2012

Advances in wind power generation, transmission, and simulation technology

Hao Chen
Iowa State University

Advances in wind power generation, transmission, and simulation technology

by

Hao Chen

A dissertation submitted to the graduate faculty

in partial fulfillment of the requirements for the degree of

DOCTOR OF PHILOSOPHY

Major: Electrical Engineering

Program of Study Committee:
Dionysios C. Aliprantis, Major Professor
Venkataramana Ajjarapu
James D. McCalley
Umesh Vaidya
Joseph Zambreno

Iowa State University

Ames, Iowa

2012

DEDICATION

This dissertation is dedicated to my wife Shurui Huang and to my newborn daughter Adalyn Chen. Without my wife's support I would not have been able to complete this work. Without my baby girl, I could not find my inner strength to survive the most difficult times.

TABLE OF CONTENTS

LIST OF TABLES vii

LIST OF FIGURES viii

ACKNOWLEDGEMENTS xi

ABSTRACT xii

CHAPTER 1. INTRODUCTION 1

CHAPTER 2. INDUCTION GENERATOR WITH VIENNA RECTIFIER: FEASIBILITY STUDY FOR WIND POWER GENERATION 8

2.1 Abstract 8

2.2 Introduction 8

2.3 Steady State Analysis 9

2.3.1 Wind Turbine and Induction Generator 9

2.3.2 Vienna Rectifier 12

2.3.3 The Proposed Configuration 13

2.4 Control Strategy 18

2.5 Simulation Results 19

2.6 Conclusions 24

CHAPTER 3. ANALYSIS OF SQUIRREL-CAGE INDUCTION GENERATOR WITH VIENNA RECTIFIER FOR WIND ENERGY CONVERSION SYSTEM 25

3.1 Abstract 25

3.2 Introduction 25

3.3 Steady-State Analysis . . . 27
3.3.1 Wind Turbine and Induction Generator . . . 28
3.3.2 Vienna Rectifier . . . 31
3.3.3 System Design . . . 32
3.4 Power Electronics Energy Loss Analysis . . . 34
3.5 Experimental Results . . . 39
3.5.1 Steady-State . . . 40
3.5.2 Transient Behavior . . . 41
3.6 Conclusions . . . 41

CHAPTER 4. ANALYSIS OF PERMANENT-MAGNET SYNCHRONOUS GENERATOR WITH VIENNA RECTIFIER FOR WIND ENERGY CONVERSION SYSTEM . . . 43

4.1 Abstract . . . 43
4.2 Introduction . . . 43
4.3 Determination of Feasible Operating Region . . . 45
4.4 System Control Strategy . . . 51
4.4.1 Component Selection . . . 52
4.4.2 Identification of Most Efficient Operating Points . . . 53
4.4.3 Simulation-Based Power Loss Estimation . . . 57
4.5 Experimental Results . . . 60
4.6 Conclusions . . . 61

CHAPTER 5. LOW-FREQUENCY AC TRANSMISSION FOR OFFSHORE WIND POWER . . . 65

5.1 Abstract . . . 65
5.2 Introduction . . . 65
5.3 System Configuration and Control . . . 67
5.3.1 Sending End Control . . . 67
5.3.2 Receiving-End Control . . . 68

5.4 System Design 71
5.4.1 Main Power Components 71
5.4.2 Filter Design 74
5.5 Case Study 77
5.6 Simulation Results 80
5.7 Conclusion 80

CHAPTER 6. DYNAMIC SIMULATION OF DFIG WIND TURBINES ON FPGA BOARDS 85

6.1 Abstract 85
6.2 Introduction 85
6.3 Modeling and Control 86
6.3.1 Induction Machine and Wind Turbine Model 86
6.3.2 DFIG Control 87
6.4 FPGA Implementation 91
6.4.1 Simulation Architecture 91
6.4.2 Synthesis and Implementation 94
6.5 Simulation Results 95
6.6 Conclusion 96

CHAPTER 7. CONCLUSION 99

7.1 Contributions 99
7.2 Future Work 100

APPENDIX A. PARAMETERS OF INDUCTION MACHINE AND WIND TURBINE 102

APPENDIX B. WIND TURBINE AND INDUCTION GENERATOR PARAMETERS FOR SIMULATION AND EXPERIMENTS 103

B.1 Wind Turbine and Induction Generator Simulation Parameters 103
B.2 Laboratory Prototype Parameters 104

APPENDIX C. WIND TURBINE AND PERMANENT-MAGNET SYNCHRONOUS GENERATOR PARAMETERS FOR SIMULATION AND EXPERIMENTS 105

C.1 Wind Turbine Parameters for Analysis and Simulation 105

C.2 Laboratory Prototype Parameters 105

References 108

LIST OF TABLES

2.1 Input Phase Voltages for $\varphi \in (-\frac{\pi}{6}, \frac{\pi}{6})$ 14

3.1 Capacitor Bank Design Parameters 33

3.2 Energy Loss Comparison 38

4.1 Energy Loss Comparison 57

4.2 PMSG Current THD Comparison 60

5.1 LFAC System Simulation Parameters 83

5.2 Parameters of PI Controllers for the 12-pulse inverter and cycloconverter 84

6.1 Xilinx Virtex–5 XC5VLX330 resources usage summary 95

6.2 Simulation parameters 96

C.1 Parameters of PI Controllers for the laboratory prototype 106

LIST OF FIGURES

1.1 Power collection and transmission for offshore wind power plants. . . . 4

2.1 Machine current leading angle (for rotor field-oriented control). 11
2.2 Power circuit of three-phase/switch/level PWM (Vienna) rectifier. . . . 13
2.3 Voltage space vectors of the Vienna rectifier input phase voltages. . . . 14
2.4 Proposed configuration. 15
2.5 Capacitance constraint curves (rotor field-oriented control). 16
2.6 Voltage and current variations corresponding to Case 1. 17
2.7 Variation of β. 17
2.8 Voltage and current variations corresponding to Case 2. 19
2.9 Control block diagram for the induction generator driven by the Vienna rectifier. 20
2.10 Loss comparison between inverter and Vienna rectifier in Case 1. . . . 21
2.11 Loss comparison between inverter and Vienna rectifier in Case 2. . . . 22
2.12 Machine currents and torque comparison ($v_w = 10$ m/s). 23

3.1 Proposed SCIG/Vienna rectifier configuration. 28
3.2 Power circuit of a Vienna rectifier. 28
3.3 Machine input impedance angle (for rotor field-oriented control). . . . 31
3.4 Capacitance constraint curves and switched capacitor bank levels. . . . 33
3.5 Variation of voltage and current at the generator terminals. 34
3.6 Variation of voltage and current at the Vienna rectifier terminals. . . . 35
3.7 Variation of power factor angle β at Vienna rectifier terminals. 36

3.8 DC-link voltage requirement. 36

3.9 Average switching frequency of Vienna rectifier with delta-hysteresis current modulation for various wind speeds. 37

3.10 Loss comparison between six-switch converter and Vienna rectifier. . . 38

3.11 Control block diagram for the induction generator driven by the Vienna rectifier. 39

3.12 Variation of power factor angle β at Vienna rectifier terminals. 40

3.13 Steady state waveforms: $i_{qs}^{e*} = 0.5$ A and $i_{mr}^{*} = -1.1$ A. 41

3.14 Transient waveforms (i_{qs}^{e*} step change from 0.65 A to 0.45 A). 42

4.1 Power circuit of a Vienna rectifier. 44

4.2 The PMSG/Vienna rectifier WECS topology. 45

4.3 Current and voltage limits on the I_{ds}^{r}–I_{qs}^{r} plane for a PMSG with six-switch two-level converter. 49

4.4 Current selection region for the PMSG with six-switch two-level converter. 49

4.5 Current and voltage limits on the I_{ds}^{r}–I_{qs}^{r} plane for a PMSG with Vienna rectifier. 50

4.6 Voltage limit curves of PMSG with Vienna rectifier. 51

4.7 Current selection region for a PMSG with Vienna rectifier. 52

4.8 Efficiency and optimal current selection of the PMSG/six-switch converter system. 54

4.9 Efficiency and optimal current selection of the PMSG/Vienna rectifier system. 55

4.10 Loss comparison between six-switch converter and Vienna rectifier. . . 56

4.11 Efficiency comparison between six-switch converter and Vienna rectifier. 57

4.12 Control block diagram for the PMSG driven by the Vienna rectifier. . 58

4.13 Simulated time-domain waveforms of PMSG stator currents and torque. 59

4.14 Optimal current operation points for the laboratory prototype. 61

4.15 Variation of active power, reactive power, and power factor angle at the generator terminals (fundamental quantities). 62

4.16 Experimental time-domain waveforms of PMSG stator voltage and current. 63

4.17 Acceleration study. 64

5.1 Configuration of the proposed LFAC transmission system. 67

5.2 Sending end DC/AC inverter control. 68

5.3 Receiving end cycloconverter control. 69

5.4 Details of the signal conditioning block. 70

5.5 Modulator for phase *a*. 70

5.6 Equivalent circuit of 20-Hz transmission system. 74

5.7 Equivalent circuit of 20-Hz transmission system for harmonic analysis. 74

5.8 Harmonic voltage amplitudes generated by the cycloconverter at the 20-Hz side. 76

5.9 Equivalent circuit of 60-Hz transmission system. 77

5.10 Sending end active power vs. max. transmission distance. 78

5.11 *LC* filter design. 79

5.12 Equivalent impedance magnitude seen from the receiving end. 79

5.13 Simulated voltage and current waveforms. 81

5.14 Transient waveforms. 82

6.1 Control block diagram for DFIG 88

6.2 FPGA implementation of DFIG wind turbine system 92

6.3 RK4 iteration process 93

6.4 Simulation results 97

C.1 Laboratory prototype. 107

ACKNOWLEDGEMENTS

I would like to take this opportunity to express my gratitude and appreciation to those who helped me with various aspects of my work. I am grateful to my advisor, Dr. Dionysios C. Aliprantis. His guidance, knowledge, patience and generosity have been significant throughout my studies. Without his support and encouragement, I could never start my professional career and reach this point.

Special thanks to my committee members, Dr. Venkataramana Ajjarapu, Dr. James D. McCalley, Dr. Umesh Vaidya, and Dr. Joseph Zambreno. All the knowledge that I have learned from you broaden my horizons and will guide me throughout my career pathway. Many thanks to Mr. Nicholas David for his kindly laboratory assistance. I would additionally like to acknowledge the financial support from the Electric Power Research Center and the Power Systems Engineering Research Center.

ABSTRACT

Wind is an increasingly important piece of electricity generation portfolios worldwide. This dissertation describes advances related to the electromechanical energy conversion system of wind turbines, and the electric transmission system for offshore wind power plants. The contributions of this work are the following: (i) We propose that the power electronics topology commonly called the "Vienna rectifier" can be used for improved variable-speed wind energy conversion. Theoretical analysis is conducted to show how a Vienna rectifier could drive either a squirrel-cage induction generator or a permanent-magnet synchronous generator-based wind turbine. Computer simulations and experimental results demonstrate the feasibility of the proposed topology and potential improvements in energy conversion efficiency. (ii) We propose a novel low-frequency ac (LFAC) transmission system for offshore wind power plants. A system design and control method is set forth, and key system operational characteristics are illustrated via computer simulations. The LFAC system constitutes a promising option for medium- or long-distance transmission, and could be an alternative to high-voltage dc (HVDC) transmission. (iii) We develop a technique that utilizes a field-programmable gate array (FPGA) as a dynamic simulation platform for wind turbines. A doubly fed induction generator-based wind turbine simulation is implemented on an FPGA board, in order to verify the effectiveness and performance advantage of this approach.

CHAPTER 1. INTRODUCTION

Electricity generation from wind is developing rapidly. By the end of 2011, the cumulative installed wind power capacity in the United States has reached 46.9 GW and wind energy accounted for 2.9% of total electricity production. The long-term goal is to obtain 20% of the U.S. electricity needs from wind by 2030 [1]. An estimate from the National Renewable Energy Laboratory (NREL) shows that wind power could be able to supply 36.6% of total electricity needs by 2050 [2]. The dramatic increase of wind power production and ambitious growth goals place increasingly stringent requirements on the performance of wind power technology. This dissertation describes advances in various aspects of wind energy conversion and transmission technology, as outlined in the following paragraphs.

Wind Energy Conversion Systems with Vienna Rectifier

The wind energy conversion system (WECS) converts the wind stream's mechanical energy to electrical energy inside the wind turbine. Here, our focus is on the electrical subsystem of the WECS, i.e., from the shaft to the power system terminals. A variety of electric generator types (e.g., squirrel-cage or wound-rotor induction machines, and synchronous machines) are used in fixed-speed or variable-speed WECS. Fixed-speed WECS are directly connected to electric power grids, whereas variable-speed WECS are connected either through a fully-rated power electronic converter (for squirrel-cage induction machines or synchronous machines) or a partially-rated power electronic converter (for doubly-fed induction generators (DFIGs)) [3]. In general, variable-speed operation is achieved by using power electronic converters with a back-to-back configuration [4,5]. Nowadays, variable-speed WECS constitute the most popular option—at least for MW-scale turbines—since they allow maximum energy extraction from the

wind, and because they can provide enhanced support to the power grid [6]. In this first part of the dissertation, we set forth a novel power electronics topology, called the "Vienna rectifier," for wind power generation.

Back-to-back six-switch two-level PWM converters are used in the majority of cases as a power electronics interface between individual wind turbines and the power grid [6]. Multi-level converters, such as the back-to-back three-level neutral-point-clamped converter, have also been proposed [7, 8]. The utilization of multi-level converters can lead to designs with higher power ratings and improved power quality. However, the large number of power switches significantly increases cost and control complexity [9]. In this work, we have identified the three-phase/three-switch/three-level PWM rectifier [10] (commonly called the "Vienna" rectifier) as a good candidate for further improving energy conversion efficiency and the reliability of generator drive systems. The Vienna rectifier has been applied mostly as a power supply module and as an active front-end stage in motor drives [11]. This topology can generate three voltage levels with reduced number of controlled power switches (only three), thus simplifying the control and reducing cost (although more power diodes are needed). An another advantage is that it leads to reduced blocking voltage stress on the power semiconductors, which can enhance reliability.

Low-Frequency AC (LFAC) Transmission System for Offshore Wind Power

Onshore geographic sites that are optimal for constructing wind power plants are often in remote locations, typically far from the major load centers. In the United States, for example, the largest potential for onshore wind energy exists in the Midwest, hundreds of miles away from the large load centers of the East and West coasts. In addition, "good" offshore sites with abundant wind potential and/or other attractive environmental characteristics could be located tens of miles away from the coasts. Hence, the transmission of large amounts of wind power over long distances has become a timely and significant technical challenge [**?**, 12–15] In this second part of the dissertation, a novel transmission technology specifically for offshore wind power plants is proposed.

Offshore wind power is expected to represent a significant component of the future electric generation portfolio due to large space availability and better wind energy potential in offshore locations [2, 16]. As estimated from NREL, 4,150 GW of potential wind turbine nameplate capacity from offshore wind resources are available in the United States [17]. In the next 10–20 years, a dramatic increase of offshore wind power plants is expected to occur, conditional on the reduction of installation costs and the advent of necessary technological breakthroughs. Plans to establish offshore wind power plants with power ratings up to 1,500 MW, at distances up to ca. 150 km from the coast have been recently proposed in Germany [18]. In the United States, ca. 20 projects representing more that 2 GW of capacity are in the planing and permitting process [19].

For an offshore wind power plant, as shown in Fig. 1.1, a medium-voltage ac or dc grid can be used to collect the wind turbines' power and deliver it to an offshore platform within the plant [6,20]. [1] A transmission system is necessary to integrate the plant with the onshore main power grid. Presently, high-voltage ac (HVAC) and high-voltage dc (HVDC) are well established transmission technologies [13]. HVAC is a conventional and convenient strategy because it is relatively straightforward to design the protection system, and it is easy to change voltage levels using transformers. HVAC is a suitable solution for delivering onshore wind power over long distances using overhead transmission lines. However, when underground ac transmission cables (for onshore plants) or submarine cables (for offshore plants) need to be used, HVAC is no longer a technically feasible option. In such applications, the cable's high capacitance leads to considerable charging current, which in turn reduces the active power transmission capacity of the cable, and limits the transmission distance. Currently, HVAC is widely adopted for short offshore transmission distances (e.g., 50–75 km) [12]. To overcome this disadvantage of HVAC, the HVDC technology has been developed. Depending on the power electronic devices used in the converters at the two ends of an HVDC system, it can be classified into two types: (i) line-commutated converter HVDC (LCC-HVDC) using thyristors, and (ii) voltage source converter HVDC (VSC-HVDC) using self-commutated devices (e.g., IGBTs) [21]. Currently,

[1] It is interesting to note that the proposed Vienna rectifier-based WECS discussed previously could be utilized to establish a dc collection grid. This could be a subject of future research.

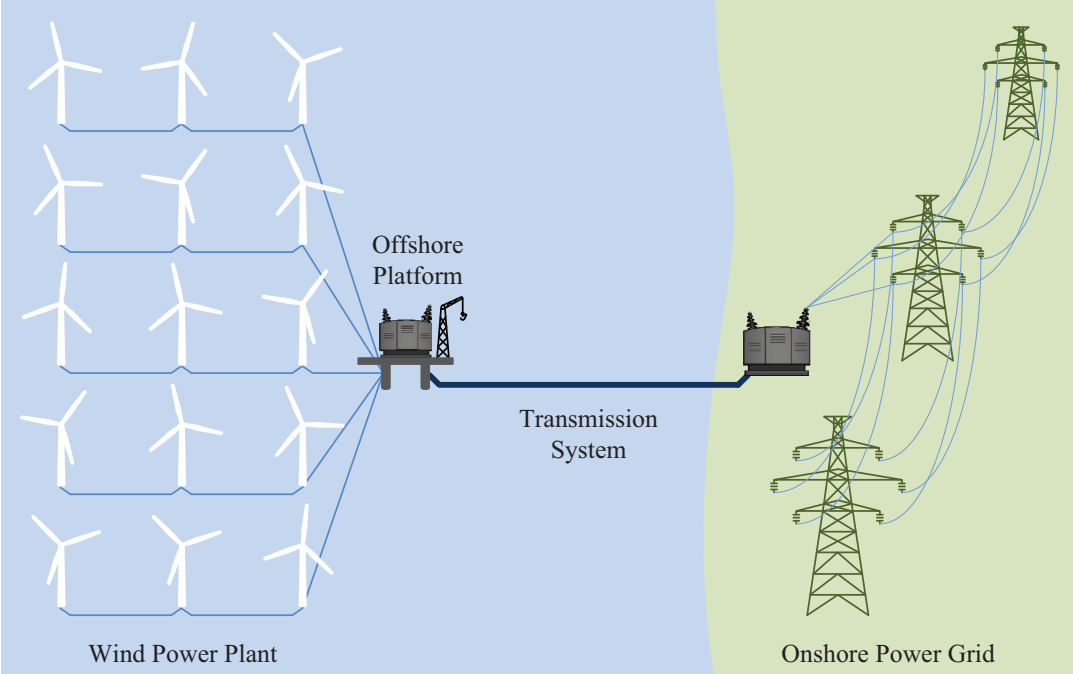

Figure 1.1 Power collection and transmission for offshore wind power plants.

HVDC is widely applied for delivering large amounts of power (typically around 1 GW for LCC-HVDC and 400 MW for VSC-HVDC) over long distances (e.g., greater than 100 km, especially for offshore wind power), since it imposes essentially no limit on transmission distance due to the absence of charging current in dc power cables [14].

Besides HVAC and HVDC, a low-frequency ac (LFAC) transmission system has also been recently proposed [22–25]. Here, low frequency refers to a frequency lower than the nominal power frequency (60 or 50 Hz). Since a thyristor-based cycloconverter is used as the frequency converter interface between the low-frequency side and the power frequency side, the transmission frequency is preferably set to be one third of the nominal power frequency (i.e., 20 or 16.66 Hz) in order to reduce the harmonics [22, 26]. In this work, we have proposed a new LFAC transmission system to connect dc collection-based offshore wind power plants with the main power grid. Within the plant (the sending end), a dc/ac 12-pulse thyristor-based inverter is used to generator low-frequency ac power. At the onshore substation (the receiving end), a three-phase bridge (6-pulse) cycloconverter is used as an interface.

In general, the LFAC system has higher reliability and lower cost compared to VSC-HVDC, and can transmit power over longer distances compared to an HVAC system. The LFAC transmission could be optimal for medium distance transmission (somewhere in between HVAC and HVDC) [25].

FPGA-based Simulation Platform

Modeling and simulation is indispensable for designing and studying complex systems such as wind turbines and power transmission schemes, especially when experiments with actual components are usually prohibitively expensive or impossible to conduct [27–33]. In the past, when fixed-speed wind turbines were mainly used, modeling and simulation studies was relatively easy to conduct, and conventional offline simulation platforms (such as PSS/E) were accurate enough to show phenomena of interest [34–36]. However, after the introduction of power electronic converters in wind applications, more sophisticated simulation platforms are required, especially when detailed switching-level simulations are needed. Although conventional offline simulation platforms (such as Matlab/Simulink and PSCAD) can still be used, the simulation speed is very low due to high computational burden. Recently, real-time simulators (such as RTDS and RT-LAB) have been developed to improve simulation efficiency and facilitate system analysis [37–40]. However, the simulation of large-scale systems requires bulky hardware, which raises the cost and limits the application of these simulators. This last part of the dissertation sets forth the basics of a novel technique for simulating wind turbines, making use of FPGAs.

A field-programmable gate array (FPGA) is a reconfigurable digital logic platform. Due to its inherently parallel hardware architecture, FPGA allows the parallel execution of millions of bit-level operations in a spatially programmed environment. Research has been under way on the modeling and real-time simulation of various electrical power components using FPGAs as computational [41–45] and non-computational [46, 47] devices.

The dynamic (time-domain) simulation of electrical power systems involves the numerical solution of a set of ordinary differential equations (ODEs). On the other hand, the various

numerical integration algorithms (i.e., ODE solvers) usually only require additions and multiplications, which are generally simple mathematical operations to implement on a digital platform. Moreover, complex systems requiring the simultaneous solution of numerous ODEs for simulation are inherently conducive to a parallel mapping to physical computational resources. By mapping an ODE solver on an FPGA board (a process that is called hardware implementation), we can increase efficiency by reducing the overhead introduced by software, which leads to substantial simulation speed gains compared to using personal computers. Therefore, FPGA-based simulation represents an attractive option for simulating more complex electrical power and power electronics-based systems.

Dissertation Organization

The remainder of this dissertation is organized as follows, where each chapter represents either a journal or conference publication.

Chapter 2 investigates the feasibility of using a topology with a squirrel-cage induction generator and a Vienna rectifier for a wind energy conversion system. Details about the operation of Vienna rectifiers are provided in this chapter. A comparison between the proposed system and a conventional system that uses the classical six-switch two-level converter is performed to illustrate the expected efficiency improvement.

Chapter 3 proposes a new WECS topology that uses a Vienna rectifier as the generator-side converter for a squirrel-cage induction generator (SCIG). The operation of a SCIG/Vienna rectifier configuration is analyzed in detail. A power converter loss evaluation is performed to show the efficiency improvement. Experimental results obtained from a laboratory prototype are used to validate the theoretical analysis and feasibility of the proposed system.

Chapter 4 analyzes a WECS topology that uses a Vienna rectifier as the generator-side converter for a permanent-magnet synchronous generator (PMSG). A theoretical analysis of the PMSG/Vienna rectifier configuration is provided. Also, we devise a control strategy that leads to maximum efficiency, based on detailed power loss calculations for the power electronic converter and the generator. Experimental results are provided to demonstrate the feasibility

of the proposed system.

Chapter 5 proposes a new LFAC transmission system to connect dc collection-based offshore wind power plants with the main power grid. The system design and control are addressed. A comparison between the proposed LFAC system and the conventional HVAC system is performed.

Chapter 6 presents the implementation of a dynamic simulation of a doubly-fed induction generator (DFIG)-based wind turbine on an FPGA development board. The basic steps of designing an explicit fourth-order Runge–Kutta numerical ordinary differential equation solver on the FPGA platform are outlined. The FPGA simulation results and speed improvement are validated versus a Matlab/Simulink simulation.

Chapter 7 summarizes the contributions of this work and recommends further investigations for future work.

CHAPTER 2. INDUCTION GENERATOR WITH VIENNA RECTIFIER: FEASIBILITY STUDY FOR WIND POWER GENERATION

A paper published in the *Proceedings of the IEEE International Conference on Electrical Machines*, 2010

Hao Chen[1] and Dionysios C. Aliprantis

2.1 Abstract

This paper investigates the feasibility of using a topology with a squirrel-cage induction machine and a Vienna rectifier for a wind energy conversion system. Simulation results reveal that this configuration is advantageous with respect to energy efficiency and reliability compared to a traditional six-switch two-level inverter.

2.2 Introduction

Variable-speed wind energy conversion systems (WECS) are commonly used because they allow maximum power extraction from the wind [48]. Configurations using various machine types (e.g., squirrel-cage or wound-rotor induction machines, and permanent magnet synchronous machines) have been studied extensively [4, 5, 49, 50]. Back-to-back six-switch two-level PWM converters are often used. Multi-level converters, such as the back-to-back three-level neutral-point-clamped converter, have been used as well [8]. The utilization of multi-level converters can lead to designs with higher power ratings and improved power quality. However, the large number of power switches significantly increases cost and control complexity [9].

[1]Primary researcher and author

The three-phase/switch/level PWM (Vienna) rectifier [10], has been applied mostly as a power supply module and as an active front-end stage in motor drives [11]. The Vienna rectifier can generate three voltage levels with decreased number of power switches (only three) thus simplifying the control, and leads to reduced blocking voltage stress on the power semiconductors.

In this paper, the feasibility of using the Vienna rectifier in a variable-speed WECS as the generator drive is investigated. A topology with a squirrel-cage induction generator and a Vienna rectifier is proposed. This could be utilized, for example, to establish dc grids in offshore wind power plants with HVDC transmission [20, 51, 52]. Two case studies are devised to illustrate the operational characteristics of the proposed system. This configuration is compared to the conventional six-switch two-level converter system by way of simulations. It is shown that the Vienna-rectifier topology has better efficiency, and the potential for better reliability.

2.3 Steady State Analysis

2.3.1 Wind Turbine and Induction Generator

It is well known that the mechanical power P_m extracted from the wind can be expressed as [48]:

$$P_m = \tfrac{1}{2}\rho\pi R_w^2 c_p\left(\lambda,\gamma\right) v_w^3\,, \tag{2.1}$$

where v_w is the upstream wind speed; ρ is the air density; R_w is the wind turbine radius; $c_p\left(\lambda,\gamma\right)$ is the performance coefficient; γ is the pitch angle in degrees; and λ is the tip-speed ratio given by $\lambda = \omega_w R_w / v_w$, where ω_w is the blades' angular velocity. In this study, pitching of the blades is not considered, so $\gamma = 0$, and $c_p(\lambda, 0)$ attains its maximum value $c_p^{\max} = 0.48$ for an optimal $\lambda_o = 8.10$. In a variable-speed wind turbine, the blades' speed is changed proportionally to the wind speed such that λ_o is always maintained, in order to extract maximum power from the wind [5]. The relation between λ_o and the optimal wind turbine rotor speed

ω_{wo} (or the optimal generator electrical speed ω_{ro}) is given by

$$\lambda_o = \frac{\omega_{wo} R_w}{v_w} = \frac{\omega_{ro}}{v_w} K_1 \,, \tag{2.2}$$

where $K_1 = \frac{2R_w}{GP}$, G is the gearbox ratio, and P is the number of generator poles. Using (3.2) to express v_w in terms of ω_{ro} and λ_o, (4.1) becomes

$$P_m^{\max} = K_2 c_p^{\max} \left(\frac{\omega_{ro}}{\lambda_o} K_1 \right)^3 \,, \tag{2.3}$$

where $K_2 = \frac{1}{2}\rho\pi R_w^2$. Therefore, the mechanical torque applied to the generator shaft has a quadratic speed function:

$$T_m^{\max} = \frac{P}{2} \frac{P_m^{\max}}{\omega_{ro}} = \frac{P K_2 K_1^3 c_p^{\max}}{2\lambda_o^3} \omega_{ro}^2 \,. \tag{2.4}$$

Using generator convention for the stator currents, the input impedance of the induction machine is given by

$$Z_m = \frac{\tilde{V}_m}{-\tilde{I}_m} = R + jX \,, \tag{2.5}$$

where $\tilde{V}_m$ and $\tilde{I}_m$ are the machine's terminal voltage and current. The classical induction machine model [53] yields

$$R = R_s + \frac{(\omega_e L_m)^2 \frac{R_r'}{s}}{\left(\frac{R_r'}{s}\right)^2 + (\omega_e L_r')^2} \tag{2.6}$$

$$X = \omega_e L_s - \frac{\omega_e L_r' (\omega_e L_m)^2}{\left(\frac{R_r'}{s}\right)^2 + (\omega_e L_r')^2} \,. \tag{2.7}$$

Note that $R < 0$ for generator action, and $X > 0$; hence, the power factor angle $\alpha = \tan^{-1}(X/R)$ is between 90° and 180°. Since $-\tilde{I}_m$ lags $\tilde{V}_m$ by α, it follows that $\tilde{I}_m$ leads $\tilde{V}_m$ by $180° - \alpha$.

If the rotor field-oriented control [53] is adopted (also refer to Section 2.4 for notation), the slip frequency ω_s is set to

$$\omega_s = \frac{R_r' I_{qs}^e}{L_r' I_{ds}^e} \,, \tag{2.8}$$

and the d-axis stator current I_{ds}^e is set to

$$I_{ds}^e = -\frac{\Lambda_r'}{L_m} \,, \tag{2.9}$$

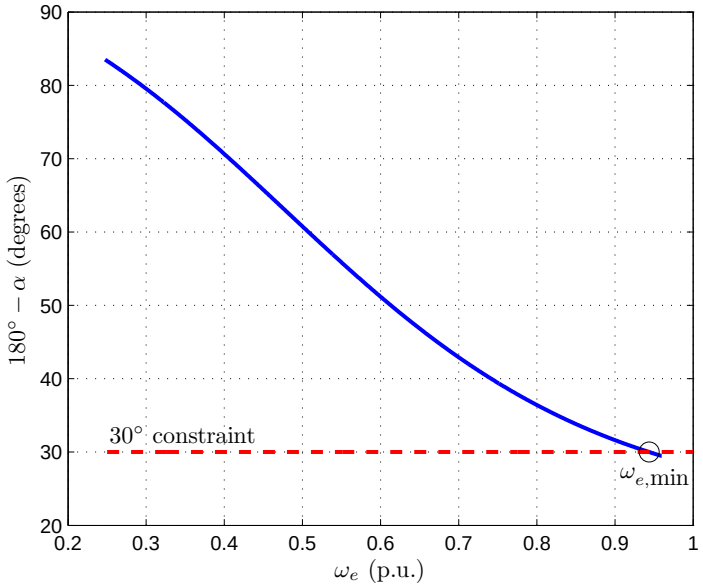

Figure 2.1 Machine current leading angle (for rotor field-oriented control).

where Λ'_r is the machine's rated rotor flux. The electromagnetic torque of the machine is

$$T_e = \frac{3}{2}\frac{P}{2}\frac{L_m}{L'_r}\Lambda'_r I^e_{qs}\,. \tag{2.10}$$

Since T_e is equal to $T_m^{\max}$ given by (3.4) at the steady state, the q-axis stator current I^e_{qs} can be expressed as

$$I^e_{qs} = \frac{2K_2K_1^3 c_p^{\max} L'_r}{3\lambda_o^3 L_m \Lambda'_r}\omega_{ro}^2\,. \tag{2.11}$$

Substitution of (3.5) and (3.8) into (2.8) yields

$$\omega_s = -\frac{2K_2K_1^3 c_p^{\max} R'_r}{3\lambda_o^3 \Lambda'^2_r}\omega_{ro}^2\,. \tag{2.12}$$

This analysis shows that the electrical frequency, $\omega_e = \omega_{ro} + \omega_s$, can be related to the wind speed via (3.2).

Using (2.6), (2.7), and (2.12), one can compute the angle for which $\tilde{I}_m$ leads $\tilde{V}_m$ for different ω_e (or wind speeds); this is shown in Fig. 2.1. The significance of this calculation will be explained in a later section. Note that the parameters of the machine and wind turbine are provided in Appendix A.

2.3.2 Vienna Rectifier

The topology of a three-phase/switch/level PWM (Vienna) rectifier is shown in Fig. 4.1. Taking the center point N of the DC-link voltage as the reference point, the rectifier input phase voltage v_{kN}, which depends on both the switching state of the corresponding power switch S_k and the sign of the corresponding phase current i_k, is given by [54]

$$v_{kN} = \begin{cases} \text{sgn}\{i_k\}\frac{V_o}{2} & \text{if } S_k = 0 \\ 0 & \text{if } S_k = 1 \end{cases} \tag{2.13}$$

where the index k can be $A, B,$ or C. Note that the blocking voltage stress of the switches and diodes in Fig. 4.1 is only half of the total DC-link voltage V_o.

For a balanced set of input phase currents (with $i_A = \sqrt{2}I\cos\varphi$), a sign reversal of the three phase currents (i_A, i_B, i_C) takes place every $\frac{\pi}{3}$ electrical radians. Thus, according to (2.13), the input phase voltage v_{kN} is shown in Table 2.1 for eight switching state combinations, and for $\varphi \in (-\frac{\pi}{6}, \frac{\pi}{6})$. The variable $\bar{v}$ in Table 2.1 represents the complex space vector of the input phase voltages, which is given by [55]:

$$\bar{v} = \frac{2}{3}\left(v_{AN} + a v_{BN} + a^2 v_{CN}\right) \tag{2.14}$$

where $a = e^{j\frac{2\pi}{3}}$. The voltage space vectors in Table 2.1 form a hexagon (i.e., A-B-C-D-E-F) in the complex plane, as shown in Fig. 2.3. For the next interval $\varphi \in (\frac{\pi}{6}, \frac{\pi}{2})$, a similar derivation results in the hexagon A-G-H-I-C-J, which can be considered as resulting from a counter-clockwise rotation of the hexagon A-B-C-D-E-F by $\frac{\pi}{3}$.

When the rectifier input current space vector $\bar{i}$, which is

$$\bar{i} = \frac{2}{3}\left(i_A + a i_B + a^2 i_C\right) = \sqrt{2}I\left(\cos\varphi + j\sin\varphi\right), \tag{2.15}$$

is located in any one of the six intervals, then the possible rectifier input voltage space vector must be located in the corresponding hexagon. For example, if $\bar{i}$ is located in the interval $\varphi \in (-\frac{\pi}{6}, \frac{\pi}{6})$, the possible input voltage space vector must be located in the hexagon A-B-C-D-E-F. However, if $\bar{i}$ is on a hexagon boundary (e.g., $\varphi = -\frac{\pi}{6}$), the possible input voltage space vector must be located in the overlap of two adjacent hexagons (e.g., the parallelogram

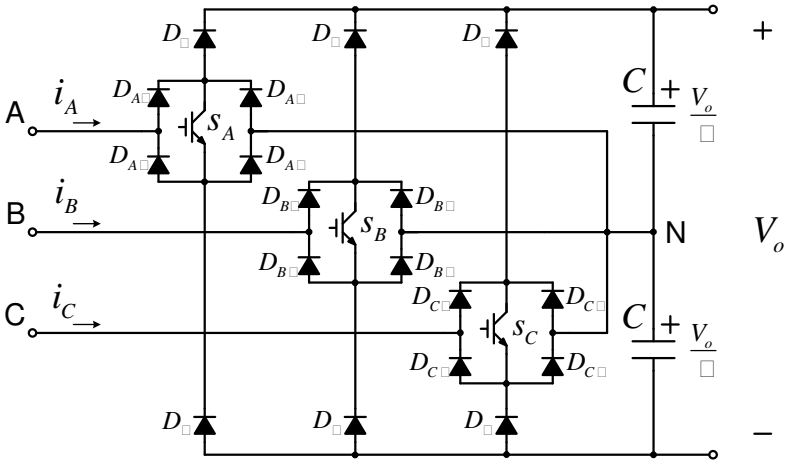

Figure 2.2 Power circuit of three-phase/switch/level PWM (Vienna) rectifier.

A-J-E-F in Fig. 2.3). Therefore, the Vienna rectifier allows the input current ($\tilde{I}$ in Fig. 3.1) to lead or lag the input voltage ($\tilde{V}$ in Fig. 3.1) by no more than 30°.

2.3.3 The Proposed Configuration

In principle, a Vienna rectifier could be connected directly with an induction generator. However, the 30° angle constraint, shown in Fig. 2.1, would make the minimum possible frequency, $\omega_{e,\min}$, a fairly large value, thus greatly narrowing the operation range. In other words, the Vienna rectifier cannot supply enough reactive power to the machine for $\omega_e < \omega_{e,\min}$. One possible way to provide reactive power is by connecting a capacitor bank across the machine terminals, as shown in Fig. 3.1. The connection of the capacitor bank can make the voltage ($\tilde{V}$) and current ($\tilde{I}$) at the AC side of the Vienna rectifier satisfy the angle constraint. The equivalent input impedance of the proposed system is

$$Z = \frac{\tilde{V}}{-\tilde{I}} = (R + jX) \,//\, \left(\frac{1}{j\omega_e C}\right) + j\omega_e L = \frac{R + jX_{eq}}{(1 - \omega_e C X)^2 + (\omega_e C R)^2} \tag{2.16}$$

where

$$X_{eq} = \left(\omega_e^2 LC - 1\right)\left[\omega_e C\left(R^2 + X^2\right) - 2X\right] + \omega_e L - X\,. \tag{2.17}$$

Note that $R < 0$ for generator action, but X_{eq} can acquire both positive and negative values. In order to satisfy the Vienna rectifier constraint, $\tilde{I}$ must not lead or lag $\tilde{V}$ by more

Table 2.1 Input Phase Voltages for $\varphi \in (-\frac{\pi}{6}, \frac{\pi}{6})$

S_A	S_B	S_C	v_{AN}	v_{BN}	v_{CN}	$\bar{v}$
0	0	0	$\frac{V_o}{2}$	$-\frac{V_o}{2}$	$-\frac{V_o}{2}$	$\frac{2V_o}{3}$
0	0	1	$\frac{V_o}{2}$	$-\frac{V_o}{2}$	0	$\frac{V_o}{2}(1-j\frac{1}{\sqrt{3}})$
0	1	0	$\frac{V_o}{2}$	0	$-\frac{V_o}{2}$	$\frac{V_o}{2}(1+j\frac{1}{\sqrt{3}})$
0	1	1	$\frac{V_o}{2}$	0	0	$\frac{V_o}{3}$
1	0	0	0	$-\frac{V_o}{2}$	$-\frac{V_o}{2}$	$\frac{V_o}{3}$
1	0	1	0	$-\frac{V_o}{2}$	0	$\frac{V_o}{2}(\frac{1}{3}-j\frac{1}{\sqrt{3}})$
1	1	0	0	0	$-\frac{V_o}{2}$	$\frac{V_o}{2}(\frac{1}{3}+j\frac{1}{\sqrt{3}})$
1	1	1	0	0	0	0

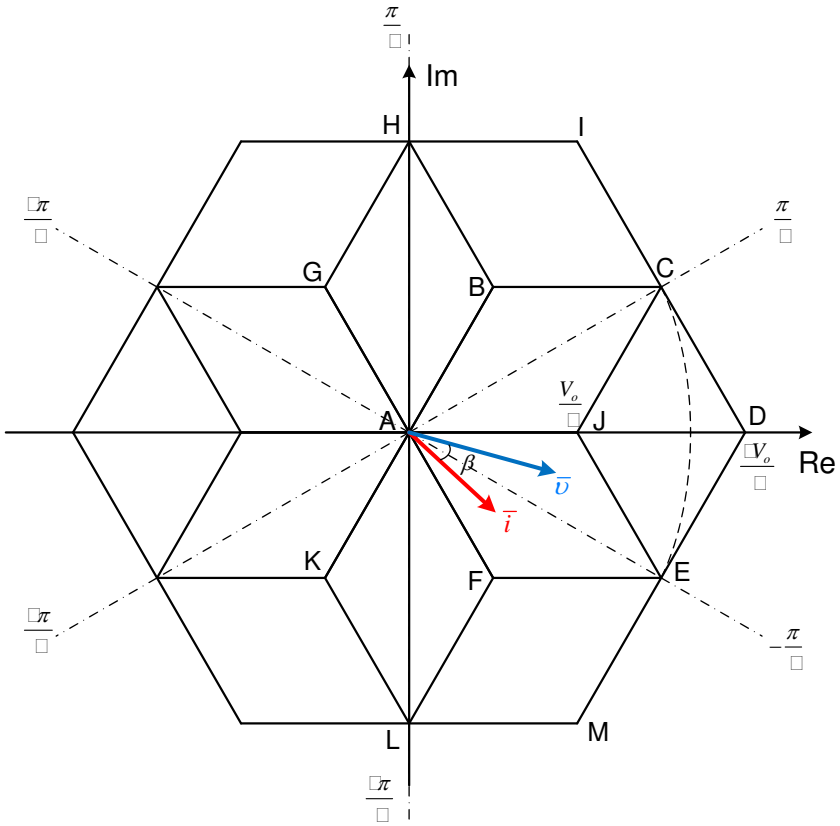

Figure 2.3 Voltage space vectors of the Vienna rectifier input phase voltages.

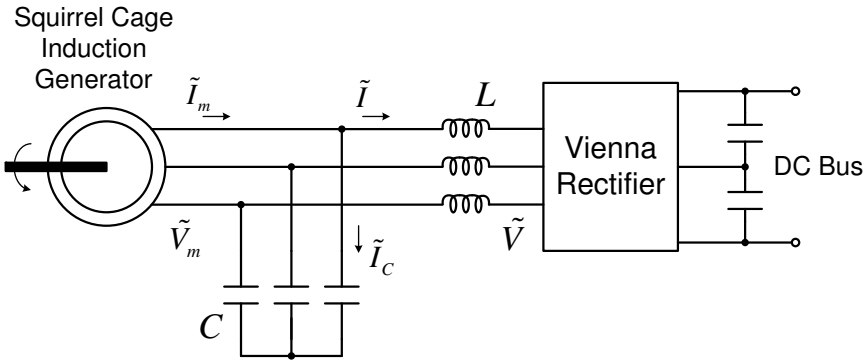

Figure 2.4 Proposed configuration.

than 30°. This leads to the following inequality constraint:

$$|X_{eq}| \leq |R| \tan 30^\circ = \frac{|R|}{\sqrt{3}}. \tag{2.18}$$

The equivalent resistance and reactance of the machine (R and X) depend on the slip s and the synchronous speed ω_e. Hence, four variables (s, ω_e, C, and L) should be appropriately chosen to satisfy (2.18) in order to make the proposed system operate normally.

The resonant frequency of the LC filter is

$$\omega_f = \frac{1}{\sqrt{LC}}. \tag{2.19}$$

Using (2.19) to express L in terms of C and ω_f, (2.17) becomes

$$X_{eq} = \left(\frac{\omega_e^2}{\omega_f^2} - 1\right)\left[\omega_e C\left(R^2 + X^2\right) - 2X\right] + \frac{\omega_e}{\omega_f^2 C} - X. \tag{2.20}$$

With a choice of $\omega_f = 2.5\omega_b$, the constraint C vs. ω_e can be calculated. The two blue curves in Fig. 2.5 correspond to

$$X_{eq} = \pm\frac{|R|}{\sqrt{3}}. \tag{2.21}$$

So, the choice of a certain capacitance confines the operational range of ω_e.

2.3.3.1 Case 1

The capacitance C_1 can be selected to obtain the maximum operational range of ω_e (i.e., ω_{e1} to $\omega_{e,\max}$) as shown in Fig. 2.5. C_1 can be calculated using (2.6), (2.7), (2.20), and (2.21).

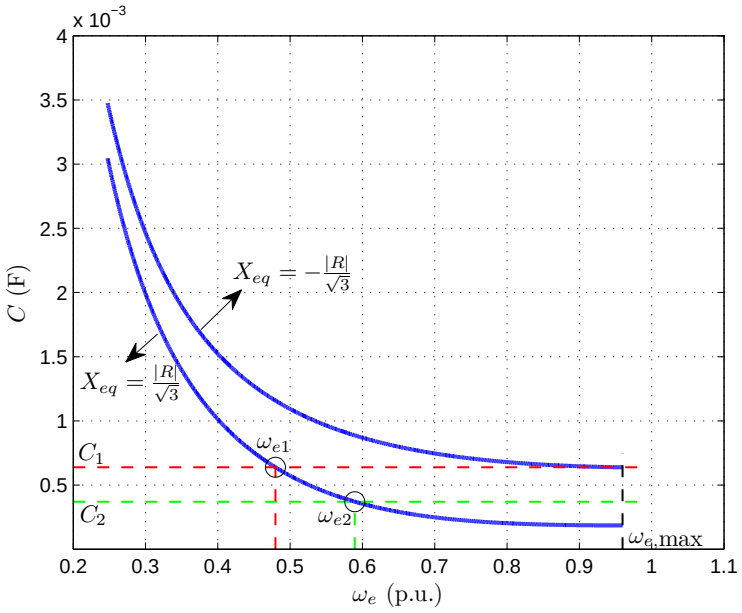

Figure 2.5 Capacitance constraint curves (rotor field-oriented control).

The inductance L_1 corresponding to C_1 is obtained by (2.19). The same set of equations can be used to compute ω_{e1}.

After C_1 and L_1 are determined, a steady-state analysis can provide the variation of $|\tilde{V}_m|$, $|\tilde{V}|$, $|\tilde{I}_m|$, and $|\tilde{I}|$, as shown in Fig. 2.6. Let β denote the angle by which $\tilde{I}$ lags $\tilde{V}$. According to the Vienna rectifier analysis, β varies from $-30°$ to $30°$ when ω_e varies from ω_{e1} to $\omega_{e,\max}$, as shown by the blue curve in Fig. 2.7. From Fig. 2.3 and geometric considerations, the maximum possible magnitude of $\bar{v}$ for steady-state operation can be determined as

$$|\bar{v}|_{\max} = \frac{V_o}{2\sqrt{3}\cos(60° - |\beta|)}\,. \tag{2.22}$$

This equation can be used to establish the level of required DC-link voltage. From Figs. 2.6 and 2.7, it can be seen that maximum voltage $|\tilde{V}|_{\max}$ occurs when $\beta = 30°$. This angle also coincides with the minimum voltage that the Vienna rectifier can generate, which is $V_o/3$ according to (2.22). Therefore, the DC-link voltage of the rectifier V_o must satisfy

$$\frac{V_o}{3} \geq |\tilde{V}|_{\max}\,. \tag{2.23}$$

The above inequality implies that V_o has to be set as a fairly large value (close to 3 p.u.) in order to make the generator operate normally at $\omega_{e,\max}$.

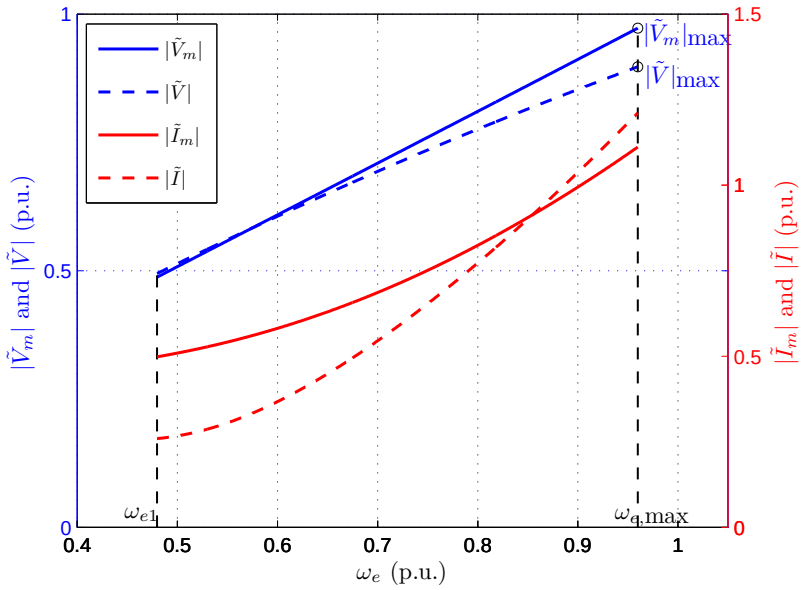

Figure 2.6 Voltage and current variations corresponding to Case 1.

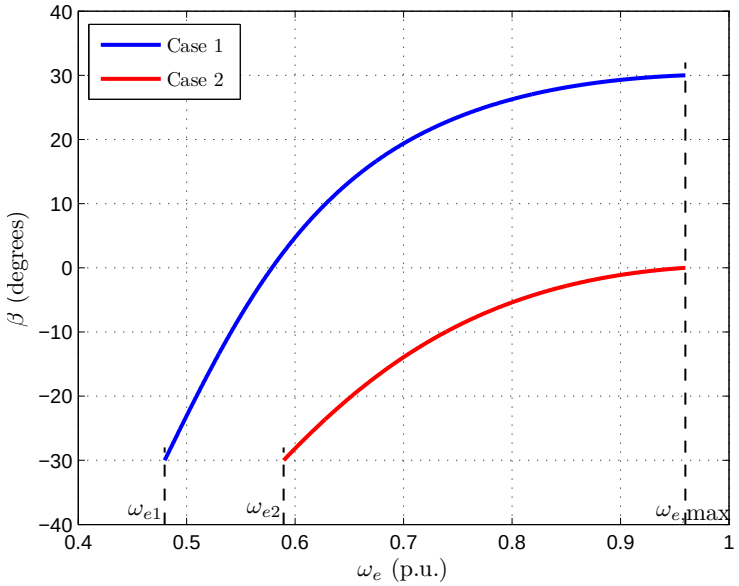

Figure 2.7 Variation of β.

2.3.3.2 Case 2

On the other hand, (2.22) shows that $|\bar{v}|_{\max}$ obtains its largest value, $V_o/\sqrt{3}$, for $\beta = 0°$. Therefore, one can select the capacitance C_2 such that $\beta = 0°$ at $\omega_{e,\max}$, as shown in Fig. 2.5 and by the red curve in Fig. 2.7. The value of C_2 can be calculated using (2.6), (2.7), (2.20), and $X_{eq} = 0$. In this case, V_o must satisfy

$$\frac{V_o}{\sqrt{3}} \geq |\tilde{V}|_{\max} . \tag{2.24}$$

The value of $|\tilde{V}|_{\max}$ can be obtained by using the new values of C_2 and the corresponding L_2, as depicted in Fig. 2.8. The minimum frequency ω_{e2} can be determined similarly to ω_{e1}. Since $\beta = -30°$ at ω_{e2}, the second constraint for V_o is

$$\frac{V_o}{3} \geq |\tilde{V}|_{\min} , \tag{2.25}$$

where $|\tilde{V}|_{\min}$ corresponds to ω_{e2} in Fig. 2.8. Combining (2.24) and (2.25) yields that V_o must satisfy

$$V_o \geq \max\left(\sqrt{3}|\tilde{V}|_{\max},\ 3|\tilde{V}|_{\min}\right) . \tag{2.26}$$

The required DC-link voltage for Case 2 is lower than that of Case 1. However, the operational speed range for Case 1 is larger than that of Case 2.

2.4 Control Strategy

The rotor field-oriented control is applied for the proposed system. The control structure is shown in Fig. 3.11. The reference frame transformation matrices $\mathbf{K}_s^s$, ${}^s\mathbf{K}^e$, and ${}^e\mathbf{K}^s$ are defined in [53]. The d-axis of the synchronous reference frame is aligned with the rotor flux vector. The speed is controlled in order to extract maximum power from the wind. The rotor flux is set to a rated value. The description of the flux observer is provided in [55].

Various modulation methods exist to form the sinusoidal currents $\boldsymbol{i}_{ABC}$ feeding into the Vienna rectifier, such as continuous or discontinuous space vector modulation [56–58]. Herein, the hysteresis modulation is applied for simplicity. As shown in Fig. 3.11,

$$S'_k = \begin{cases} 0 & \text{if } i_k > i_k^* + h \\ 1 & \text{if } i_k < i_k^* - h \end{cases} \tag{2.27}$$

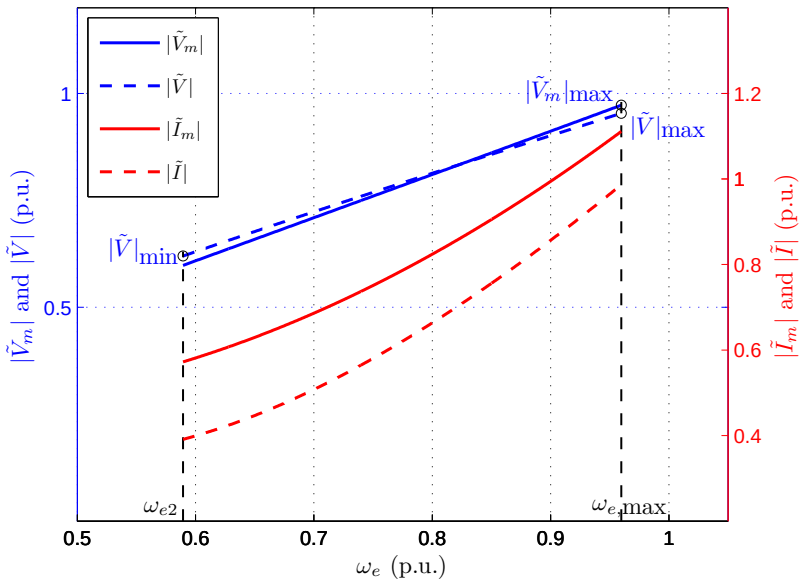

Figure 2.8 Voltage and current variations corresponding to Case 2.

where $\pm h$ defines the hysteresis band. Due to (2.13), the control signals S_k of the switches are given by [54]:

$$S_k = \begin{cases} S'_k & \text{if } i_k^* \geq 0 \\ \overline{S'_k} & \text{if } i_k^* < 0 \end{cases} \tag{2.28}$$

Herein, the balancing of the center point (N) voltage is not considered for simplicity. Note that this issue can be easily solved by adding a zero-sequence component to $\boldsymbol{i}^*_{ABC}$ [54]. The DC-link voltage V_o can be controlled by a grid-side converter, which is not shown in Fig. 3.11.

2.5 Simulation Results

To demonstrate the validity and characteristics of the proposed WECS, simulations have been performed using Matlab/Simulink and PLECS [59]. A conventional system of an induction generator driven by a six-switch two-level inverter with hysteresis modulation was also implemented, in order to show the performance advantage of the proposed system. Both systems use the same hysteresis band (i.e., $h = 0.05$ pu).

In the conventional system, the inverter's DC-link voltage must satisfy $V_{o(\text{inv})}/\sqrt{3} \geq |\tilde{V}_m|_{\max}$, where $|\tilde{V}_m|_{\max}$ corresponds to $\omega_{e,\max}$ in Figs. 2.6 and 2.8. For the machine parameters used

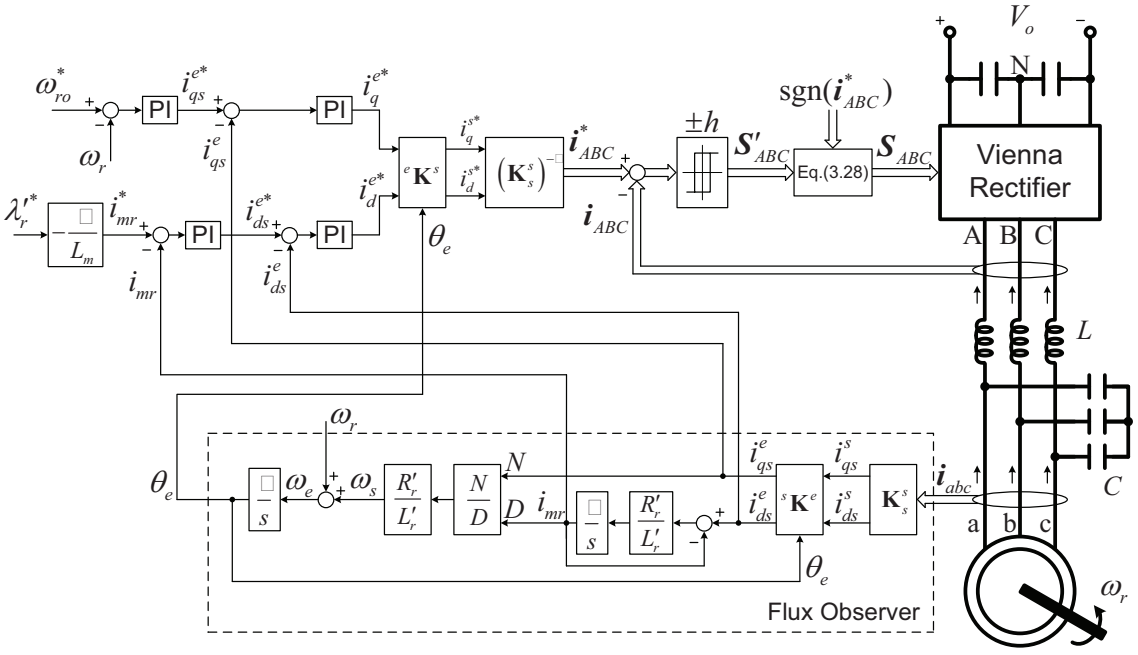

Figure 2.9 Control block diagram for the induction generator driven by the Vienna rectifier.

here, $V_{o(\text{inv})}$ can be set as 700 V. This will be the blocking voltage stress of the inverter switches.

On the other hand, the DC-link voltage of the Vienna rectifier for Case 1 is constrained by (2.23), where $|\tilde{V}|_{\max}$ is obtained by Fig. 2.6. Herein, $V_o = 1,400$ V for Case 1, even though a slightly lower voltage could have been chosen (as low as $1,127$ V). This will impose the same blocking voltage stress as the inverter's switches on the switches of the Vienna rectifier. For Case 2, however, V_o can be set as low as 700 V according to (2.26) and Fig. 2.8. Therefore, the blocking voltage stress of the switches for Case 2 is decreased to 350 V.

Based on the voltage and current requirements, the POWEREX CM400HA-24A (400 A/ 1200 V) single IGBT module [60] can be used to construct the inverter, and both CM400HA-24A and the POWEREX QRS1240T30 (180 A/1200 V) fast recovery diode module [61] can be used to set up the Vienna rectifier. Note that the free-wheeling diode in the IGBT module does not conduct current in the Vienna rectifier. Since PLECS supports the thermal modeling and simulation of semiconductors, the switching and conduction loss can be obtained as long as the thermal description parameters of switches and diodes are specified in the PLECS circuits [59].

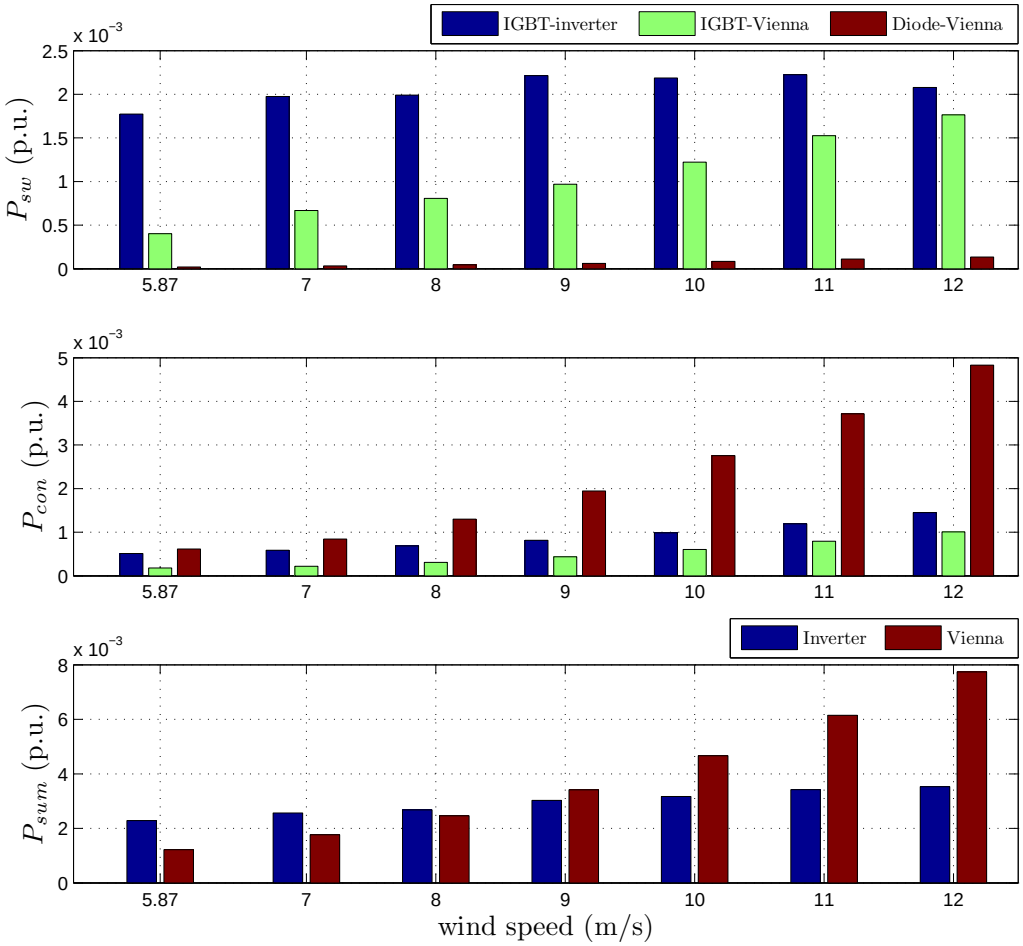

Figure 2.10 Loss comparison between inverter and Vienna rectifier in Case 1.

The thermal description parameters of POWEREX CM400HA-24A and QRS1240T30, such as on-state voltage, turn-on and turn-off losses, can be acquired from the component data sheets [61, 62] and the Power Module Loss Simulator [63].

The switching loss P_{sw}, conduction loss P_{con}, and total loss $P_{sum} = P_{sw} + P_{con}$ of the IGBT modules in one phase leg of the inverter are presented in Figs. 2.10 and 2.11. These are compared to P_{sw}, P_{con}, and P_{sum} of the IGBT module and the diode modules in one phase leg of the Vienna rectifier. (The wind speeds of 5.87 m/s and 7.25 m/s correspond to ω_{e1} and ω_{e2}.) Figures 2.10 and 2.11 show that P_{sw} and P_{con} of IGBTs and diodes in the Vienna rectifier rise with the increase of wind speed. The IGBTs dominate the switching loss, whereas the diodes dominate the conduction loss. Since the blocking voltage stress of IGBTs and

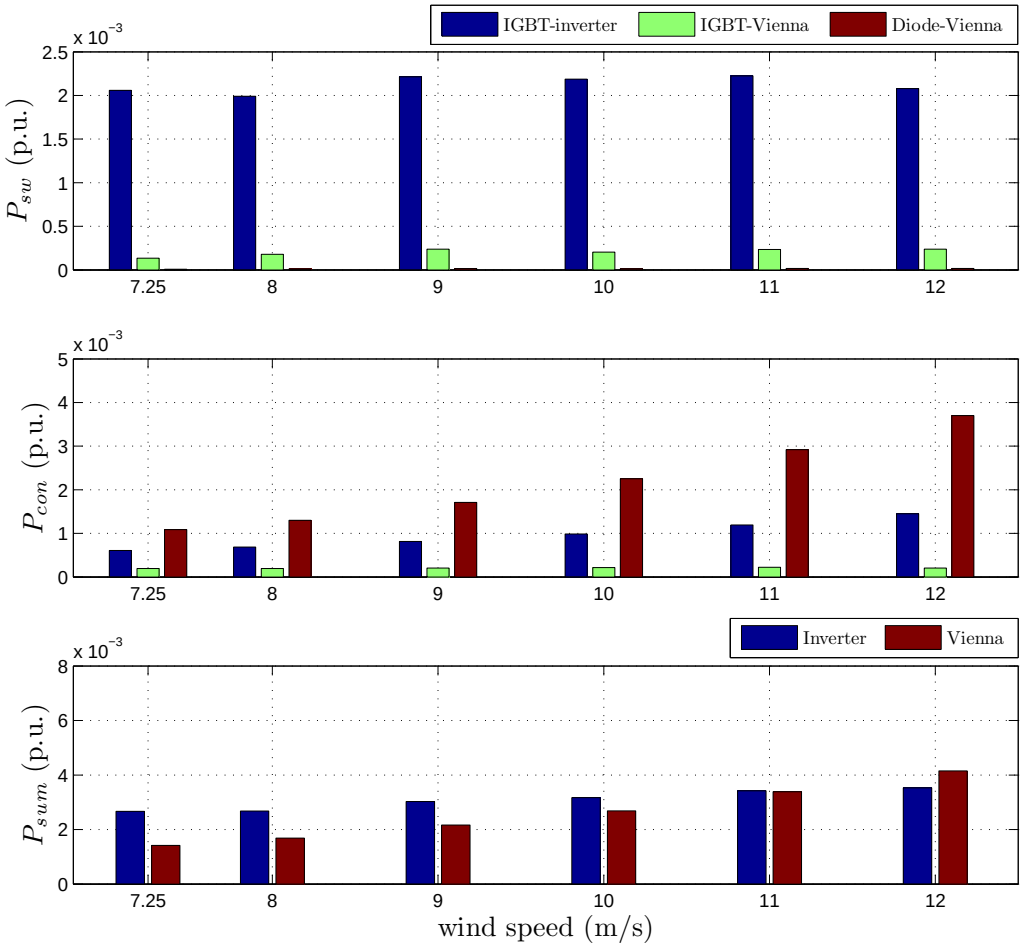

Figure 2.11 Loss comparison between inverter and Vienna rectifier in Case 2.

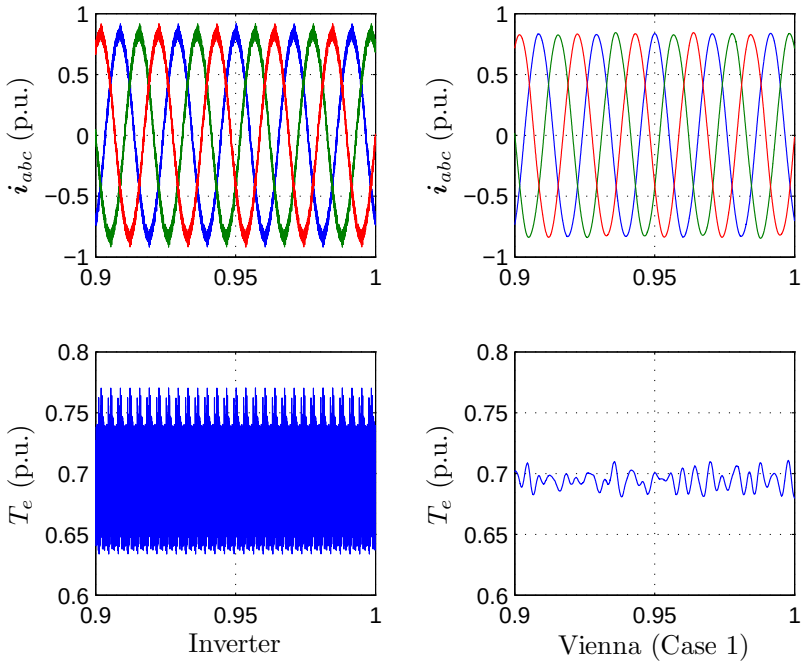

Figure 2.12 Machine currents and torque comparison ($v_w = 10$ m/s).

diodes in Case 2 is half of that in Case 1, the switching loss in Case 2 decreases remarkably compared with Case 1. The amount of decrease of conduction loss is apparent in the high wind speed range because the current through the IGBTs and diodes in Case 2 is lower than that in Case 1 (refer to $|\tilde{I}|$ in Figs. 2.6 and 2.8). The total loss of Case 1 is greater than that of the inverter in the high wind speed range due to high conduction loss of diodes. Case 2 has lower total loss because of the significant decrease of switching and conduction loss. Note that the decrease of IGBT switching and conduction loss in the Vienna rectifier, especially for Case 2, can reduce the thermal stress of the IGBTs and further improve the reliability of the IGBT modules [64,65]. Moreover, for this wind energy conversion application, the Vienna rectifier would be overall more efficient, because of the inherent probabilistic distribution of wind speeds (that is, operation at rated power does not occur as often as operation at reduced power levels).

Herein, since the above loss comparison is used to demonstrate the characteristics and performance advantage of the Vienna rectifier, the loss of the LC filter is not considered. On the other hand, because of the LC filter, the current through the machine in the proposed

system has much lower harmonic content than in a conventional system. This helps reduce generator losses and torque pulsation (Fig. 2.12).

2.6 Conclusions

A novel variable-speed WECS utilizing a squirrel-cage induction machine and a Vienna rectifier has been proposed. A capacitor bank is necessary to make the voltage and current at the AC side of the Vienna rectifier satisfy an angle constraint. The influence of the choice of capacitance on the operational behavior of the machine and the rating of power semiconductor switches has been investigated. The switching and conduction loss of the power semiconductors in the Vienna rectifier were characterized by simulations. These preliminary results show that the proposed system has potential to be more efficient and reliable compared to a conventional system.

There are still numerous issues that need to be investigated in more detail, such as: the experimental verification, the effect of the Vienna rectifier upon the machine performance; control strategies and optimal modulation methods to improve system dynamics; the buildup of the capacitor voltage during the start-up process; ways to increase the operational speed range by fine-tuning the electric machine design; and the interface with the power grid.

CHAPTER 3. ANALYSIS OF SQUIRREL-CAGE INDUCTION GENERATOR WITH VIENNA RECTIFIER FOR WIND ENERGY CONVERSION SYSTEM

A paper published in the *IEEE Transactions on Energy Conversion*, Vol. 26, No. 3, pp. 967-975, Sep. 2011.

Hao Chen[1] and Dionysios C. Aliprantis

3.1 Abstract

This paper analyzes a topology consisting of a squirrel-cage induction machine and a Vienna rectifier for a wind energy conversion system. Simulation results reveal that this configuration is advantageous with respect to energy efficiency compared to a traditional six-switch two-level converter. In addition, it can have higher reliability, due to reduced blocking voltage stress across the semiconductors. The theoretical analysis and feasibility of the proposed configuration are validated by experimental results obtained from a prototype system.

3.2 Introduction

Variable-speed wind energy conversion systems (WECS) are commonly used because they allow maximum energy extraction from the wind. Configurations using various machine types, such as squirrel-cage induction generators, doubly-fed induction generators (DFIG), and permanent magnet synchronous generators (PMSG) have been studied extensively in the past and are still subject of active research [4, 5, 49, 50, 66]. Even though today's commercial MW-scale wind turbines are mostly DFIG- or PMSG-based, there are cases where squirrel-cage induction

[1]Primary researcher and author

generators are a good solution, such as in isolated power systems [67]. The squirrel-cage machine is a relatively inexpensive motor, it is quite robust, and requires minimum maintenance. In addition, recently there has been a shortage in the supply (and a significant increase in the demand) of rare earth minerals that are used in PMSG machines, which is expected to drive their prices upwards. Hence, generators that are not permanent-magnet based (such as the squirrel-cage machine) are gaining renewed interest.

For the turbine's power electronics interface with the power system, back-to-back six-switch two-level PWM converters are used in the majority of cases [6]. Multi-level converters, such as the back-to-back three-level neutral-point-clamped converter, have been proposed as well [7,8]. The utilization of multi-level converters can lead to designs with higher power ratings and improved power quality. However, the large number of power switches significantly increases cost and control complexity [9].

The three-phase/three-switch/three-level PWM rectifier [10] (called the "Vienna" rectifier), has been applied mostly as a power supply module and as an active front-end stage in motor drives [11]. The Vienna rectifier can generate three voltage levels with decreased number of power switches (only three) thus simplifying the control and reducing cost (although more diodes are needed). Also, it leads to reduced blocking voltage stress on the power semiconductors, which can enhance reliability.

In this paper, a novel WECS topology with a squirrel-cage induction generator and a Vienna rectifier is proposed, and its operation is analyzed in detail.[2] This topology was first introduced in [68], and could be used in wind turbines of practically any rating. Herein, the analysis of [68] is extended to the case of an induction generator with main flux path saturation (Section 3.3). A case study is devised to demonstrate the operation of the system under a wide speed range (Section 3.3.3). The proposed configuration is compared to the conventional six-switch two-level converter system by way of simulations (Section 3.4), which show that the Vienna rectifier topology has better efficiency, and the potential for better reliability. Finally, experimental results on a prototype generator drive are provided that validate the operation

[2]The design of the maximum power point tracking and blade pitching control loops is not discussed in this paper, which focuses entirely on the analysis of the electromechanical energy conversion system.

of the system (Section 4.5). It should be noted that a Vienna rectifier/PMSG configuration was recently proposed and studied (using simulation results only) in [69]. Our results are in agreement with the conclusions of [69], namely, that the Vienna rectifier provides a more efficient power electronics topology than the classical two-level PWM converter. The proposed induction generator/Vienna rectifier topology constitutes a new promising design option, which should be evaluated closely by the wind energy industry.

3.3 Steady-State Analysis

In the analysis that follows, it is assumed that the wind turbine is operating under maximum power point tracking control, in a hypothetical quasi-steady-state mode of operation. Also, the induction generator is controlled using the rotor field-oriented control scheme. Equations are derived that relate all of the machine's steady-state variables to rotor speed, which is proportional to the prevailing wind speed. This enables the study of the system's performance as a function of wind speed (a single degree of freedom). Of particular interest is the generator's input impedance.

The proposed configuration is shown in Fig. 3.1. The use of an LC filter is dictated by a constraint imposed by the Vienna rectifier. Moreover, the capacitor bank is necessary for the self-excitation of the induction machine. The capacitors cannot be charged from the energy stored in the dc link using the Vienna rectifier, because this is a unidirectional converter. The self-excitation of an induction machine is a well known phenomenon, so it will not be explained further in this paper. For the purposes of this analysis, self-excitation is predicted analytically using the method of [70].

The topology of the three-phase/three-switch/three-level PWM ("Vienna") rectifier is depicted in Fig. 4.1. Herein, we consider the electromechanical system until the dc bus, which is assumed to maintain a constant dc voltage. The dc bus can be connected to a conventional six-switch or other type of inverter. Alternatively, it could be connected to a dc collection system, such as the ones that have been proposed to establish dc grids in offshore wind farms with HVDC transmission [20, 51, 52].

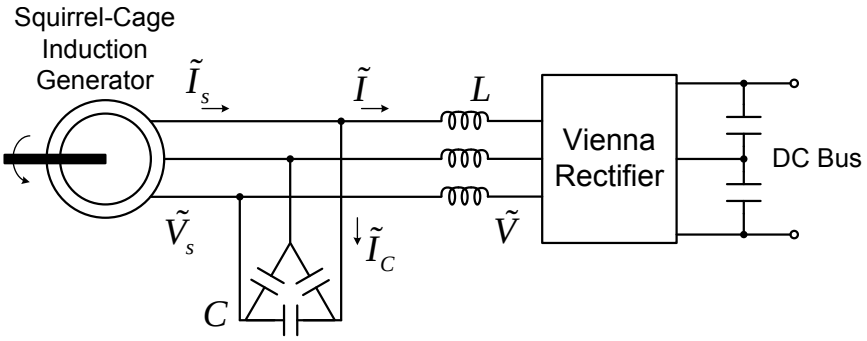

Figure 3.1 Proposed configuration.

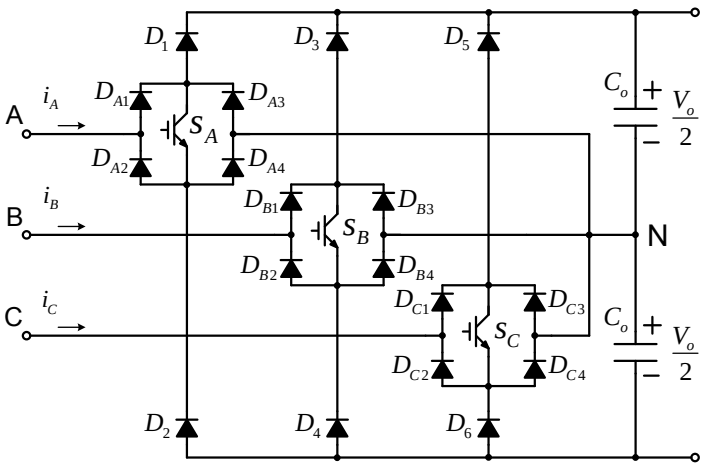

Figure 3.2 Power circuit of a Vienna rectifier.

3.3.1 Wind Turbine and Induction Generator

The mechanical power P_m extracted from the wind by a turbine can be expressed as [48]:

$$P_m = \tfrac{1}{2}\rho\pi R_w^2 c_p\left(\lambda,\gamma\right) v_w^3\,, \tag{3.1}$$

where v_w is the upstream wind speed, ρ is the air density, R_w is the rotor disc radius, $c_p\left(\lambda,\gamma\right)$ is the performance coefficient, γ is the pitch angle in degrees, and λ is the tip-speed ratio given by $\lambda = \omega_w R_w / v_w$, where ω_w denotes the blades' angular velocity. In this analysis, pitching of the blades is not considered, so $\gamma = 0$, and $c_p(\lambda, 0)$ attains its maximum value $c_p^{\max}$ for an optimal λ_o. In a variable-speed wind turbine, the blades' speed is changed proportionally to the wind speed such that λ_o is always maintained, in order to extract maximum power from the wind. The relation between λ_o and the optimal wind turbine rotor speed ω_{wo} or the

corresponding generator electrical speed ω_{ro} is given by

$$\lambda_o = \frac{\omega_{wo} R_w}{v_w} = \frac{\omega_{ro}}{v_w} K_1 \,, \tag{3.2}$$

where $K_1 = (2R_w)/(GP)$, G is the gearbox ratio, and P is the number of generator poles. Using (3.2) to express v_w in terms of ω_{ro} and λ_o, (4.1) becomes

$$P_m^{\max} = K_2 c_p^{\max} \left(\frac{\omega_{ro}}{\lambda_o} K_1 \right)^3 \,, \tag{3.3}$$

where $K_2 = \frac{1}{2}\rho\pi R_w^2$. Therefore, the mechanical torque applied to the generator shaft for maximum power extraction (ignoring gearbox losses) is a quadratic speed function:

$$T_m^{\max} = \frac{P}{2} \frac{P_m^{\max}}{\omega_{ro}} = \frac{P}{2} M \omega_{ro}^2 \,, \tag{3.4}$$

where $M = K_2 K_1^3 c_p^{\max} / \lambda_o^3$.

The rotor field-oriented control [53] is adopted for the induction generator, and generator convention is used for the currents. The analysis uses standard notation for the machine parameters. The steady-state machine stator and rotor currents are expressed in the synchronous reference frame, hence the 'e' superscript. The d-axis stator current I_{ds}^e is

$$I_{ds}^e = -\frac{\Lambda_r'}{L_m} \,, \tag{3.5}$$

where Λ_r' is the machine's rated rotor flux, and $L_m = L_m(I_m)$ is a nonlinear magnetizing inductance. The qd-axes rotor currents are

$$I_{qr}'^e = -\frac{L_m}{L_r'} I_{qs}^e \;\text{ and }\; I_{dr}'^e = 0 \,. \tag{3.6}$$

The electromagnetic torque is

$$T_e = \frac{3}{2} \frac{P}{2} \frac{L_m}{L_r'} \Lambda_r' I_{qs}^e \,. \tag{3.7}$$

Since T_e is equal to $T_m^{\max}$ given by (3.4) at the steady state (friction and windage losses are ignored), the q-axis stator current I_{qs}^e can be expressed as

$$I_{qs}^e = \frac{2 L_r' M}{3 L_m \Lambda_r'} \omega_{ro}^2 \,. \tag{3.8}$$

The qd-axes magnetizing currents are given by

$$I^e_{qm} = -\left(I^e_{qs} + I'^e_{qr}\right) = -\frac{2L'_{lr}M}{3L_m\Lambda'_r}\omega^2_{ro}\,, \tag{3.9}$$

$$I^e_{dm} = -\left(I^e_{ds} + I'^e_{dr}\right) = \frac{\Lambda'_r}{L_m}\,. \tag{3.10}$$

The magnetizing flux is

$$\Lambda_m = L_m I_m\,, \tag{3.11}$$

where I_m is the magnetizing current given by

$$I_m = \sqrt{\left(I^e_{qm}\right)^2 + \left(I^e_{dm}\right)^2}\,. \tag{3.12}$$

Substitution of (3.9) and (3.10) into (3.11) and (3.12) yields

$$\Lambda_m = \sqrt{\left(\frac{2L'_{lr}M}{3\Lambda'_r}\omega^2_{ro}\right)^2 + {\Lambda'_r}^2}\,, \tag{3.13}$$

which signifies that Λ_m is a function of ω_{ro}, which in turn is proportional to wind speed. The term that is inside the parentheses remains quite small, so that $\Lambda_m \approx \Lambda'_r$ for the entire operational speed range (so the machine is not overly saturated for high speeds). An arctangent function representation is adopted to represent the relationship between Λ_m and I_m [71], which can be used to obtain I_m. Then, L_m can be calculated from $L_m = \Lambda_m/I_m$. After obtaining L_m, the machine currents can be calculated from (3.5), (3.6), and (3.8). Also, the qd-axes stator fluxes (Λ^e_{qs} and Λ^e_{ds}) can be obtained. The synchronous frequency ω_e is

$$\omega_e = \omega_{ro} + \omega_s\,, \tag{3.14}$$

where ω_s is the slip frequency, which, for the rotor field-oriented control, is given by

$$\omega_s = \frac{R'_r I^e_{qs}}{L'_r I^e_{ds}} = -\frac{2R'_r M}{3{\Lambda'_r}^2}\omega^2_{ro}\,. \tag{3.15}$$

The qd-axes stator voltages can be calculated using

$$V^e_{qs} = -R_s I^e_{qs} + \omega_e \Lambda^e_{ds}\,, \tag{3.16}$$

$$V^e_{ds} = -R_s I^e_{ds} - \omega_e \Lambda^e_{qs}\,. \tag{3.17}$$

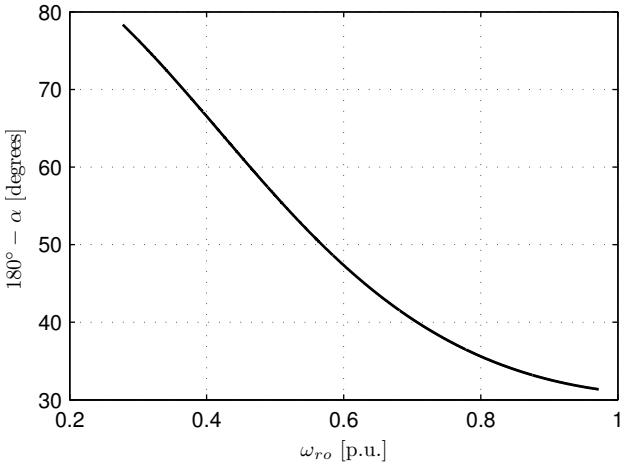

Figure 3.3 Machine input impedance angle (for rotor field-oriented control).

Finally, the input impedance of the induction machine is

$$Z = R + jX = \frac{\tilde{V}_s}{-\tilde{I}_s}\,, \tag{3.18}$$

where $\tilde{V}_s$ and $\tilde{I}_s$ are the machine's terminal voltage and current phasors given by

$$\tilde{V}_s = \frac{V^e_{qs} - jV^e_{ds}}{\sqrt{2}} \text{ and } \tilde{I}_s = \frac{I^e_{qs} - jI^e_{ds}}{\sqrt{2}}\,. \tag{3.19}$$

Note that $R < 0$ for generator action, and $X > 0$; hence, the power factor angle $\alpha = \tan^{-1}(X/R)$ is between 90° and 180°. Since $-\tilde{I}_s$ lags $\tilde{V}_s$ by α, it follows that $\tilde{I}_s$ leads $\tilde{V}_s$ by $180° - \alpha$. Figure 3.3 shows the variation of this angle as a function of ω_{ro} in per unit, where 1 p.u. corresponds to rated machine frequency (50 Hz in this example). This plot, as well as several other plots in this paper, end a little before 1 p.u., because this is where rated power output (300 kW) is obtained. The parameters of the machine and wind turbine are provided in Appendix B.1. The significance of this calculation will be explained in the next section.

3.3.2 Vienna Rectifier

In [68], it was shown that the Vienna rectifier allows the input current ($\tilde{I}$ in Fig. 3.1) to lead or lag the input voltage ($\tilde{V}$ in Fig. 3.1) by no more than 30°. The phase shift between $\tilde{V}$ and $\tilde{I}$ is denoted by β ($\beta > 0$ when current is lagging).

From Fig. 3.3, it can be seen that a Vienna rectifier cannot be connected directly with an induction generator because of its 30° angle constraint. (This plot was obtained for a given set of machine parameters, but it is representative of induction generators in general.) In other words, the Vienna rectifier cannot supply enough reactive power to the machine. One possible way to provide reactive power is by connecting a capacitor bank across the machine terminals, as shown in Fig. 3.1. The connection of an appropriately sized capacitor bank can guarantee that the angle constraint is satisfied for a relatively wide speed range [68]. However, a single capacitance level would not allow the operation of the system for a wind speed range that would be typical of modern variable-speed WECS. A method to overcome this limitation, using a switched capacitor bank, is described next.

3.3.3 System Design

Figure 3.4 shows that the choice of the LC-filter capacitance determines the operational range of the generator [68], for a given inductance value. Apparently, any single capacitance level restricts the speed range quite significantly. To overcome this limitation, and to enable variable-speed operation over a typical range of wind speeds, the use of a switched capacitor bank is proposed. The example that is illustrated in Fig. 3.4 shows a case where five capacitance levels are selected, allowing the turbine to operate from 3 m/s to 10.5 m/s, where rated power is obtained. (For wind speeds higher than 10.5 m/s, pitching of the blades would be required.) The capacitor bank is switched when the operating point comes close to the $\beta = \pm 30°$ constraint. A 2° safety margin is introduced, so that the switching occurs at $\beta = \pm 28°$. The capacitance level that is used for the highest range of rotor speeds and output powers is selected such that $\beta = 0°$ at rated power, as shown in Fig. 3.7. This ensures the best usage of the available dc-link voltage [68]. Details of the switched capacitor bank design are shown in Table 3.1, which lists the characteristics of the five delta-connected capacitor banks [72]. (As rotor speed increases, capacitor banks are gradually disconnected.) Note that the capacitors do not all need to have the same voltage rating, as is indicated in the Table. As rotor speed increases, so does the capacitor bank voltage; this is shown in Fig. 3.5, which also

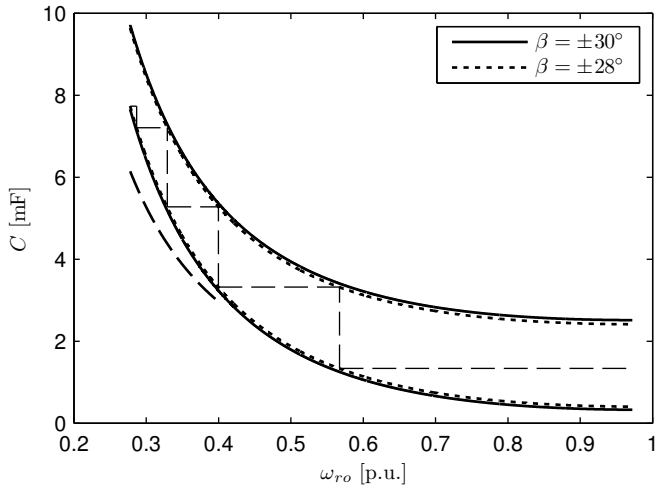

Figure 3.4 Capacitance constraint curves and switched capacitor bank levels. (Capacitance values are for a delta-connected bank. The LC-filter inductance is 0.25 mH per phase.)

Table 3.1 Capacitor Bank Design Parameters

C (mF)	max. speed (p.u.)	volt. rating (V l-l)	volume (m^3)
0.5	0.29	122	0.005
1.9	0.33	140	0.017
2.0	0.40	170	0.018
2.0	0.57	240	0.018
1.3	1.0	417	0.035

includes the machine terminal current variation. Base voltage and current values correspond to the generator's rated quantities (see Appendix B.1).

Figure 3.6 depicts voltage and current at the Vienna rectifier terminals. It is interesting to note that the current flowing through the Vienna rectifier is lower than the machine current for the entire speed range (because the capacitors provide a significant component of reactive current). This will impact the conduction loss in the power electronics.

The heavy dashed line in Fig. 3.4 reflects the minimum capacitance required for self-excitation for a range of speeds [70]. Since this curve is below the $\beta = -30°$ constraint curve, the machine will self-excite from a low speed. Once the voltage at the machine terminals is established, then the Vienna rectifier can be safely engaged.

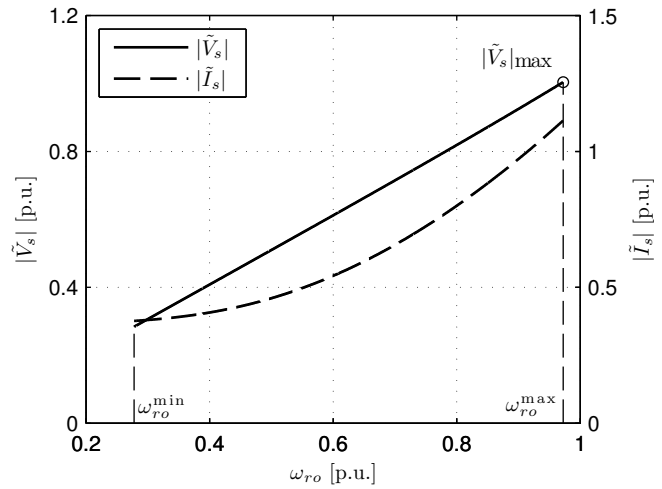

Figure 3.5 Variation of voltage and current at the generator terminals.

Finally, to complete the system design, one needs to determine the necessary dc-link voltage level of the Vienna rectifier. From [68], the dc-link voltage level must satisfy the following constraint:

$$V_o \geq 2\sqrt{6}\cos(60^\circ - |\beta|)|\tilde{V}|\,. \tag{3.20}$$

This is plotted in Fig. 3.8, which reveals that the maximum voltage occurs at $\omega_{ro} = 0.57$ p.u.

3.4 Power Electronics Energy Loss Analysis

To evaluate the energy loss of the power electronics, the proposed topology is compared to a conventional system of an induction generator driven by a six-switch two-level converter (without an LC filter, which is not typically used in this case). The simulations are run using Matlab/Simulink and PLECS [59]. To obtain a fair comparison, the two systems are designed with similar components. For the six-switch converter in the conventional system, the space vector modulation is used to control the machine's terminal voltage, with a switching frequency of 3 kHz. For the Vienna rectifier, the delta-hysteresis modulation [53] is used to control the currents (see Fig. 3.11). The hysteresis band width is set to $h = 0.02$ pu, and the sampling frequency is 20 kHz. The average switching frequency throughout the entire operating range is on the order of 2–5 kHz, as shown in Fig. 3.9. The dc-link voltage for both systems is set to 700 V. For the Vienna rectifier, this choice is mandated by (3.20), with a safety margin

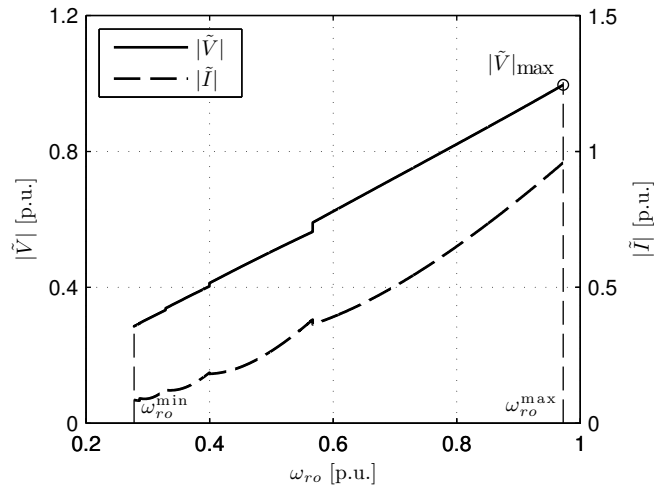

Figure 3.6 Variation of voltage and current at the Vienna rectifier terminals.

of approximately 20%. This voltage level is also sufficient for the classical six-switch inverter, which needs to supply the machine voltage profile shown in Fig. 3.5.

Based on the voltage and current requirements, the POWEREX CM800HA-34H (800 A/1700 V) single IGBT module [60] can be used to construct the six-switch converter. For the Vienna rectifier (see Fig. 4.1), the CM800HA-34H is selected for the power switches S_A, S_B, and S_C. Note that the free-wheeling diode in the IGBT module does not conduct current. The POWEREX QRS0680T30 (800 A/600 V) fast-recovery diode module [73] is selected for diodes D_k ($k = 1, ..., 6$), whereas the POWEREX PS410625 (2500 A/600 V) slow-recovery diode module [74] is selected for diodes D_{Ai}, D_{Bi}, and D_{Ci} ($i = 1, ..., 4$) [10]. PLECS supports the thermal modeling and simulation of semiconductors, so the switching and conduction loss can be obtained if the thermal description parameters of switches and diodes are specified in the PLECS circuits [59]. The thermal description parameters of the POWEREX components, such as on-state voltage, and turn-on and turn-off losses, can be acquired from the component data sheets and the Mitsubishi Electric Power Module Loss Simulator [63].

The switching loss P_{sw}, conduction loss P_{con}, and total loss $P_{sum} = P_{sw} + P_{con}$ of the six-switch converter and the Vienna rectifier (in per unit) are presented in Fig. 3.10. For the Vienna rectifier, the IGBTs dominate the switching loss, whereas the diodes dominate the conduction loss. The blocking voltage stress of the Vienna rectifier IGBTs and diodes is

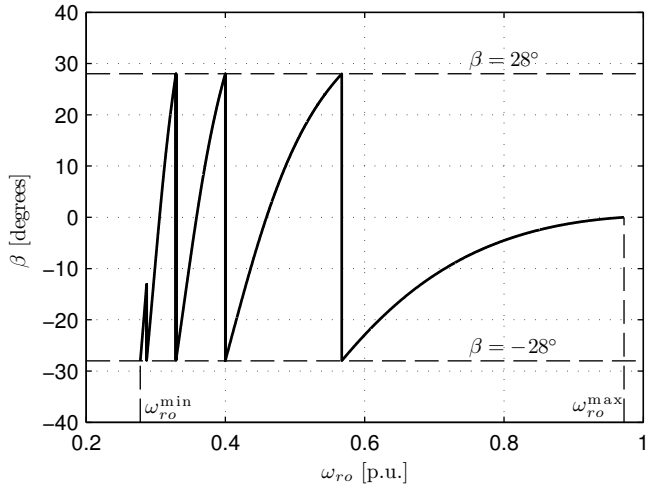

Figure 3.7 Variation of power factor angle β at Vienna rectifier terminals.

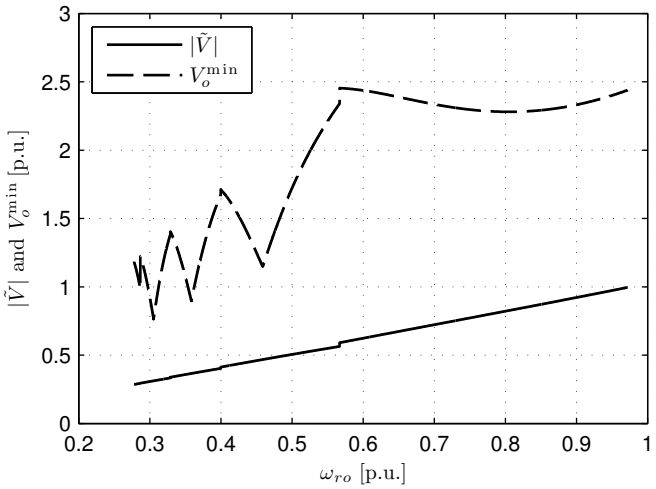

Figure 3.8 DC-link voltage requirement.

only half of the voltage stress in the six-switch converter. This leads to significantly reduced switching loss [75], as can be observed from the topmost plot (where the gray bars are almost imperceptible). However, due to the larger number of diodes used in the Vienna rectifier, the conduction loss is substantial, as can be seen in the middle plot. Overall, the Vienna rectifier has lower loss for the entire speed range, as is apparent from the bottom plot. It should be noted that the decrease of IGBT switching and conduction loss in the Vienna rectifier can reduce the thermal stress of the IGBTs, and thus further improve the reliability of the IGBT modules [64, 65].

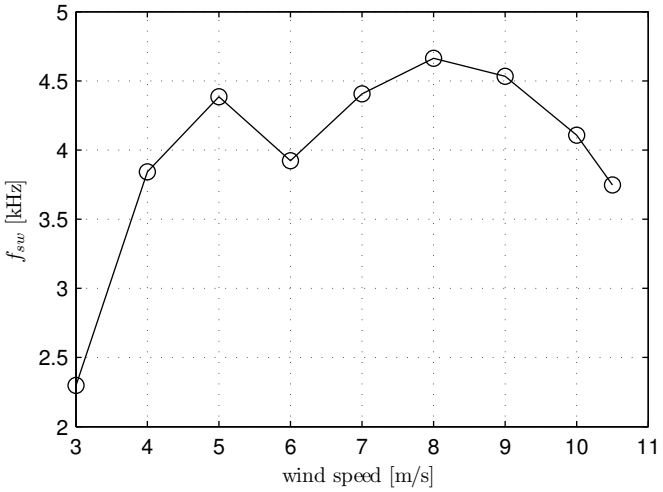

Figure 3.9 Average switching frequency of Vienna rectifier with delta-hysteresis current modulation for various wind speeds.

It is possible to estimate the annual energy loss of the power electronics by taking into account the statistics of wind speed. Usually, the Weibull probability density function is used to describe the variation of wind speed over a year [76]. The Weibull distribution is defined using two parameters, namely, a scale parameter c, and a shape parameter k. For this analysis, the parameters are $k = 2$ and $c = 7.2$ m/s. The annual energy loss can be estimated by

$$E_{\text{loss}} = \int_{v_{\min}}^{v_{\max}} 8760 P_{\text{loss}}(v_w) f(v_w) dv_w \,, \tag{3.21}$$

where $v_{\min}$ and $v_{\max}$ are wind speed limits, P_{loss} is the converter power loss, and f is the Weibull distribution. The integral in (4.18) is evaluated numerically, using the trapezoidal rule and the discrete points that were obtained previously. The wind speed varies from 3 m/s to 15 m/s, and blade pitching is assumed to occur above the rated wind speed of 10.5 m/s. (For wind speeds higher than rated, the generator and power electronics operate at the same point as for 10.5 m/s.)

The annual energy losses of the Vienna rectifier and six-switch converter are given in Table 4.1, in absolute numbers and as a percentage of the total generated energy. The results suggest that, for this example, the Vienna rectifier is a slightly more efficient solution. This conclusion cannot be generalized to all possible cases, because the answer depends on a large number of case-specific parameters. A more thorough comparison is worthwhile, and is left for

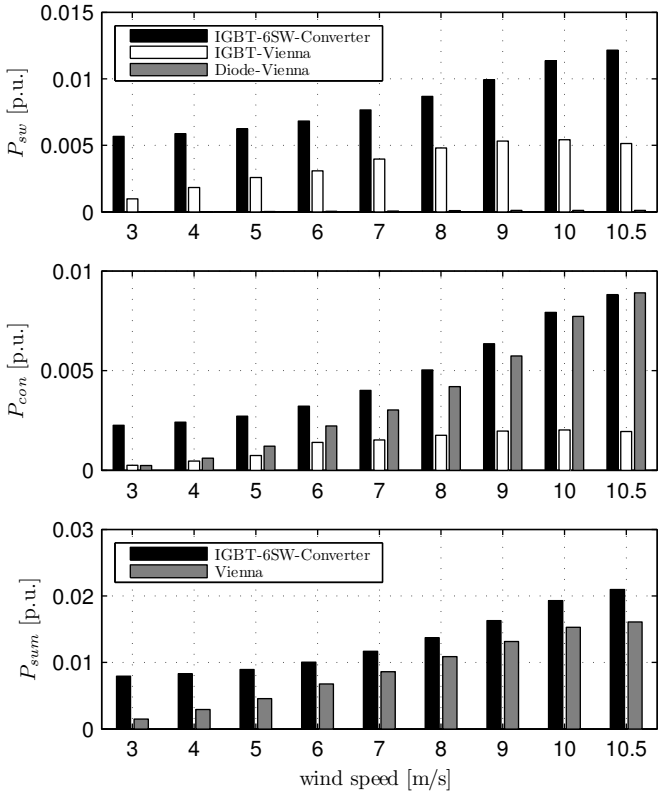

Figure 3.10 Loss comparison between six-switch converter and Vienna rectifier.

Table 3.2 Energy Loss Comparison

	loss (MWh)	loss (%)
6-switch converter	27.72	3.44%
Vienna rectifier	18.82	2.33%

future work. In addition, the loss of the *LC* filter has not been taken into account. However, the *LC* filter does absorb a substantial amount of harmonics, which would otherwise flow in the generator windings. Therefore, there occurs a shift of harmonic power loss from the generator to the *LC* filter, which is difficult to quantify (because it will affect both ohmic and core losses), and should also be more carefully investigated. The reduction of harmonic currents in the generator also helps reduce the high-frequency electromagnetic torque pulsation, which could be an additional factor of drivetrain fatigue in a WECS.

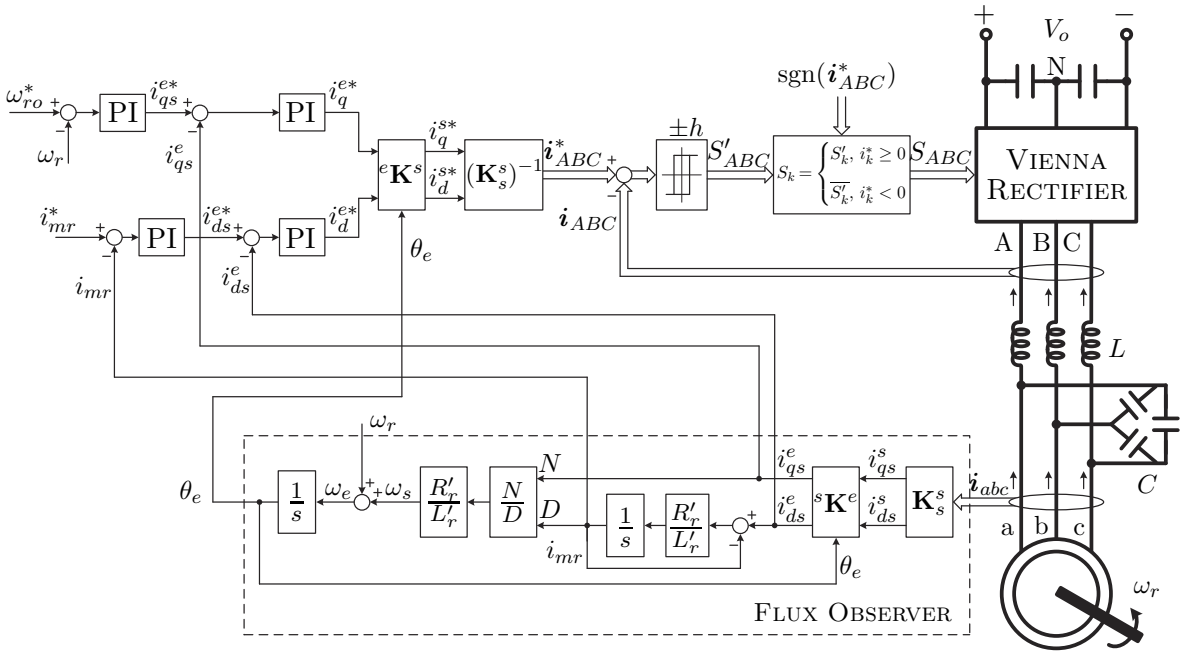

Figure 3.11 Control block diagram for the induction generator driven by the Vienna rectifier.

3.5 Experimental Results

To verify the feasibility of the proposed topology, a small-scale prototype has been implemented in the laboratory. A separately excited dc machine was used as a prime mover. The parameters of the experimental setup are provided in Appendix B.2. A programmable dc power source was used to supply the dc-link voltage of the Vienna rectifier (V_o = 400 V). Resistors were connected in parallel with the dc-link capacitors, to absorb the generated power. The control scheme shown in Fig. 3.11 was implemented on a dSPACE DS1103 system.

It is important to note that this experimental topology does not emulate the torque-speed characteristics of a WECS. Therefore, the results obtained in this section should not be compared with the theoretical curves of Section 3.3. The dc machine armature and field winding voltage were 96.5 V and 129 V, respectively. The torque-speed characteristic of this configuration is linear, and the speed control loop of Fig. 3.11 was deactivated.

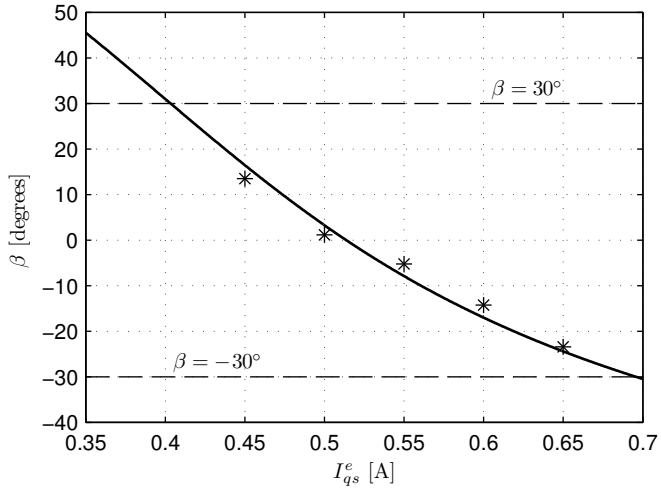

Figure 3.12 Variation of power factor angle β at Vienna rectifier terminals.

3.5.1 Steady-State

In this experiment, the rotor magnetizing current reference, i^*_{mr}, was set to -1.1 A (minus sign because of generator convention for currents), and the q-axis stator current reference, i^{e*}_{qs}, was consecutively set to 0.45 A, 0.5 A, 0.55 A, 0.6 A, and 0.65 A. For each value of i^{e*}_{qs}, the power factor at the ac side of the Vienna rectifier was acquired using a power analyzer, from which β was obtained; the experimental results are shown as stars in Fig. 3.12, and the theoretically predicted variation is superimposed as a solid line. The experimental results match the theoretical analysis quite well. During the experiments, when i^{e*}_{qs} was further increased towards 0.7 A or decreased towards 0.4 A, the rotor speed became unstable and the Vienna rectifier was unable to drive the induction generator, because the $\pm 30°$ angle constraint was violated.

Figure 3.13 shows the generator's phase-a current i_a, the generator's line-to-line voltage v_{ab}, the Vienna rectifier's phase-A current i_A, and the Vienna rectifier's line-to-line voltage v_{AB}, for $i^{e*}_{qs} = 0.5$ A. It can be seen that the voltage across the generator's terminals is almost free of harmonics due to the presence of the LC filter.

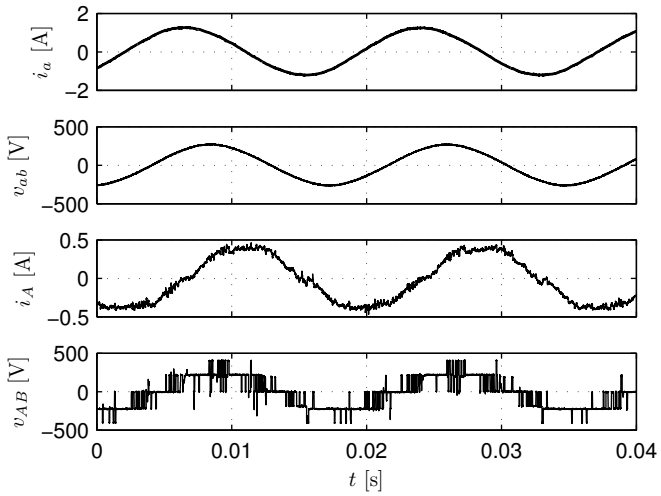

Figure 3.13 Steady state waveforms: $i_{qs}^{e*} = 0.5$ A and $i_{mr}^{*} = -1.1$ A.

3.5.2 Transient Behavior

In this experiment, the operation of the controller is validated with a transient study. The magnetizing current command i_{mr}^{*} was set to -1.1 A and i_{qs}^{e*} was stepped from 0.65 A to 0.45 A at $t \approx 0.7$ s. Figure 5.14 depicts the transient response. Shown are the stator currents in the synchronous reference frame, i_{qs}^{e}, i_{ds}^{e}, the LC-filter current commands, i_{q}^{e*}, i_{d}^{e*}, and the rotor speed, ω_r. The rotor speed increased since the electromagnetic torque of the generator was decreased.

3.6 Conclusions

A novel variable-speed WECS consisting of a squirrel-cage induction generator and a Vienna rectifier has been proposed and analyzed. An LC filter based on a switched capacitor bank is utilized to obtain a wide speed operational range. The switching and conduction losses of the power semiconductors in the Vienna rectifier were obtained by simulations, and compared to the losses incurred by a similar six-switch converter. The results show that the proposed system has potential to be more efficient and reliable. Finally, the proposed topology and control algorithm were experimentally validated on a small-scale prototype.

This appears to be a promising topology that should be investigated in more depth. Im-

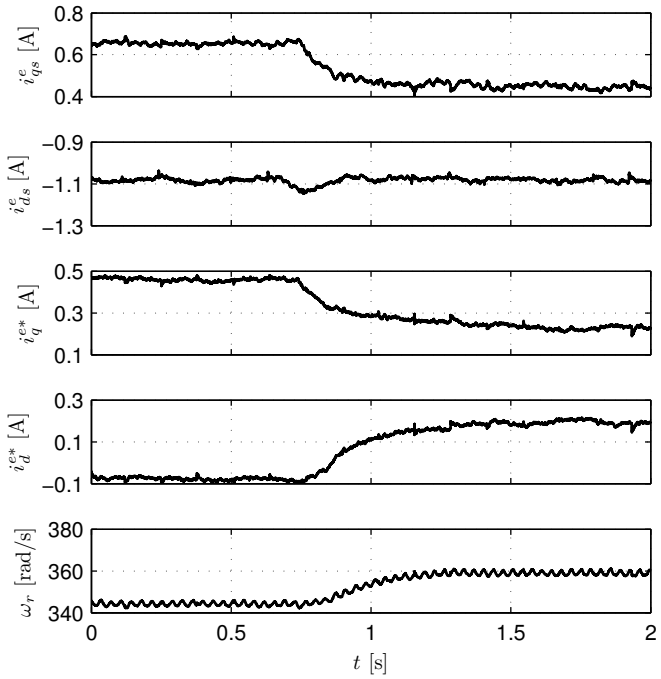

Figure 3.14 Transient waveforms (i^{e*}_{qs} step change from 0.65 A to 0.45 A).

portant questions that remain unanswered are related to the economic considerations of this topology versus a more classical one; the effect of the Vienna rectifier on the machine performance, including an accurate determination of harmonics-related losses on the machine and the *LC* filter; a detailed system-level energy loss comparison that includes all components; the quantification of the possible reliability enhancement due to the reduced voltage stress on the switches; alternate control strategies and optimal modulation schemes; increasing the operational speed range and/or reducing capacitive requirements by fine-tuning the electric machine design and its parameters; the impact of the capacitor switching transients on the electric generator; and a study of the benefits of eliminating high-frequency torque vibrations from the wind turbine drivetrain.

CHAPTER 4. ANALYSIS OF PERMANENT-MAGNET SYNCHRONOUS GENERATOR WITH VIENNA RECTIFIER FOR WIND ENERGY CONVERSION SYSTEM

A paper accepted by the *IEEE Transactions on Sustainable Energy*

Hao Chen[1], Nicholas David, and Dionysios C. Aliprantis

4.1 Abstract

This paper analyzes a topology consisting of a permanent-magnet synchronous generator and a Vienna rectifier for a wind energy conversion system. A control strategy leading to maximum efficiency is proposed. Simulation results reveal that this configuration is advantageous with respect to energy efficiency compared to a traditional six-switch two-level converter. Experimental results are provided to demonstrate the feasibility of the proposed system.

4.2 Introduction

Variable-speed wind energy conversion systems (WECS) are widely used since they allow maximum power extraction from the wind. Configurations using various machine types, such as squirrel-cage induction generators (SCIG), doubly-fed induction generators, and permanent magnet synchronous generators (PMSG) have been studied extensively in the past and are still subject of active research [50, 67, 77–79]. Among different types of variable-speed WECS, PMSG-based turbines are attractive because of higher power capacities and energy efficiency, and good grid support capability [80–82].

[1]Primary researcher and author

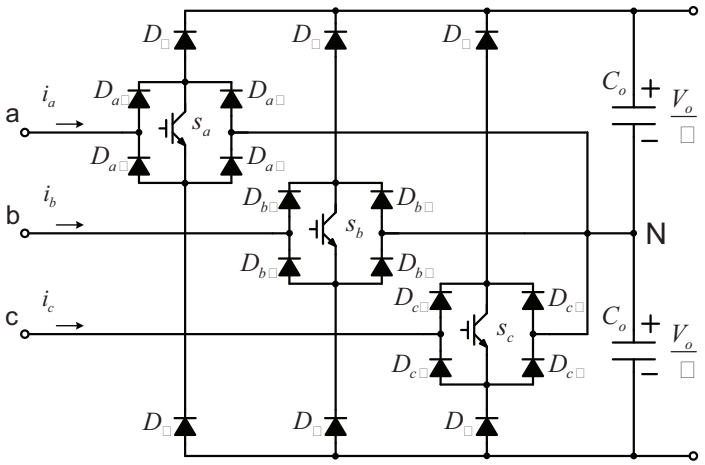

Figure 4.1 Power circuit of a Vienna rectifier.

Usually, PMSG-based WECS use back-to-back full-scale power converters (generator-side and grid-side converter) to interface with the power system. For the generator-side converter, uncontrolled three-phase diode rectifiers and six-switch two-level PWM converters have been utilized [32, 83]. However, due to higher generator current distortion induced by the diode rectifier, the six-switch converter is the prevailing choice [6].

The three-phase/three-switch/three-level PWM rectifier (commonly called the "Vienna" rectifier), whose power circuit is shown in Fig. 4.1, has been applied mostly as a power supply module and as an active front-end stage in motor drives [10, 11]. The Vienna rectifier can generate three voltage levels (line to dc-link neutral) with only three power switches, thus simplifying the control, reducing cost (although more diodes are needed), and improving power quality. In addition, it results in reduced blocking voltage stress on the power semiconductors, which can enhance reliability.

Recently, the Vienna rectifier has been proposed as the generator-side converter for either SCIG- or PMSG-based WECS [69, 84, 85]. In particular, Rajaei et al. in [69] propose a PMSG/Vienna rectifier configuration for a WECS, as shown in Fig. 4.2. The Vienna rectifier is used as the generator-side converter, which is commonly a six-switch two-level converter. Because the Vienna rectifier is a unidirectional converter, it cannot be used as a grid-side interface. Rather, a conventional six-switch converter or a multi-level converter can be used.

In [69], time-domain simulation results that demonstrate the system's functionality are

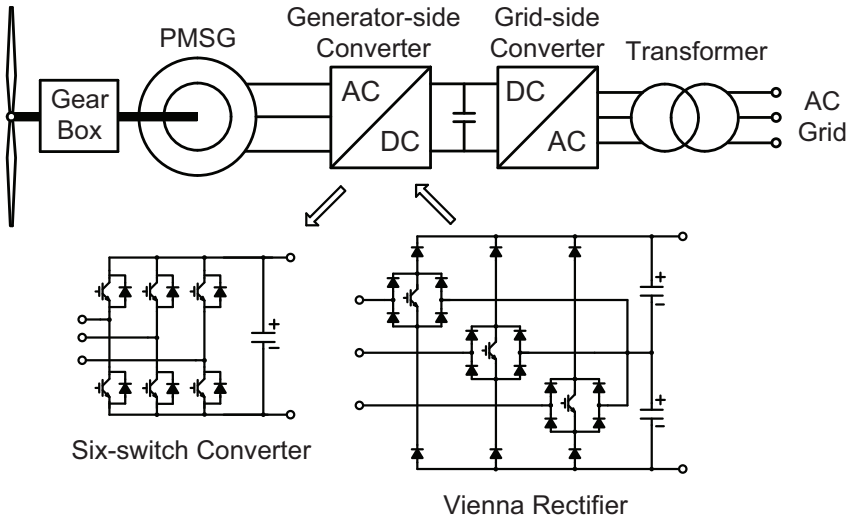

Figure 4.2 The PMSG/Vienna rectifier WECS topology. [In a direct-drive turbine, the gearbox will not be present. Also not shown is the chopper circuit commonly used in the dc-link to dissipate power in case of grid-side faults.]

provided; however, a mathematically rigorous analysis of the system has not been performed. The primary objective of this paper is to fill this gap, i.e., to determine the feasible operating region of the PMSG/Vienna configuration, which is studied in detail in Section 5.4.1.[2] The paper's second objective is to design a maximum-efficiency control strategy within the feasible operating region, which is discussed in Section 4.4. Experimental results on a small-scale prototype are provided in Section IV. Section 4.6 concludes the paper. Our results are in agreement with the conclusions of [69, 86–88], namely, that the Vienna rectifier provides a more efficient power electronics topology than the classical two-level PWM converter. Hence, the PMSG/Vienna rectifier topology constitutes a new promising design option, which should be evaluated closely by the wind energy industry.

4.3 Determination of Feasible Operating Region

In this section, the PMSG/Vienna configuration is analyzed in the steady state. The objective is to illustrate how the system's operation is constrained by current and voltage

[2]The design of the blade pitching control loops is not discussed in this paper, which focuses on the analysis of the electromechanical energy conversion system.

limits. Here, it is implied that a grid-side converter is in place. However, this is not considered in the ensuing analysis, because it does not affect the steady-state operation (a dc-link with sufficiently large capacitance essentially decouples the two converters). Nevertheless, it would be necessary to consider both converters in dynamic simulation studies that involve grid-side faults.

First, consider the well-known expression of mechanical power extracted from the wind by a horizontal-axis wind turbine [48]

$$P_m(v_w) = \frac{1}{2}\rho A c_p\left(\lambda, \gamma\right) v_w^3 \,, \tag{4.1}$$

where v_w is the upstream wind speed, ρ denotes the air's density, A is the area swept by the blades, $c_p\left(\lambda, \gamma\right)$ is the performance coefficient, γ is the blades' pitch angle, and λ is the tip-speed ratio. Typically, for a variable-speed wind turbine operating between its cut-in and rated speeds, the blades are not pitched ($\gamma = 0$), and the rotational velocity is changed proportionally to the wind speed in order to extract maximum power from the wind. In this operating mode, the electromagnetic torque command can be a quadratic speed function [85, 89]:

$$T_e^*(\omega_r) = C\omega_r^2 \,, \tag{4.2}$$

where C is a constant, and ω_r is the (measured) electrical rotor speed. (This control strategy ensures stable operation around the optimal power-speed curve, even during transient aerodynamic conditions.) For wind speeds higher than the rated speed, the pitch angle of the blades is controlled in order to maintain constant (rated) power output. However, as far as the generator is concerned, if the oscillations around the rated operating point are ignored, its operating condition remains essentially the same. In the ensuing analysis, mechanical dynamics are ignored, and the electrical generation subsystem is assumed to remain in a steady state. In MW-scale wind turbines, due to their relatively large rotor inertia and the slow time constants of the pitch angle dynamics compared to the electrical generator subsystem, this assumption leads to negligible error.

The steady-state model of a PMSG consists of the following voltage equations in the rotor's reference frame, using generator convention for the stator currents and standard symbols for

electrical parameters [53]:

$$V_{qs}^r = -R_s I_{qs}^r + \omega_r \left(-L_d I_{ds}^r + \lambda_m\right) , \tag{4.3}$$

$$V_{ds}^r = -R_s I_{ds}^r + \omega_r L_q I_{qs}^r . \tag{4.4}$$

The electromagnetic torque T_e (positive for generator action and $\omega_r > 0$) is

$$T_e = \frac{3}{2} p \left[\left(L_q - L_d\right) I_{qs}^r I_{ds}^r + \lambda_m I_{qs}^r\right] , \tag{4.5}$$

where p is the number of the generator's magnetic pole pairs. The generator's qd-axes currents, I_{ds}^r and I_{qs}^r, are controlled to obtain the appropriate torque, $T_e = T_e^*(\omega_r)$. The parameter values used to generate the results herein are provided in Appendix C.1.

Current and voltage limits (of fundamental components, neglecting higher-order harmonics) can be expressed by

$$\left(I_{qs}^r\right)^2 + \left(I_{ds}^r\right)^2 \leq \left(I_{s\,\max}\right)^2 , \tag{4.6}$$

$$\left(V_{qs}^r\right)^2 + \left(V_{ds}^r\right)^2 \leq \left(V_{s\,\max}\right)^2 , \tag{4.7}$$

where $I_{s\,\max}$ is the maximum stator current (in terms of peak value) and $V_{s\,\max}$ is the maximum stator voltage (line-to-neutral, peak value) that the stator-side converter can generate depending on the dc-link voltage V_o. The current limit (4.6) represents a fixed circle on the I_{ds}^r–I_{qs}^r plane. The voltage limit (4.7), in general, is represented by a speed-dependent curve on the plane.

Before proceeding to the analysis of the PMSG/Vienna rectifier configuration, it is instructive to analyze the PMSG connected to a conventional six-switch two-level converter. The voltage limit for a non-overmodulated converter is $V_{s\,\max} = V_o/\sqrt{3}$. Combining (4.3), (4.4), and (4.7) leads to an ellipse that is (approximately, after neglecting stator resistance) defined by

$$\frac{\left(I_{ds}^r - \frac{\lambda_m}{L_d}\right)^2}{\left(\frac{1}{L_d}\right)^2} + \frac{\left(I_{qs}^r\right)^2}{\left(\frac{1}{L_q}\right)^2} = \left(\frac{V_{s\,\max}}{\omega_r}\right)^2 . \tag{4.8}$$

Two voltage limit ellipses for $\omega_{r1} = 0.8$ p.u. and $\omega_{r2} = 1$ p.u. are shown in Fig. 4.3.[3] The two corresponding equal-torque contours, $T_{e1} = T_e^*(\omega_{r1})$ and $T_{e2} = T_e^*(\omega_{r2})$, are also shown. The required level of torque can be obtained by selecting any (I_{ds}^r, I_{qs}^r) pair along an equal-torque contour. It can be seen that for relatively low torque (i.e., low wind and rotor speeds), the voltage limit ellipse encloses the current limit circle, so the possible qd-axes currents are constrained by the current limit circle only; these limits are marked as Points A and B. However, with increasing torque (i.e., higher wind speeds), the voltage limit ellipse shrinks, and after a point the currents along an equal-torque contour will be constrained by both the voltage limit ellipse and the current limit circle; these are marked as Points C and D for ω_{r2}. The coordinates of the intersection points A, B, C, D can be determined either by solving a set of equations (if possible, e.g., when finding the intersection of the current limit circle with the torque hyperbola) or numerically, if the equations are intractable. It is then straightforward, by repeating this process, to draw a feasible "current selection region" diagram for the entire torque range, such as the one depicted by area (EFGHI) in Fig. 4.4. This diagram can be interpreted as follows: for each $T_e^*(\omega_r)$, the intersections of the equal-torque contour and the perimeter of the current selection region provide the outer limits for the currents (I_{ds}^r, I_{qs}^r).

If a Vienna rectifier is used instead of a six-switch converter, the current phasor ($\tilde{I}_s = I_s\angle -\phi$ in Fig. 4.2) cannot lead or lag the line-to-neutral voltage phasor ($\tilde{V}_s = V_s\angle 0$ in Fig. 4.2) by more than 30° [85]. Therefore, it is necessary to examine the impact of this constraint on the operating range of the PMSG-Vienna configuration. To this end, the power factor is calculated based on the active and reactive powers generated from the stator, which are

$$P_s = \frac{3}{2}\left(V_{qs}^r I_{qs}^r + V_{ds}^r I_{ds}^r\right) , \tag{4.9}$$

$$Q_s = \frac{3}{2}\left(V_{qs}^r I_{ds}^r - V_{ds}^r I_{qs}^r\right) . \tag{4.10}$$

For generator operation, $P_s > 0$, whereas Q_s can be positive, zero, or negative. Ignoring the

[3] To generate this and subsequent plots, a nonzero R_s has been considered in the voltage limit calculation for higher accuracy; this rotates slightly the non-resistive voltage limit ellipses, but their shape is still elliptical. Also, a 200-V safety margin is taken into account (i.e., the dc-link voltage is assumed to be reduced by this amount).

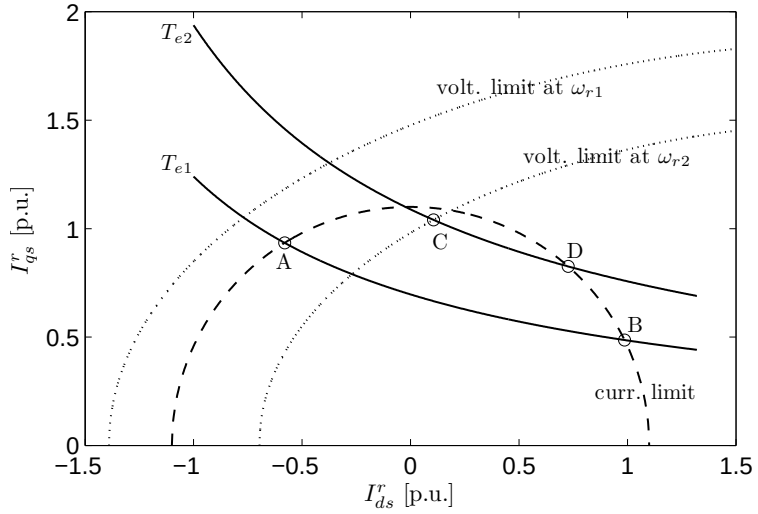

Figure 4.3 Current and voltage limits on the I^r_{ds}–I^r_{qs} plane for a PMSG with six-switch two-level converter.

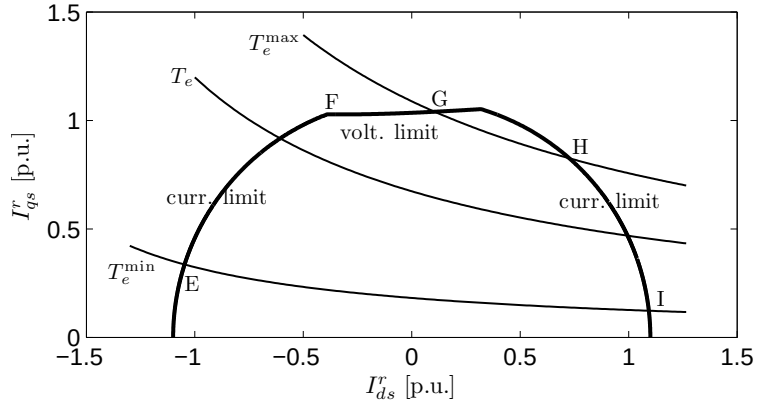

Figure 4.4 Current selection region for the PMSG with six-switch two-level converter.

stator resistance R_s, substitution of (4.3) and (4.4) into (5.10) and (5.13) yields

$$P_s = \frac{3}{2}\omega_r \left[(L_q - L_d)\, I^r_{qs} I^r_{ds} + \lambda_m I^r_{qs} \right] , \tag{4.11}$$

$$Q_s = \frac{3}{2}\omega_r \left[-L_q \left(I^r_{qs}\right)^2 - L_d \left(I^r_{ds}\right)^2 + \lambda_m I^r_{ds} \right] . \tag{4.12}$$

The tangent of the power factor angle is

$$\tan\phi = \frac{Q_s}{P_s} = \frac{-L_q \left(I^r_{qs}\right)^2 - L_d \left(I^r_{ds}\right)^2 + \lambda_m I^r_{ds}}{(L_q - L_d)\, I^r_{qs} I^r_{ds} + \lambda_m I^r_{qs}} . \tag{4.13}$$

This leads to

$$L_d \left(I^r_{ds}\right)^2 + \tan\phi\, (L_q - L_d)\, I^r_{ds} I^r_{qs} + L_q \left(I^r_{qs}\right)^2 - \lambda_m I^r_{ds} + \tan\phi \lambda_m I^r_{qs} = 0 , \tag{4.14}$$

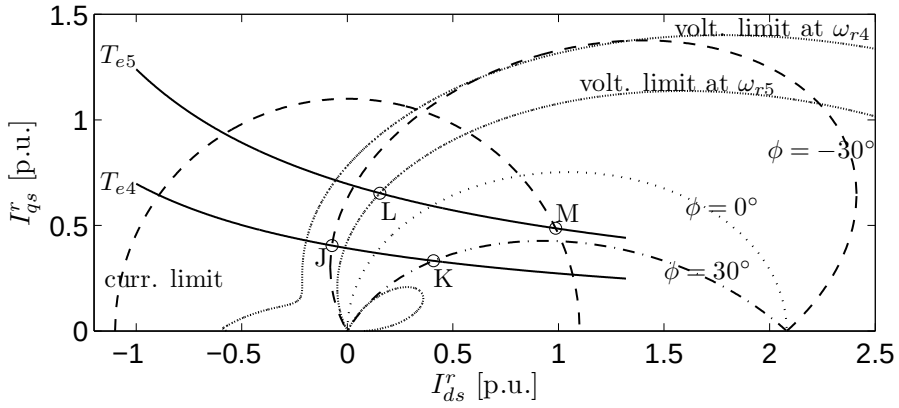

Figure 4.5 Current and voltage limits on the I_{ds}^r–I_{qs}^r plane for a PMSG with Vienna rectifier.

which represents a ϕ-dependent ellipse on the I_{ds}^r–I_{qs}^r plane. Three equal-power-factor ellipses, corresponding to $\phi = \pm 30°$ and $\phi = 0°$, are plotted in Fig. 4.5.[4] The currents are constrained to lie within the region enclosed by the $\pm 30°$ curves.

An additional constraint is imposed from the maximum attainable line-to-neutral stator voltage, whose peak value depends on the power factor by [84]:

$$V_{s\max}(\phi) = \frac{V_o}{2\sqrt{3}\cos(60° - |\phi|)}, \tag{4.15}$$

where $\phi = \phi(I_{ds}^r, I_{qs}^r)$ by (4.13). In other words, combining (4.3), (4.4), (4.7), (4.13), and (4.15), the voltage limit equation is an implicit function of the qd-axes currents, parameterized by the rotor speed:

$$\left(V_{qs}^r(I_{ds}^r, I_{qs}^r; \omega_r)\right)^2 + \left(V_{ds}^r(I_{ds}^r, I_{qs}^r; \omega_r)\right)^2 \le \left(V_{s\max}(I_{ds}^r, I_{qs}^r)\right)^2 \tag{4.16}$$

Three voltage limit contours corresponding to $\omega_{r3} = 0.4$ p.u., $\omega_{r4} = 0.6$ p.u., and $\omega_{r5} = 0.8$ p.u. are numerically calculated and shown in Fig. 4.6. Due to the inclusion of stator resistance in the calculations, the curves become slightly unsymmetrical with respect to the $I_{qs}^r = 0$ axis. Also, they are not elliptical, and they tend to shrink with increasing ω_r.

The voltage limit curves corresponding to ω_{r4} and ω_{r5} are drawn in Fig. 4.5, together with the two corresponding equal-torque contours, $T_{e4} = T_e^*(\omega_{r4})$ and $T_{e5} = T_e^*(\omega_{r5})$. It can be

[4] It is interesting to note that all ellipses (regardless of the value of ϕ) intersect the $I_{qs}^r = 0$ axis at the origin and at $I_{ds}^r = \lambda_m / L_d$. The ellipses have been generated by setting $R_s = 0$. A nonzero resistance value will cause these ellipses to be speed-dependent, but their shape only changes slightly.

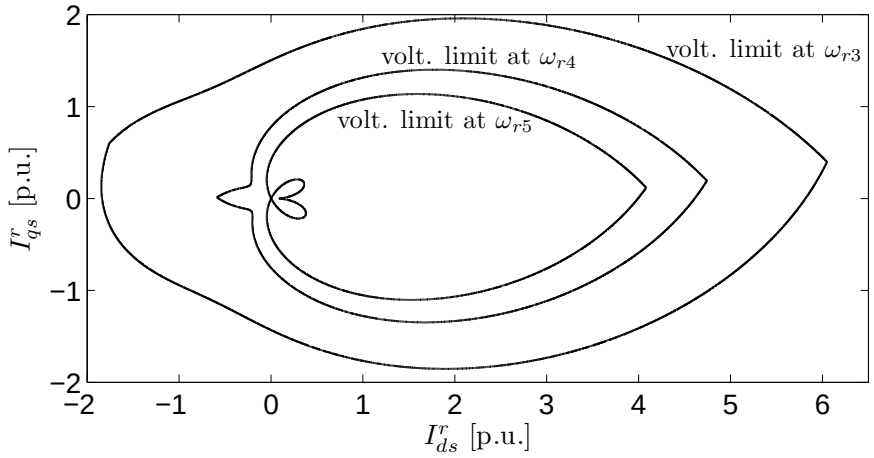

Figure 4.6 Voltage limit curves of PMSG with Vienna rectifier.

seen that for relatively low torque (i.e., low wind speeds), the available qd-axes currents are constrained by the power factor ellipses of $\phi = \pm 30°$; their limits are marked by Points J and K for T_{e4}. For higher torque levels, the constraints on the currents arise from the voltage limit curve or the current limit curve. For example, the currents of the T_{e5} contour are constrained by the voltage limit curve (Point L) and the current limit circle (Point M). Similar to the six-switch converter, Fig. 4.7 outlines the generator's current selection region (NOPQRS) for the entire wind speed range. This region is smaller than the one obtained for the six-switch converter. As will be explained in the next section, this more stringent operating limit does not negatively impact the wind turbine's capabilities. In fact, even with this limitation in place, the Vienna rectifier outperforms the conventional converter in terms of efficiency.

4.4 System Control Strategy

The next step after the determination of the feasible operating region is the design of a current control strategy to obtain the desired level of torque from the generator, constrained by the current, voltage, and power factor operating limits. In this section, a current control strategy that maximizes the system's energy conversion efficiency is proposed. To realize this, it is necessary to determine the qd-axes currents that lead to maximum efficiency at each operating point. The analysis takes into account copper losses in the stator windings and semiconductor losses in the converter. The losses are estimated using two different methods:

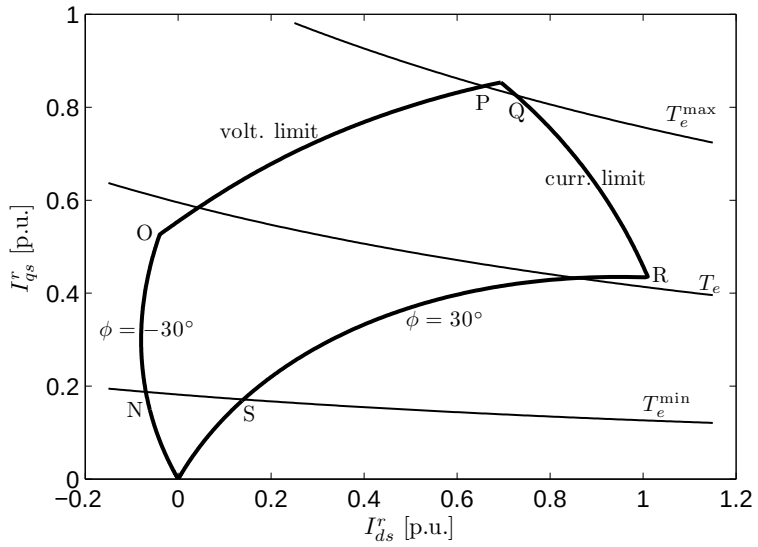

Figure 4.7 Current selection region for a PMSG with Vienna rectifier.

(i) assuming that the current waveform is purely sinusoidal, by calculating the conduction and switching losses of each semiconductor, and (ii) using a detailed switching-level simulation with a commercial simulation package. The former is relatively computationally inexpensive, and is used for scanning the entire feasible operating region, thus leading to the determination of optimal current commands for each wind speed. The latter is used to verify the results of the analytic calculation for the optimal points that have been previously determined.

4.4.1 Component Selection

Based on the voltage and current requirements of the 1.5-MW generator considered herein, the ABB 5SNA 1200G450300 single IGBT module [90] (rated for a collector-emitter voltage of 4500 V and a collector current of 1200 A) is selected for both the six-switch converter and the Vienna rectifier. (Note that the free-wheeling diode in the IGBT module never conducts current in the Vienna rectifier.) For the diodes of the Vienna rectifier, the ABB 5SDF 10H4502 fast-recovery diode module [91] (rated for a repetitive peak reverse voltage of 4500 V and a maximum RMS forward current of 1270 A) is selected for diodes D_k ($k = 1, ..., 6$), whereas the ABB 5SDD 11D2800 standard recovery diode module [92] (rated for a repetitive peak reverse voltage of 2800 V and a maximum RMS forward current of 1285 A) is selected for diodes D_{ai},

D_{bi}, and D_{ci} $(i = 1, ..., 4)$ [10]. For both converters, continuous space vector modulation is used, with a switching frequency of 2 kHz.

4.4.2 Identification of Most Efficient Operating Points

The power loss calculations for the six-switch converter and the Vienna rectifier are based on current- and voltage-dependent functions of the IGBTs' and diodes' on-state voltage drops and turn-on/off switching energy losses, which can be obtained from the components' data sheets [75, 93]. The currents are assumed to be purely sinusoidal. The objective is to search the entire operating region for the most efficient operating points. To achieve this, the wind speed range is discretized, and a finite set of feasible qd-axes currents that can provide the required torque for each wind speed is determined as per the current selection regions depicted in Figs. 4.4 and 4.7. For each qd-axes current pair, the calculations proceed as follows:

1. The generator's terminal voltages are calculated using (4.3) and (4.4).

2. The switching sequence and dwell time are obtained using the methods presented in [94] and [95, 96] for the six-switch converter and Vienna rectifier, respectively.

3. Each fundamental period ($T_f = 2\pi/\omega_r$) is discretized into a number of switching periods. The conduction and switching energy losses over each switching period are calculated by identifying the various topologies and switching events, and estimating the losses of each IGBT and diode. The losses are accumulated over the entire switching period.

4. The generator's ohmic losses are calculated.

5. The sum of converter and generator loss yields the total system loss.

Fig. 4.8(a) presents a three-dimensional plot of the calculated efficiency of the PMSG/six-switch converter system over the entire feasible operating region. The current set-points that lead to the highest efficiency for each operating point are marked by the black dots, which are projected on the current plane in Fig. 4.8(b). As can be seen, all points lie within a very narrow band around the maximum torque-per-ampere (MTPA) curve [53], which (for a PMSG

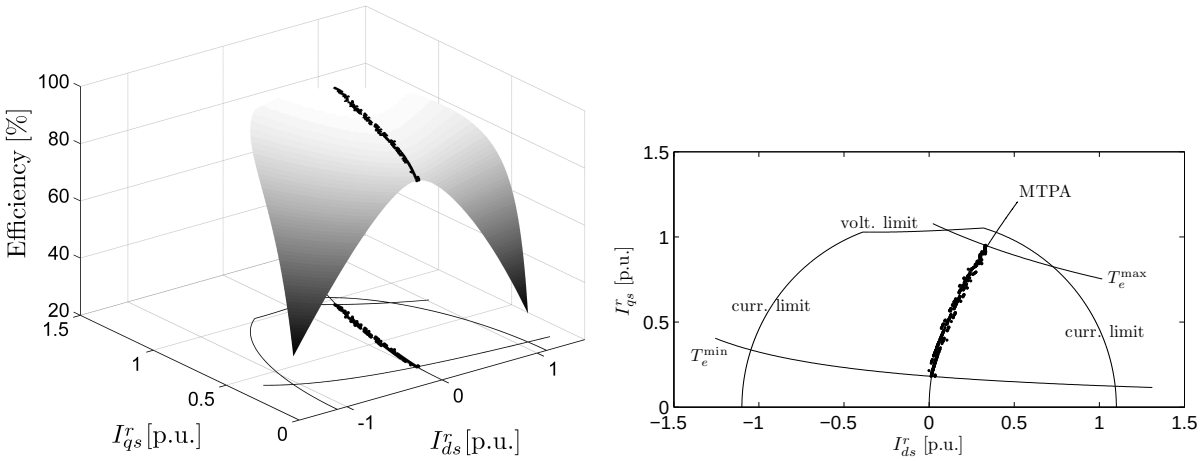

(a) Efficiency analysis.

(b) Optimal current operation points.

Figure 4.8 Efficiency and optimal current selection of the PMSG/six-switch converter system.

with saliency) can be expressed as:

$$\left(I^r_{qs}\right)^2 = \left(I^r_{ds}\right)^2 + I^r_{ds}\frac{\lambda_m}{L_q - L_d}\,. \tag{4.17}$$

The MTPA curve is derived based on a minimization of the stator's ohmic loss. Herein, the losses of the stator-side power electronics converter are also accounted for. It is interesting to note that the MTPA curve results in the optimal efficiency of the combined generator/converter system.

Similarly, Fig. 4.9(a) depicts the efficiency of the PMSG/Vienna rectifier system. Fig. 4.9(b) shows that, for relatively low and medium torque, the optimal current set-points lie very close to the MTPA curve. However, at higher torque levels, the MTPA curve extends outside the feasible current selection region, so the optimal current set-points are located on the voltage limit curve. Therefore, a control system designer can make use of the classical MTPA and voltage limit curves, which are both analytically tractable, to generate the current command look-up table.

The switching loss, $P_{\rm sw}$, conduction loss, $P_{\rm c}$, and total semiconductor loss, $P_{\rm semi} = P_{\rm sw} + P_{\rm c}$, of the six-switch converter and the Vienna rectifier over the entire wind speed range are juxtaposed in the top three graphs of Fig. 4.10. For the Vienna rectifier, these include the losses of the IGBTs and the diodes. For the six-switch converter, these represent the losses of

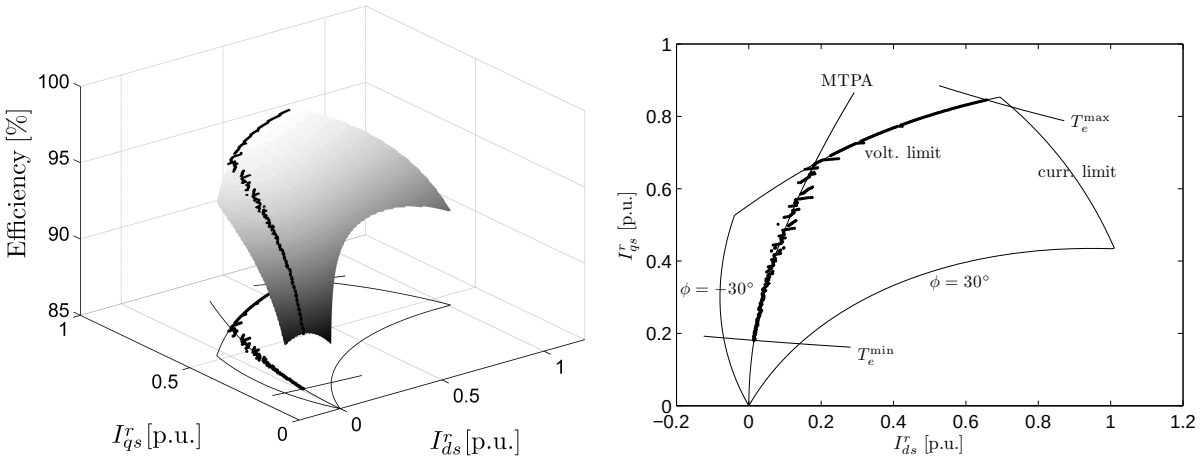

(a) Efficiency analysis.

(b) Optimal current operation points.

Figure 4.9 Efficiency and optimal current selection of the PMSG/Vienna rectifier system.

the IGBTs and their free-wheeling diodes. (For wind speeds higher than rated, the operating point of the generator is assumed to remain constant.) Since the blocking voltage stress of the Vienna rectifier IGBTs and diodes is only half of the voltage stress in the six-switch converter, the Vienna rectifier exhibits lower switching loss. On the other hand, due to the larger number of diodes in the Vienna rectifier, its conduction loss is higher. The bottom graph shows the combined generator/converter power loss, P_{loss}. Overall, the Vienna rectifier leads to lower power losses over the entire speed range. Remarkably, even though the Vienna rectifier deviates from the optimal MTPA curve after a certain wind speed (ca. 8 m/s in this example), the total power loss is always lower than the conventional six-switch converter system, as demonstrated in Fig. 4.11. The third graph of Fig. 4.10 also includes the total (switching plus conduction) IGBT losses for the Vienna rectifier, marked by crosses. The apparent decrease of IGBT loss in the Vienna rectifier can reduce the thermal stress of the IGBTs, and thus further improve the reliability of the IGBT modules [64, 65].

The expected annual energy loss of the PMSG/Vienna system can be estimated by taking into account the statistics of wind speed. Usually, the Weibull probability density function is used to describe the variation of wind speed over a year [76]. The Weibull distribution is defined using a scale parameter c, and a shape parameter k. Here, $k = 2$ and $c = 8.3$ m/s. As

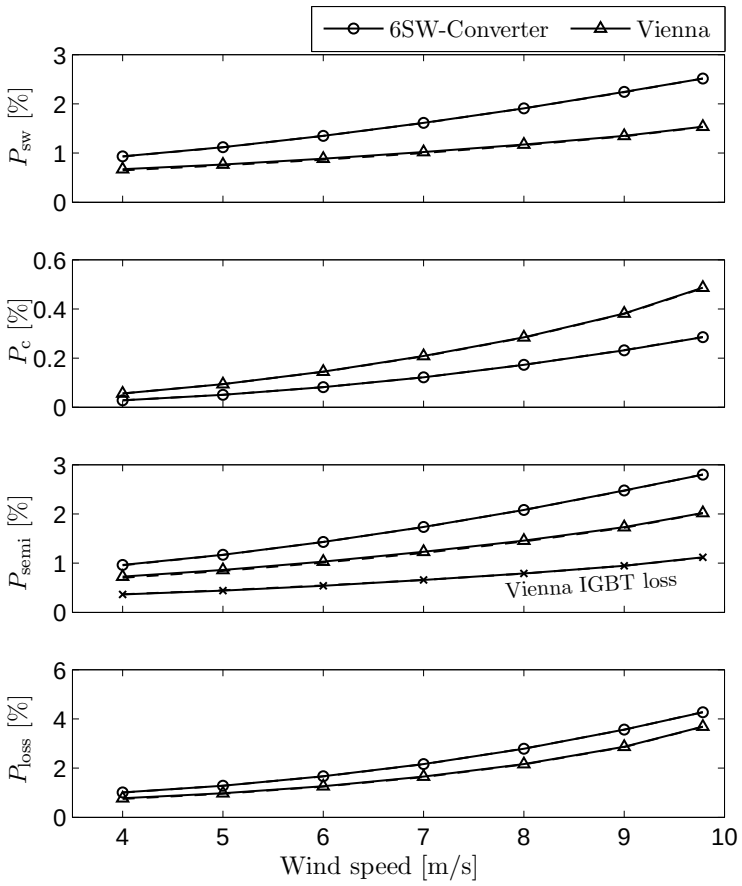

Figure 4.10 Loss comparison between six-switch converter and Vienna rectifier (losses expressed in per unit, with respect to the rated generator power).

described previously, the total power loss can be computed as a function of the wind speed, $P_{\text{loss}}(v_w)$. Then the expected annual energy loss, E_{loss}, can be found by applying the formula for the expected value of an arbitrary function $g(X)$ of a random variable X with respect to a probability density function $f(x)$, $E(g(X)) = \int_{-\infty}^{\infty} g(x)f(x)dx$:

$$\begin{aligned} E_{\text{loss}} &= 8760 \cdot E(P_{\text{loss}}(v_w)) \\ &= 8760 \int_{v_w^{\text{in}}}^{v_w^{\text{out}}} P_{\text{loss}}(v_w) f(v_w) dv_w \,, \end{aligned} \tag{4.18}$$

where v_w^{in} and v_w^{out} are the cut-in and cut-out wind speeds, and $f(v_w)$ is the Weibull probability density function at hub height. The integral in (4.18) can be evaluated numerically, using the trapezoidal rule and the discrete points that were obtained previously. Ideal blade pitching is

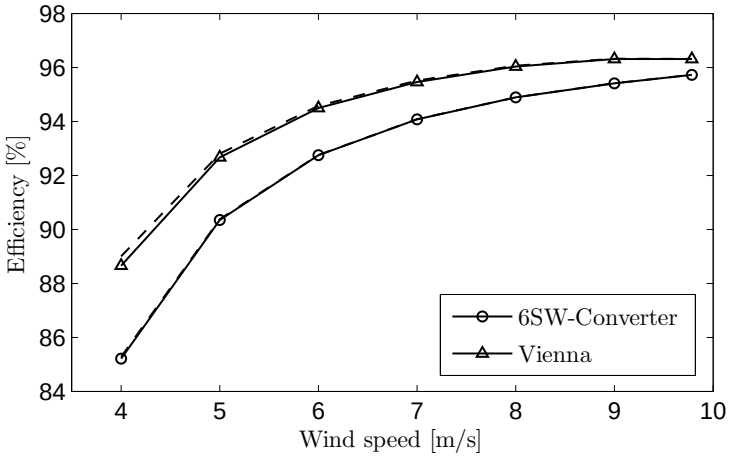

Figure 4.11 Efficiency comparison between six-switch converter and Vienna rectifier.

Table 4.1 Energy Loss Comparison

Loss	Fundamental-only		Simulation	
	MWh	%	MWh	%
6-SW converter	299.16	4.907	299.11	4.906
Vienna rectifier	245.89	4.033	244.44	4.009

assumed to occur above the rated wind speed. The annual energy losses of the two configurations are listed in Table 4.1, in absolute numbers and as a percentage of the total expected annual mechanical input energy, calculated as follows:

$$E_m = 8760 \int_{v_w^{\text{in}}}^{v_w^{\text{out}}} P_m(v_w) f(v_w) dv_w \,. \tag{4.19}$$

For v_w lower than the rated wind speed, equation (4.1) with the optimal value of the tip-speed ratio λ_o and $\gamma = 0$ is used. For v_w higher than the rated speed, constant rated power is used.

4.4.3 Simulation-Based Power Loss Estimation

In order to verify the results obtained using the fundamental component-based power loss calculation method, detailed time-domain simulations of both systems have been performed using Matlab/Simulink and the Piecewise Linear Electrical Circuit Simulation (PLECS) toolbox [59]. PLECS supports the thermal modeling and simulation of semiconductors. The switching and conduction losses can be obtained if the thermal description parameters of switches and diodes are specified in the PLECS circuits [59].

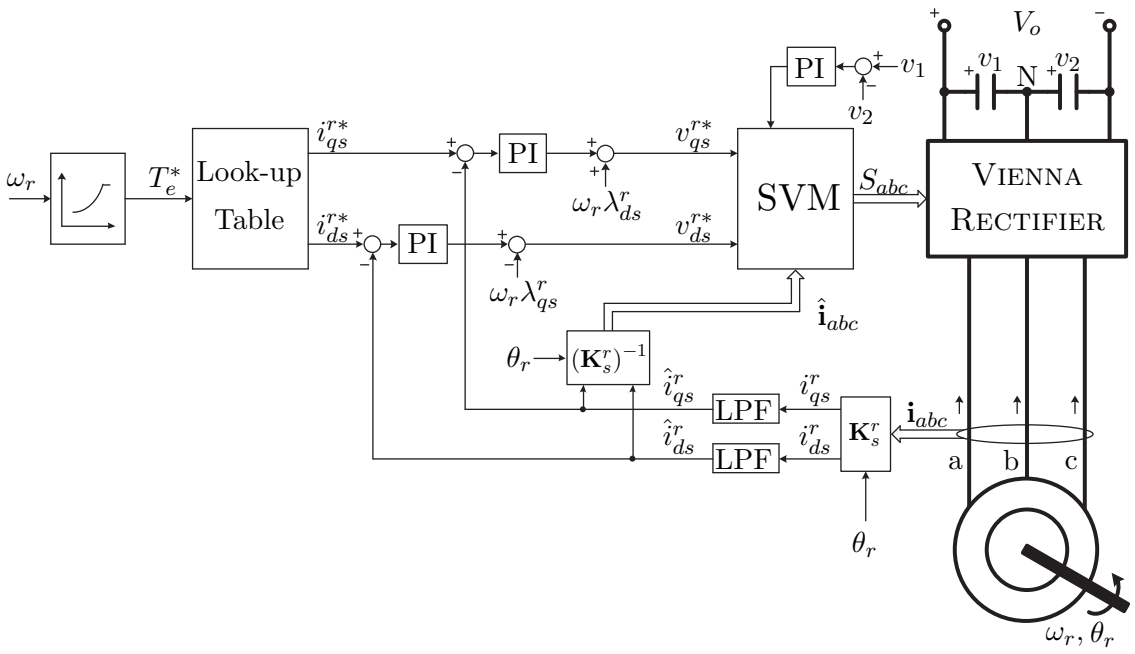

Figure 4.12 Control block diagram for the PMSG driven by the Vienna rectifier. (The reference frame transformation matrix $\mathbf{K}_s^r$ is defined in [53].)

The control structure for the PMSG/Vienna rectifier is illustrated in Fig. 6.1. The torque command T_e^* is determined from the measured generator speed based on a predefined quadratic function for maximum power extraction, viz. (4.2). Note that when the wind speed is higher than its rated value, blade pitching control is activated, and the torque command is set at its maximum value. Usually a 10% increase of the generator speed can occur due to the slow pitch angle control dynamics [77]. The qd-axes current commands (i_{qs}^{r*} and i_{ds}^{r*}) are pre-calculated using the method described in Section 4.4.2, and generated with a look-up table. For the Vienna rectifier, the simplified space vector modulation method based on the equivalence between two-level and three-level converters is applied [96]. Specifically, the 3-phase currents ($\hat{\mathbf{i}}_{abc}$) are used to identify the active voltage vectors in the space vector diagram. Then, the switching sequence selection and dwell time calculation are performed using the method presented in [95].

Two low-pass filters (LPF) are used to prevent noise from affecting the control and the determination of active voltage vectors. The balancing of the dc-link neutral-point voltage is achieved by adjusting the time distribution of the redundant voltage vectors within one

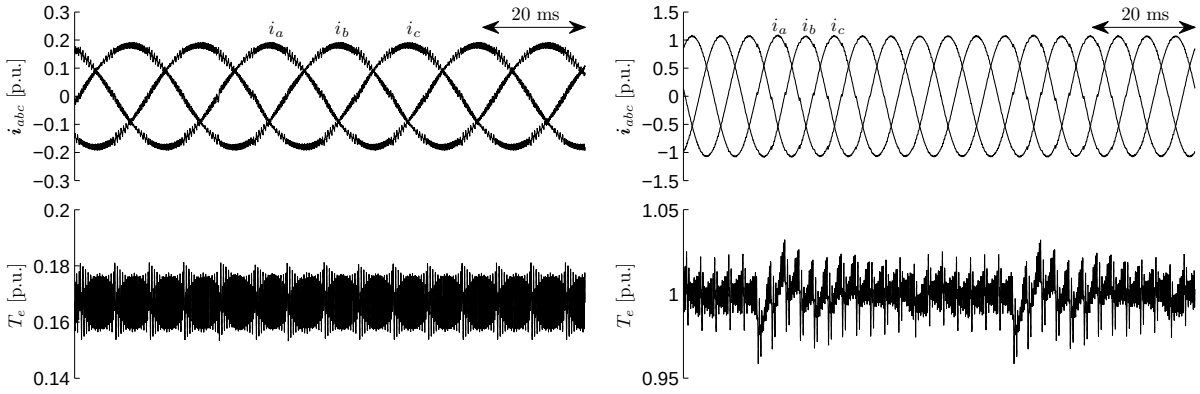

(a) Cut-in wind speed (4 m/s).

(b) Rated wind speed (9.8 m/s).

Figure 4.13 Simulated time-domain waveforms of PMSG stator currents and torque.

single switching period [95, 97]. The dc-link voltage V_o is controlled by a grid-side converter, which is not shown in Fig. 6.1. For the simulations, V_o is assumed to remain constant. Two representative simulation results depicting the generator's currents and electromagnetic torque for the cut-in and rated wind speeds are provided in Fig. 4.13. There appears to be a periodicity of 60 electrical degrees in the torque waveform, in the form of minor spikes. This is due to the phase currents crossing zero, which occurs every 60 electrical degrees. If this happens in the middle of a switching cycle (which is probably unavoidable), a discontinuity in the generated voltage occurs, because in the Vienna rectifier the voltage depends on the sign of the current. This effect can be observed as notches that appear in the current waveforms as they cross zero. This in turn affects the electromagnetic torque. Further work is necessary to better understand and mitigate this phenomenon.

The simulation-based loss calculations are superimposed as points connected by dashed lines on Figs. 4.10 and 4.11 and the annual energy loss is added to Table 4.1. The results are almost identical to the ones obtained from the fundamental-only method. Apparently, the PMSG/Vienna rectifier topology is a more efficient system, leading to a 0.9% increase in annual energy yield. In addition, since the Vienna rectifier generates three voltage levels, the current through the PMSG has lower harmonic content than in the conventional system, which is demonstrated by the total harmonic distortion (THD) comparison in Table 4.2.

Table 4.2 PMSG Current THD Comparison

THD (%)	Wind Speed (m/s)						
	4	5	6	7	8	9	9.8
6-SW converter	5.81	4.84	4.04	3.58	3.44	3.02	2.98
Vienna rectifier	5.41	4.16	3.20	2.77	3.04	2.91	2.79

4.5 Experimental Results

To verify the feasibility of the PMSG/Vienna rectifier configuration, a small-scale laboratory prototype has been implemented, with parameters provided in Appendix C.2. The generator was driven at various constant speed values by an identical servo motor. The dc-link voltage was regulated by a programmable dc power source (Sorensen SGI330X45C), set at $V_o = 50$ V. An electronic load (Chroma 63840) was connected in parallel with the dc-link capacitors to absorb the generated power. The control scheme shown in Fig. 6.1 was implemented on a dSPACE DS1103 system, with a switching frequency of 4 kHz. The controller was programmed to generate a quadratic torque-speed characteristic (see equation (4.2)), so that rated shaft power (200 W) is obtained at the rated speed.

Fig. 4.14 depicts the feasible operation region for the laboratory prototype. The drive operates along the MTPA curve for low speeds, then becomes voltage-limited for higher speeds. The asterisks denote operating conditions that were measured in the laboratory. Fig. 4.15 shows the variation of real power, reactive power, and power factor angle at the generator terminals for the above points. The solid lines represent expected theoretical results, whereas the asterisks are experimental measurements. These measurements reflect fundamental quantities, acquired using a Voltech PM6000 power analyzer. The corner point at approximately 0.73 pu speed is due to the change from the MTPA to the voltage-limited mode of operation.

Fig. 4.16 contains experimental waveforms for two steady-state operating points (corresponding to the lowest and highest speed). The plots depict line-to-line voltage v_{ab} and armature current i_a, captured with a Tektronix DPO4034B oscilloscope. At low speeds, the line-to-line voltage obtains 3 distinct values ($\{0, \pm 25\}$ V), whereas at higher speeds the voltage obtains 5 distinct values ($\{0, \pm 25, \pm 50\}$ V), as expected. Because of the relatively low dc-link

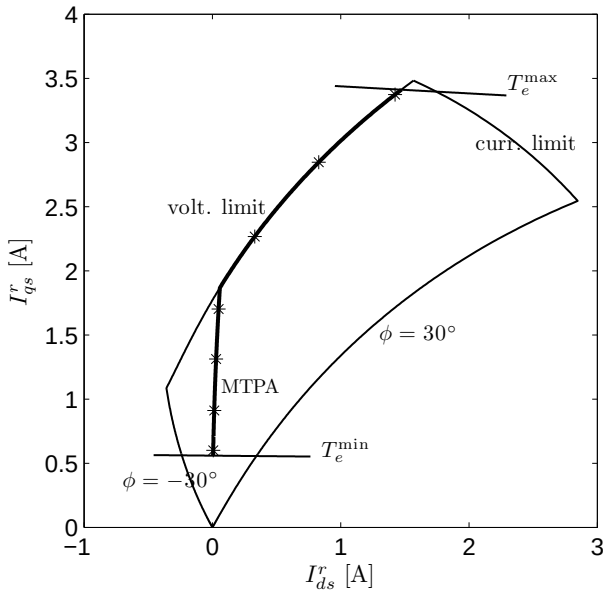

Figure 4.14 Optimal current operation points for the laboratory prototype.

voltage in the prototype, forward voltage drops in the diodes and IGBTs of the Vienna rectifier are apparent in the voltage waveforms. Nevertheless, the current waveforms are close to the simulation results, which are shown in gray.

Fig. 4.17 shows the transient response of the generator under an increase of rotor speed ω_r from 0.415 p.u. up to 0.994 p.u. The amplitude of the generator current is gradually increased. The two capacitor voltages v_1 and v_2 are maintained close to their nominal value by means of the dc-link neutral-point voltage balance control.

4.6 Conclusions

A variable-speed wind energy conversion system based on a permanent-magnet synchronous generator with Vienna rectifier has been studied. A rigorous mathematical analysis has been performed, and the restrictions on the system's operating range imposed by the current, voltage, and power factor limitations of the Vienna rectifier have been identified. Even with these in place, the system can function without problem throughout the entire wind speed range. Detailed power loss calculations in the power electronics converter and the generator itself are used to design a control strategy that leads to maximum energy efficiency. Interestingly, the

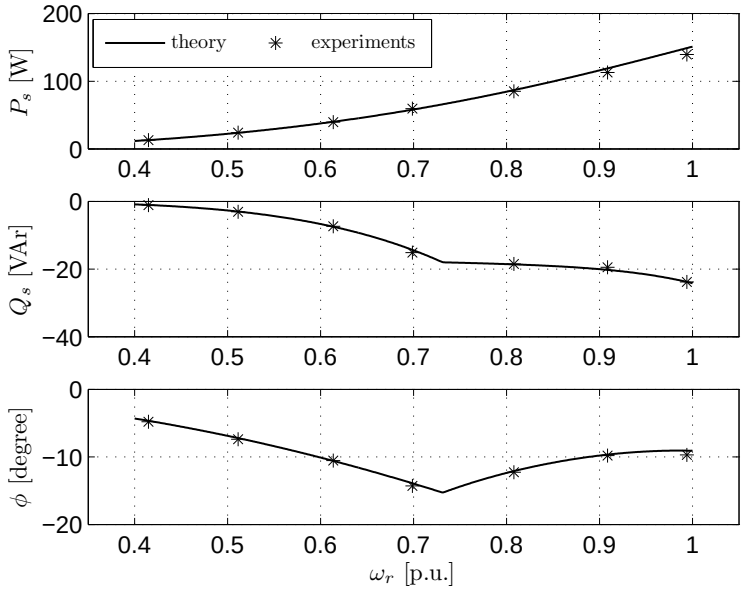

Figure 4.15 Variation of active power, reactive power, and power factor angle at the generator terminals (fundamental quantities).

proposed configuration is shown to outperform the classical six-switch two-level converter.

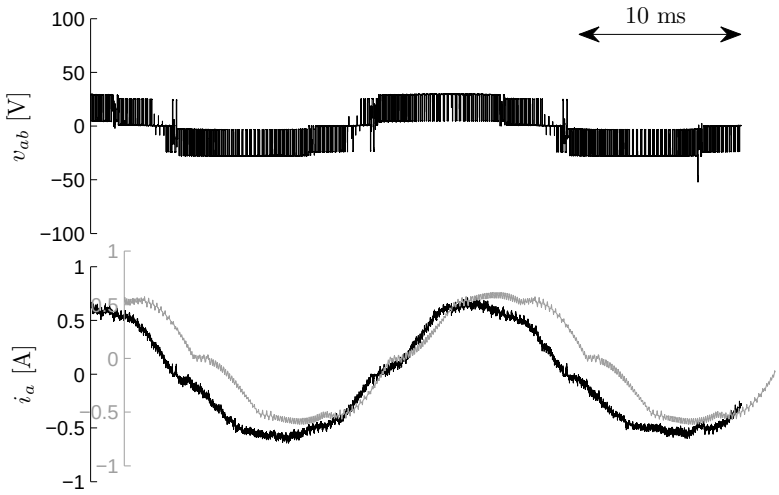

(a) Low generator speed ($\omega_r = 0.415$ p.u.).

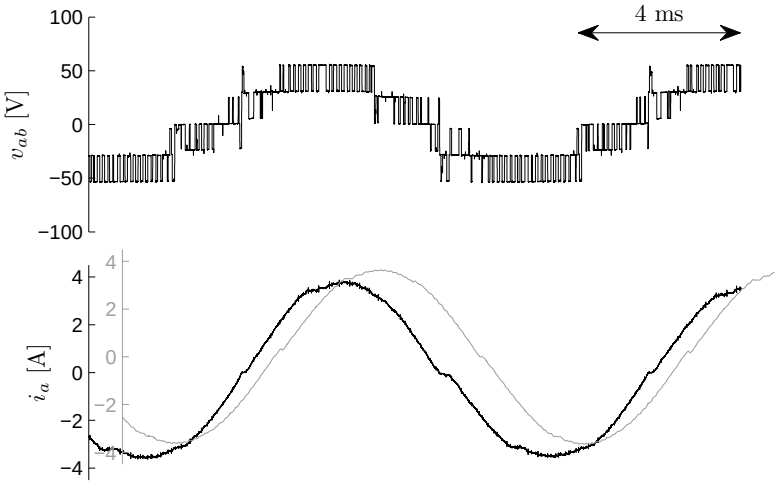

(b) High generator speed ($\omega_r = 0.994$ p.u.).

Figure 4.16 Experimental time-domain waveforms of PMSG stator voltage and current.

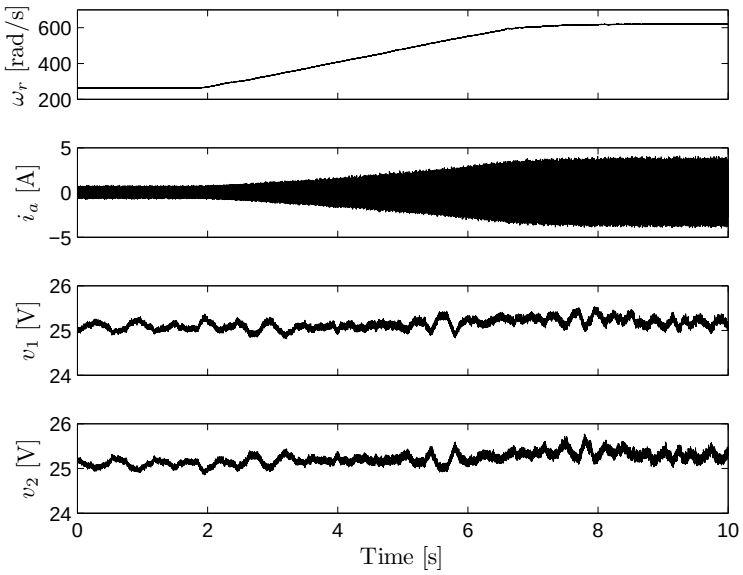

Figure 4.17 Acceleration study.

CHAPTER 5. LOW-FREQUENCY AC TRANSMISSION FOR OFFSHORE WIND POWER

A paper to be submitted to the *IEEE Transactions on Power Delivery*

Hao Chen[1] and Dionysios C. Aliprantis

5.1 Abstract

This paper presents a low-frequency ac (LFAC) transmission system for offshore wind power. The LFAC system is interfaced with the main power grid with a cycloconverter. The wind power plant collection system is dc-based, and connects to the LFAC transmission line with a 12-pulse thyristor converter. A method to design the system's components and controls is set forth. Simulation results are provided to illustrate the system's performance.

5.2 Introduction

Offshore wind power plants are expected to represent a significant component of the future electric generation portfolio due to space availability and better wind energy potential in offshore locations [2, 16]. The integration of offshore wind power plants with the main power grid is still a subject of active research [15, 29, 98]. For transmission, high voltage ac (HVAC) is typically used for short distances, whereas high-voltage dc (HVDC) is preferred for longer distances [13]. Within a wind power plant, a medium-voltage ac collection grid (e.g., 33 kV) is widely used [6]. Recently, with the development of cost-effective dc circuit breakers, a medium-voltage dc collection grid has become a feasible alternative [20], suitable for direct coupling with HVDC transmission. A medium/high-level dc voltage can be built by either

[1]Primary researcher and author

using high-power dc-dc converters [99] or by a series connection of wind turbines within the power plant [100].

Besides HVAC and HVDC, low-frequency ac (LFAC) transmission has been recently proposed [22, 24, 25], where an intermediate frequency level (e.g., 20 Hz) is used. LFAC systems are based on a cycloconverter that lowers the grid frequency to a smaller value, typically 1/3 of the normal grid frequency. In general, LFAC systems are expected to have higher reliability and lower cost compared to voltage source converter-based HVDC [13, 14], but perhaps their greatest advantage is that they can transmit power over longer distances compared to an HVAC system. The LFAC transmission could be an optimal solution for medium distance transmission (i.e., somewhere in between HVAC and HVDC) [25].

In this paper, a novel LFAC transmission topology using thyristor-based converters is analyzed. The main difference of the proposed topology with previous work [24, 25] is that a dc wind power plant collection system is used. Hence, the wind turbines would not need to be redesigned to output low-frequency ac power, which would lead to larger, heavier, and costlier magnetic components (i.e., step-up transformers and/or generators). In particular, dc collection systems can be formed by interconnecting multi-MW permanent-magnet synchronous generators with fully rated converters, which tend to be the generator type of choice for offshore applications. Another advantage of the proposed scheme is its feasibility for multi-terminal transmission systems, instead of multi-terminal HVDC [101, 102], but the analysis of such an application is out of the scope of the present study.

The objective of this paper is to set forth the details of how an LFAC system for point-to-point transmission could be designed. The system configuration and control strategies are outlined in Section 5.3. The selection of the major system components is discussed in Section 5.4.1, and filter design is discussed in Section 5.4.2. A design example and time-domain simulation study of the proposed LFAC system are provided in Section 5.5 and Section 5.6, respectively. Section 5.7 concludes the paper.

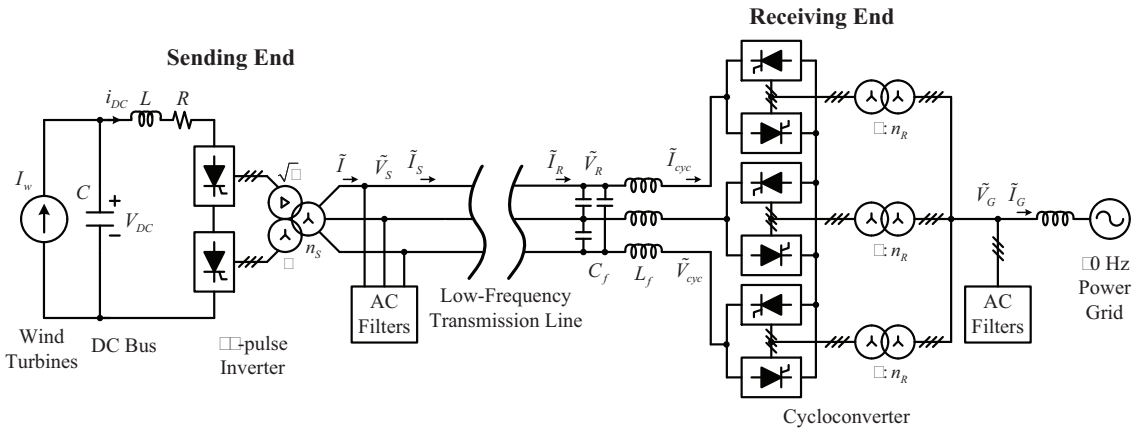

Figure 5.1 Configuration of the proposed LFAC transmission system.

5.3 System Configuration and Control

The proposed LFAC transmission system is shown in Fig. 5.1. At the sending end, a medium-voltage dc collection bus is formed by rectifying the ac output power of series-connected wind turbines [52]. A dc current source I_w represents the total power delivered from the wind turbines. A dc/ac 12-pulse thyristor-based inverter is used to generate low-frequency (20 Hz) ac power. It is connected to a three-winding transformer that raises the voltage to a higher level, for transmission. AC filters are used to suppress the 11th, 13th, and higher-order ($\geq$23rd) current harmonics, and to supply reactive power to the converter. A smoothing reactor (R-L) is connected at the inverter's dc terminals. At the receiving end, a three-phase bridge (6-pulse) cycloconverter with 36 thyristors is used as an interface between the low-frequency transmission line and the 60-Hz power grid. L_f-C_f is the cycloconverter's filter at the low-frequency side. At the grid side, AC filters are used to suppress odd current harmonics, and to supply reactive power to the cycloconverter.

5.3.1 Sending End Control

The control structure for the sending-end inverter is shown in Fig. 5.2. The controller regulates the dc bus voltage V_{DC} by adjusting the voltage V at the inverter terminals. The

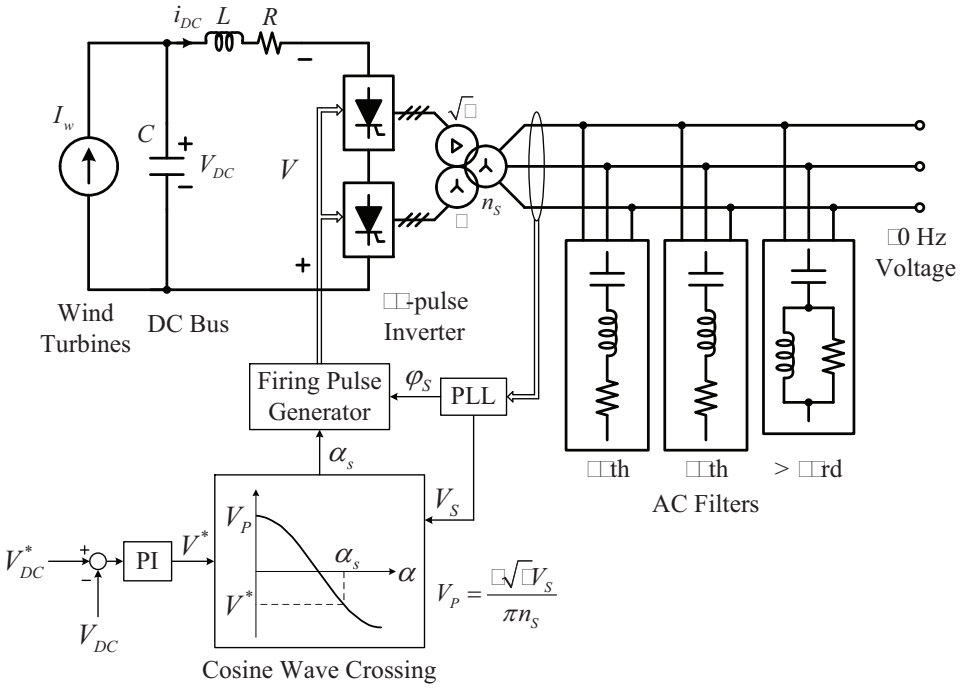

Figure 5.2 Sending end DC/AC inverter control.

cosine wave crossing method [26] is applied to determine the firing angle α_S, which is

$$\alpha_S = \arccos \frac{V^*}{V_P}, \tag{5.1}$$

where V_P is the peak value of the cosine wave. Note that $V^* < 0$ and $90^\circ < \alpha_S < 180^\circ$ (using common notation), since the converter is in the inverter mode of operation [103]. V and V_S (line-to-neutral, rms) are related by [97]:

$$V = \frac{6\sqrt{6}V_S}{\pi n_S} \cos \alpha_S \,. \tag{5.2}$$

A phase-locked loop (PLL) provides the angular position of the ac side voltage, which is necessary for generating the firing pulses of the thyristors. It also outputs the rms value of the fundamental component of the voltage, which is used in the firing angle calculation.

5.3.2 Receiving-End Control

The structure of the cycloconverter controller at the receiving end is illustrated in Fig. 5.3. The goal is to provide a constant 20-Hz voltage of given rms value V_R^* (line-to-neutral) at the

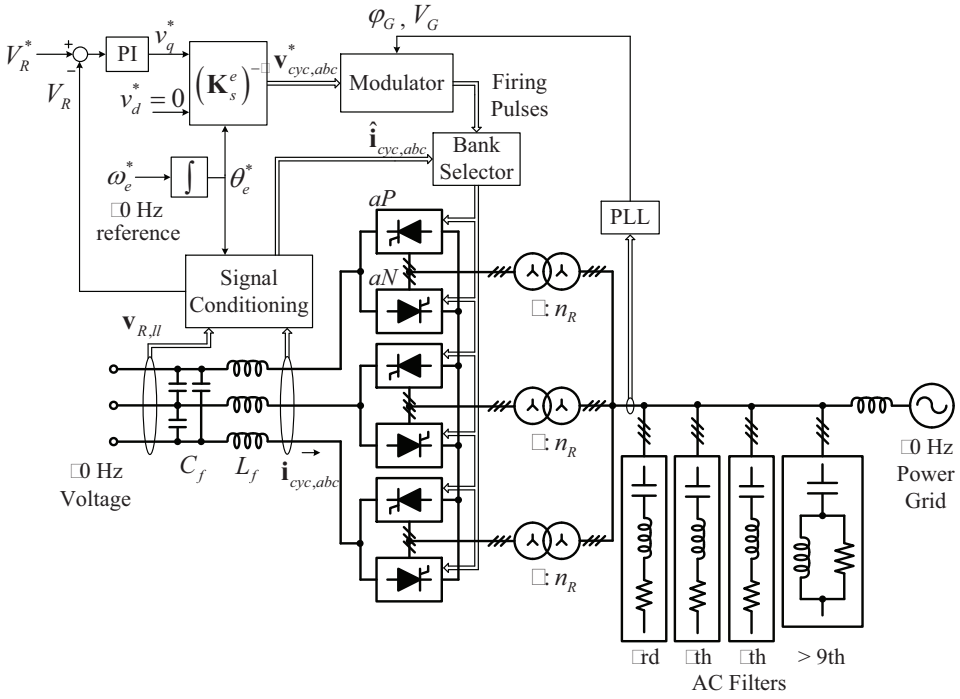

Figure 5.3 Receiving end cycloconverter control. (The reference frame transformation matrix $\mathbf{K}_s^e$ is defined in [53], and transforms variables from the stationary to the synchronous reference frame.)

receiving end. The fundamental component of the receiving end voltage V_R is obtained with the signal conditioning logic depicted in Fig. 5.4.

The firing angles are determined with the cosine wave crossing method, as shown in Fig. 5.5, which uses phase-a as an example. α_{aP} and α_{aN} are the firing angles of the phase-a positive and negative converter, respectively (denoted as 'aP' and 'aN' in Fig. 5.3). For the positive converter, the average voltage at the 20-Hz terminals is given by [97]:

$$V_{aP} = \frac{3\sqrt{6}V_G}{\pi n_R}\cos\alpha_{aP}\,, \tag{5.3}$$

where V_G is the rms value of the line-to-neutral voltage at the grid side, and n_R is the turns ratio of the transformers. The condition $\alpha_{aP}+\alpha_{aN}=\pi$ ensures that average voltages with the same polarity are generated from the positive and negative converter at the 20-Hz terminals [104]. However, the firing pulses S_{aP} and S_{aN} are not simultaneously applied to both converters, in order to obtain a non-circulating current mode of operation. This functionality is embedded in the 'Bank Selector' block of Fig. 5.3, which operates based on the filtered current $\hat{\mathbf{i}}_{cyc,abc}$.

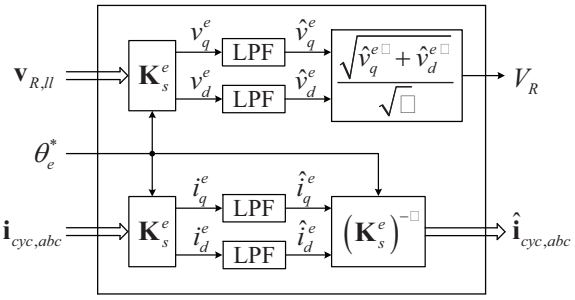

Figure 5.4 Details of the signal conditioning block. (LPF = low-pass filter; the time constants are 0.05 s and 0.01 s for the voltage and current respectively.)

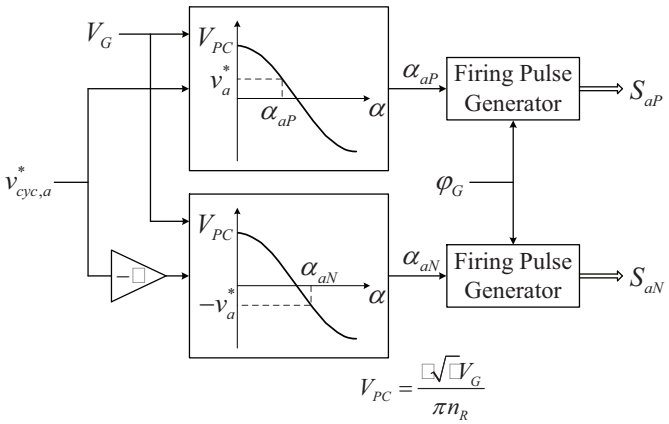

Figure 5.5 Modulator for phase *a*.

Note (for later use) that the maximum line-to-neutral rms value of the 20-Hz cycloconverter voltage is [26]

$$V_{cyc}^{\max} = \frac{3\sqrt{3}V_G}{\pi n_R}, \tag{5.4}$$

and that a voltage ratio is defined as

$$r = \frac{V_{cyc}}{V_{cyc}^{\max}}. \tag{5.5}$$

In practice, the theoretical maximum value $r = 1$ cannot be achieved, due to the transformers' leakage inductance, which was ignored in the analysis.

5.4 System Design

5.4.1 Main Power Components

The main power components are selected based on a steady-state analysis of the LFAC transmission system shown in Fig. 5.1, under the following assumptions:

- Only fundamental components of voltages and currents are considered. The receiving end is modeled as a 20-Hz voltage source of nominal magnitude.
- The power losses of the reactor, thyristors, filters, and transformers are ignored.
- The resistances and leakage inductances of transformers are neglected.
- The AC filters are represented by an equivalent capacitance corresponding to the fundamental frequency.
- The design is based on rated operating conditions (i.e., maximum power output).

At the steady state, the average value of the dc current I_{DC} is equal to I_w, so the power delivered from the wind turbines is

$$P_w = V_{DC} I_{DC} = V_{DC} I_w \,. \tag{5.6}$$

For the 12-pulse converter, the rms value of the current at the transmission side is [97]:

$$I = \frac{2\sqrt{6}}{\pi} \frac{I_{DC}}{n_S} = \frac{2\sqrt{6}}{\pi} \frac{I_w}{n_S} \,. \tag{5.7}$$

Hence, (5.7) can be written as

$$I = M P_w \,, \tag{5.8}$$

with

$$M = \frac{2\sqrt{6}}{\pi n_S V_{DC}} \,. \tag{5.9}$$

Let $\tilde{V}_S = V_S \angle 0^\circ$ and $\tilde{I}$ denote phasors of the line-to-neutral voltage and line current, respectively. Since $-\tilde{I}$ lags $\tilde{V}_S$ by α_S [97], it follows that $\tilde{I} = I \angle (180^\circ - \alpha_S)$. So, the active power delivered by the 12-pulse inverter is given by

$$P_S = P_w = 3 V_S I \cos(\alpha_S - 180^\circ) = -3 V_S I \cos \alpha_S > 0 \,. \tag{5.10}$$

Substitution of (5.8) into (5.10) yields

$$\cos\alpha_S = -\frac{1}{3MV_S} \tag{5.11}$$

and

$$\sin\alpha_S = \sqrt{1-\frac{1}{9M^2V_S^2}}\,. \tag{5.12}$$

The reactive power generated from the 12-pulse inverter is

$$Q_S = 3V_S I\sin(\alpha_S - 180^\circ) = -3V_S I\sin\alpha_S\,. \tag{5.13}$$

From (5.10)–(5.13), it follows that

$$Q_S = P_S\tan\alpha_S = -P_S\sqrt{9M^2V_S^2-1}\,. \tag{5.14}$$

The negative sign in (5.13) and (5.14) indicates that the 12-pulse inverter always absorbs reactive power. Equation (5.14) shows that Q_S can be expressed as a function $Q_S = f(P_S, V_S)$.

Based on the above analysis, the steady-state single-phase equivalent circuit of the LFAC transmission system is shown in Fig. 5.6. C_{eq} is the equivalent capacitance of the sending-end AC filters at fundamental frequency. The transmission line is modeled by a Π-equivalent (positive-sequence) circuit using lumped parameters. The well-known hyperbolic trigonometric expressions for Z' and $\frac{Y'}{2}$ are used [105]. Given a power rating of a wind power plant P_{rated}, the maximum reactive power that is absorbed by the 12-pulse inverter can be estimated according to (5.14), which yields

$$Q_{\text{rated}} = P_{\text{rated}}\sqrt{3M^2V_o^2-1}\,, \tag{5.15}$$

where V_o is the nominal transmission voltage level (line-to-line rms).

Here, it is assumed that the sending-end AC filters supply the rated reactive power to the inverter. Therefore,

$$C_{eq} = \frac{Q_{\text{rated}}}{\omega_e V_o^2}\,, \tag{5.16}$$

where $\omega_e = 2\pi 20$ rad/s. In addition, the apparent power rating of the transformer at the sending end S_{tS} should satisfy

$$S_{tS} > \sqrt{P_{\text{rated}}^2 + Q_{\text{rated}}^2} = \sqrt{3}P_{\text{rated}}MV_o\,. \tag{5.17}$$

At the 60-Hz grid side, the reactive power capacity of the AC filters and the apparent power rating of the transformers depend on the cycloconverter's voltage ratio r, which is a design parameter, and the 20-Hz side power factor [104], which can be estimated as follows.

For a given transmission cable, the voltage ratings (nominal and maximum voltage), the current rating, and the distributed cable parameters (resistance, inductance, and capacitance per unit length) are known. Here, it is assumed that a power cable is chosen to transmit the rated wind power plant power P_{rated} without violating the cable's voltage and current ratings. (The relationship between active power through the cable and maximum transmission distance, given a certain cable, will be discussed later.) For simplicity, it is further assumed that the rms value of line-to-line voltage at both sending and receiving ends is V_o and the current through Z' and L_f is approximately equal to the current rating of the cable I_{rated}.

Since the AC filters are designed to supply all reactive power to the 12-pulse inverter at the sending end, the reactive power injected into the cycloconverter's 20-Hz side can be estimated using

$$Q_{cyc}^{20} \approx \text{Im}\{Y'\}V_o^2 + \omega_e 3C_f V_o^2 - 3I_{\text{rated}}^2 \text{Im}\{Z'\} - 3I_{\text{rated}}^2 \omega_e L_f \,, \tag{5.18}$$

where the first two terms represent the reactive power generated from the cable and the LC filter's capacitor, and the last two terms represent the reactive power consumed by the cable and the LC filter's inductor. The active power injected into the cycloconverter from the 20-Hz side can be estimated using

$$P_{cyc}^{20} \approx P_{\text{rated}} - \text{Re}\{Y'\}V_o^2 - 3I_{\text{rated}}^2 \text{Re}\{Z'\} \,, \tag{5.19}$$

where the last two terms represent the power loss of the cable. Thus, the 20-Hz side power factor can be estimated according to (5.18) and (5.19).

Now the 60-Hz side power factor PF^{60} at the transformers' grid-side terminals can be obtained using the method presented in [104, Ch. 12, p. 358]. Then the apparent power rating of each out of the three receiving-end transformers S_{tR} should satisfy

$$S_{tR} > \frac{P_{cyc}^{20}}{(3)(\text{PF}^{60})} \,. \tag{5.20}$$

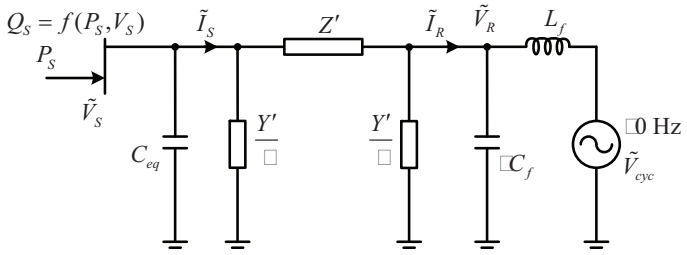

Figure 5.6 Equivalent circuit of 20-Hz transmission system.

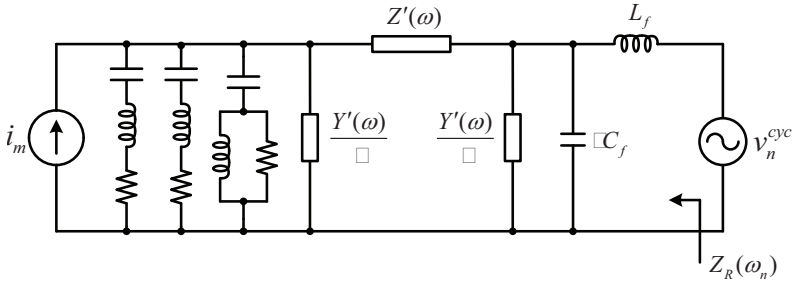

Figure 5.7 Equivalent circuit of 20-Hz transmission system for harmonic analysis.

Also, it is assumed that the grid-side AC filters are designed to supply the rated amount of reactive power to the cycloconverter.

5.4.2 Filter Design

At the sending end, the 12-pulse inverter produces harmonics of order $m = 12k \pm 1$, $k = 1, 2, \cdots$, and can be represented as a source of harmonic currents (i_m in Fig. 5.7). These current harmonics are filtered by two single-tuned filters for the 11th and 13th harmonics, and one damped filter for higher-order harmonics (≥23rd). Generally, the filter design is dependent on the reactive power that the filter supplies at fundamental frequency (also known as the filter size) and the required quality factor Q [106]. The total reactive power requirement of these filters can be estimated based on (5.15). Here, it is assumed that the total reactive power requirement is divided equally among the three filters. The quality factor for each filter can be determined using the method presented in [106, Ch. 6]. A high quality factor ($Q = 100$) is used for the single-tuned filters, and a low quality factor ($Q = 1$) is used for the high-pass damped filter. Finally, with the capacitance and quality factor known, the inductance and resistance of

each filter can be determined. With such filter design, the 12-pulse-related current harmonics originating at the sending end are essentially absent from the transmission line.

At the receiving end, there are two groups of filters which include the AC filters at the 60-Hz side and the LC filter at the 20-Hz side. At the 60-Hz side, if the cycloconverter generates exactly $60/3 = 20$ Hz, it can be shown [104, Ch. 12, pp. 360–363] that the line current has only odd harmonic components, i.e., 3rd, 5th, 7th,$\cdots$. Here, three single-tuned filters and one damped filter are used to prevent these harmonic currents from being injected into the 60-Hz power grid. These filters are designed with a procedure similar to that for the AC filters at the sending end.

At the 20-Hz side, the line-to-neutral voltage has harmonics of order $3, 5, 7, \cdots$ [104, Ch. 11, pp. 306–313]. However, the harmonic components of order equal to integer multiples of three are absent in the line-to-line voltage. Therefore, as seen from the 20-Hz side, the cycloconverter acts as a source of harmonic voltages of orders $n = 6k \pm 1, k = 1, 2, \cdots$ (v_n^{cyc} in Fig. 5.7). The design of the LC filter has two objectives:

1. to decrease the amplitudes of the voltage harmonics generated by the cycloconverter;

2. to increase the equivalent harmonic impedance magnitudes seen from the receiving end, indicated by $Z_R(\omega_n)$ in Fig. 5.7.

The design procedure presented here takes into account the voltage harmonics of order 5, 7, 11, and 13. For cycloconverters, the amplitude of the voltage harmonics only depends on the voltage ratio r and the fundamental power factor at the 20-Hz side, under the assumption of sinusoidal output current [104], which is sufficient for design purposes. Generally, the voltage harmonics tend to become worse with decreasing r. Here, we set $r = 0.9$. Fig. 5.8 illustrates the relationship between the per unit amplitudes of the voltage harmonics under consideration (5th, 7th, 11th, and 13th) and the power factor angle ϕ, computed based on formulas in [104, Ch. 11, p. 303]. Apparently, for the 5th and 7th voltage harmonics, the amplitudes are symmetric with respect to $\phi = 0°$, and positive ϕ (i.e., reactive power consumption by the cycloconverter) can result in reduced amplitudes of the 11th and 13th voltage harmonics. At $\phi \approx 85°$, minimum

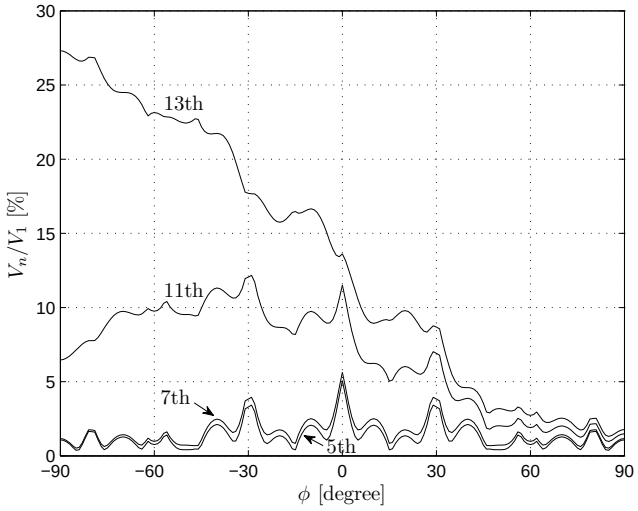

Figure 5.8 Harmonic voltage amplitudes generated by the cycloconverter at the 20-Hz side.

amplitudes are obtained. However, this value is unacceptably low, so $\phi = 35°$ is selected (for operation at rated power).

After ϕ has been determined, it follows from (5.18) and (5.19) that there is a linear relation between L_f and C_f, as in $C_f = aL_f + b$, since $\tan\phi = Q^{20}_{cyc}/P^{20}_{cyc}$. However, any ($L_f$, C_f) pair determined based on this equation should only be used as an initial guess. These initial parameters might not yield the required power factor angle ($\phi = 35°$) due to the simplifying assumptions made in the analysis. The proper LC filter parameters can be obtained by solving the circuit shown in Fig. 5.6.[2] For example, given a value for L_f, the capacitance C_f that leads to the right power factor angle can be found by searching around its initial guess value. Therefore, if L_f varies within a certain range, a number of (L_f, C_f) pairs can be obtained. Among these (L_f, C_f) candidates, a selection is made such that the magnitudes $|Z_R(\omega_n)|$ for $n = 5, 7, 11, 13$ are deemed to be adequately large. A numerical example will be provided in the next section.

[2]The circuit can be solved by formulating this as a three-bus power flow problem, where the sending end is a PQ-type bus. Since $Q_S = f(P_S, V_S)$, the power flow is solved for a range of Q_S values, until the computed V_S provides the correct value of Q_S, when substituted in $f(\cdot)$.

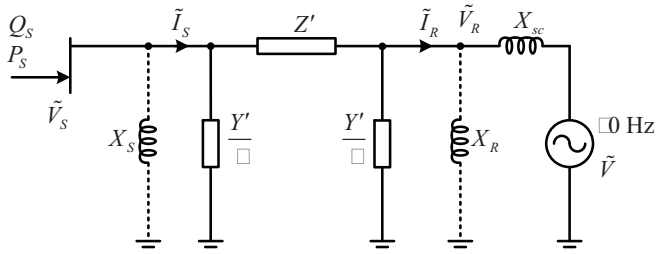

Figure 5.9 Equivalent circuit of 60-Hz transmission system.

5.5 Case Study

In this section, a design case study of a 20-Hz LFAC transmission system is presented. The transmission voltage level is chosen as 132 kV. An appropriate submarine three-core XLPE power cable is selected (nominal voltage: 132 kV, maximum voltage: 145 kV, rated current: 825 A, cross section: 1000 mm^2, copper conductor). The cable's resistance, inductance, and capacitance per km are 17.6 mΩ/km, 0.35 mH/km, and 0.25 μF/km, respectively [107, 108].

The LFAC system is compared to a conventional 60-Hz HVAC transmission system that uses the same power cable, with a steady-state single-phase equivalent circuit shown in Fig. 5.9. X_{sc} represents the short-circuit level of the 60-Hz power grid. Shunt reactive compensation (X_S and X_R in Fig. 5.9) is connected at both ends to improve the active power transmission capability, especially for long transmission distances [109]. The power grid voltage is 132 kV line-to-line. The short-circuit level is $S_{sc} = 5,000$ MVA, which is a typical value for a 132-kV system [110]. At the sending end, unity power factor is assumed ($Q_S = 0$), in order to calculate the maximum possible transmissible active power through the cable. Two cases are considered:

1. No shunt reactive compensation, i.e., $X_S = X_R = 0$. This case is denoted as '60-Hz 0/0'.

2. Shunt reactive compensation split equally between the two ends. This case is denoted as '60-Hz 50/50'. The total amount of reactive compensation is $Q_X = \mathrm{Im}\{Y'\}V_o^2$, so $X_S = X_R = 2V_o^2/Q_X$.

The relationship between sending end active power P_S and maximum transmission distance is calculated using the circuit of Fig. 5.9, and plotted in Fig. 5.10. The maximum transmission distance is obtained whenever the current or the voltage rating of the power cable is

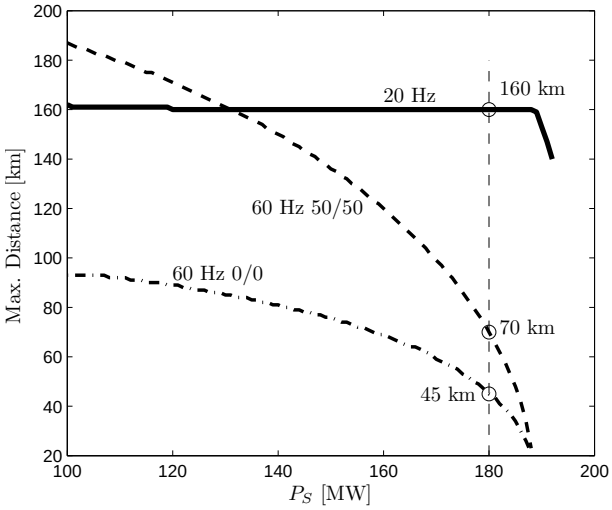

Figure 5.10 Sending end active power vs. max. transmission distance.

reached. In this case study, the cable's rated apparent power is 188 MVA. The maximum distance for transmitting 180 MW is 45 km without shunt compensation, and 70 km with shunt compensation.

The 20-Hz LFAC system is designed to transmit 180 MW over 160 km. At the sending end, the dc bus voltage level is chosen as 30 kV. A 214-MVA, 132/13.2 kV ($n_S = 10$), 20-Hz phase-shift transformer is used. With the 20-Hz rated frequency, this transformer would have larger volume compared to 60-Hz transformers. This is a drawback of the proposed LFAC system. The total size of the AC filters at the sending end is 115 MVAr.

For the cycloconverter, the voltage (line-to-line) generated at the 20-Hz side is 132 kV. The voltage ratio is selected as $r = 0.9$, and the 20-Hz side power factor angle is designed to be $\phi = 35°$. According to (5.4) and (5.5), the transformer ratio is $n_R = 1.5$, and the 60-Hz side power factor is $\text{PF}^{60} \approx 0.68$ [104]. Based on the analysis of Section 5.4.1 and equation (5.20), the apparent power rating of each cycloconverter transformer is chosen to be 100 MVA. The total size of AC filters at the 60-Hz side is 200 MVAr.

Fig. 5.11 depicts the approximate linear relation between L_f and C_f by a dashed line. The more accurate capacitance values that yield the required power factor angle are represented by the solid curve. A solution is found for L_f between 7 mH and 63 mH. Note that a solution can be obtained for L_f outside this range as well; however, in this case, either the current or

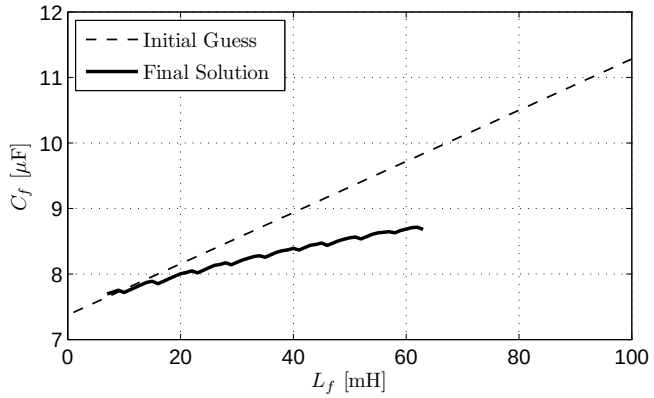

Figure 5.11 LC filter design.

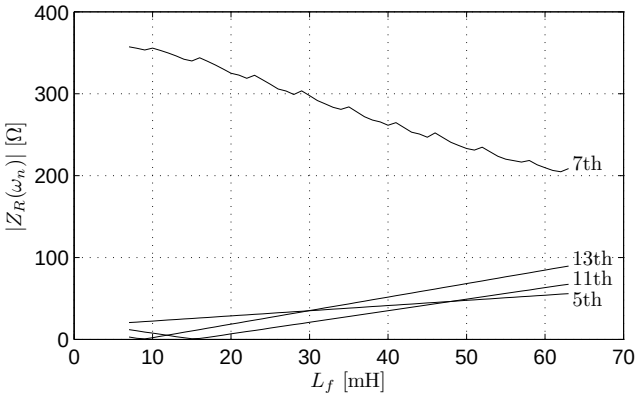

Figure 5.12 Equivalent impedance magnitude seen from the receiving end ($n = 5, 7, 11, 13$).

the voltage rating of the power cable are violated. Fig. 5.12 shows the variation of $|Z_R(\omega_n)|$ corresponding to the feasible (L_f, C_f) pairs. It can been that the LC filter with $L_f = 63$ mH and $C_f = 8.7$ μF gives the maximum impedance magnitudes for the 5th, 11th, and 13th harmonics.

Finally, based on the above system parameters, the relationship between sending-end active power and maximum transmission distance for the 20-Hz LFAC system is calculated and superimposed in Fig. 5.10. It can be observed that the proposed LFAC system is a feasible option for delivering the rated power over a distance ca. 2-3 times further than the HVAC solution. Typically, for distances longer than 100 km, HVDC systems are the preferred solution [13], but an LFAC system could be an alternative transmission technology for the 100-200 km range, at least from a technical standpoint.

5.6 Simulation Results

To demonstrate the validity of the proposed LFAC system, simulations have been carried out using Matlab/Simulink and the Piecewise Linear Electrical Circuit Simulation (PLECS) toolbox [59]. The wind power plant is rated at 180 MW, and the transmission distance is 160 km. The system parameters are listed in Table 5.1. The parameters of the PI controllers in Fig. 5.2 and Fig. 5.3 are listed in Table C.1. The transmission power cable is modeled by cascading 20 identical Π sections.

Fig. 5.13 shows the steady-state line-to-line voltage and current waveforms at the sending end, the receiving end, the 20-Hz side of the cycloconverter, and the 60-Hz power grid side under rated power conditions. The 20-Hz voltage generated from the cycloconverter has significant harmonic distortion (THD is 16.4%). Due to the LC filter, the voltages at the receiving end and the sending end have reduced THD values (3.2% and 2.2%, respectively). The measured fundamental power factor angle ϕ at the 20-Hz side of the cycloconverter is 33°, which is close to the design requirement.

Fig. 5.14 depicts the results of a transient simulation where the power from wind turbines P_w ramps from 170 MW to 180 MW, at 10 MW/s. Shown are the transient responses of the active power injected into the 60-Hz power grid, the dc bus voltage at the sending end, and the magnitude of the fundamental component of the 20-Hz voltage at the receiving end.

5.7 Conclusion

A low-frequency ac transmission system has been proposed. The methodology to design the system's components and control strategies has been discussed. The use of low frequency can improve the transmission capability of submarine power cables due to low cable charging current. The proposed LFAC system appears to be a feasible solution for the integration of offshore wind power plants over long distances. Technically, it could be used to substitute HVDC systems. Furthermore, it is easier to establish a low-frequency ac network to transmit bulk power from multiple plants.

In order to help the wind energy industry to make a better-informed decision for the trans-

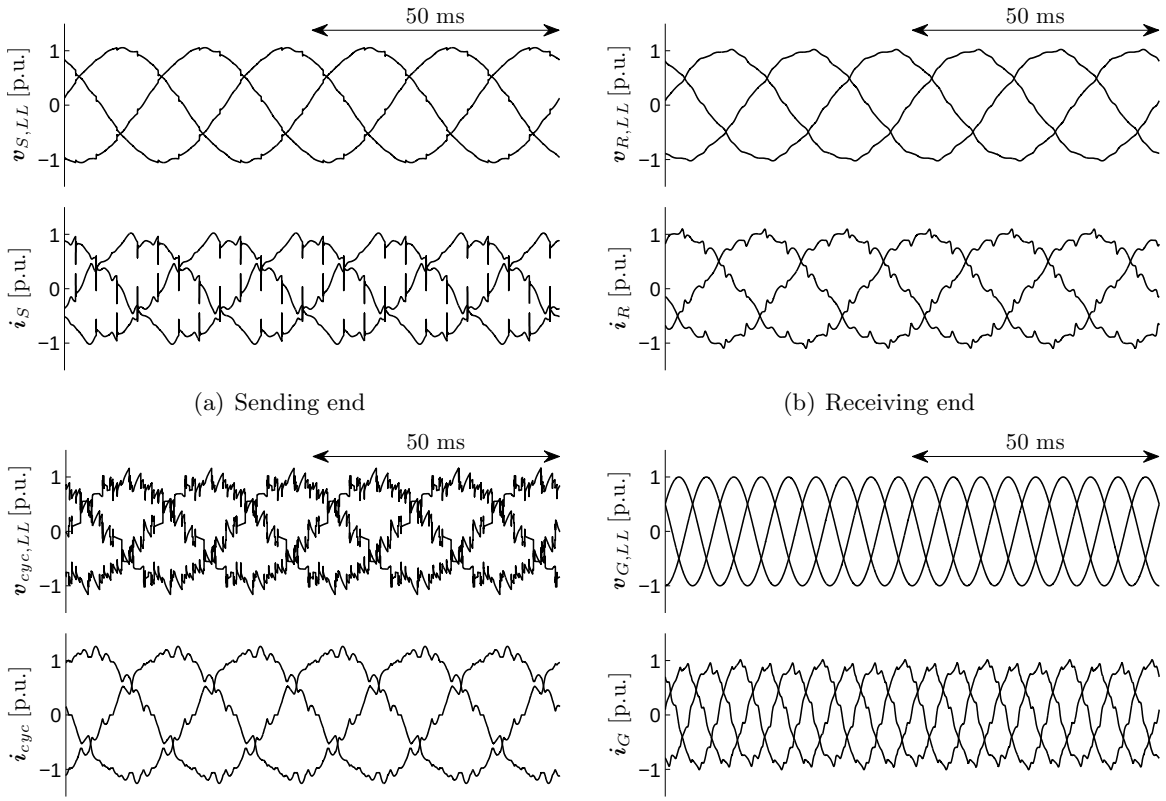

(a) Sending end

(b) Receiving end

(c) Cycloconverter 20-Hz side

(d) 60-Hz power grid side

Figure 5.13 Simulated voltage and current waveforms.

mission type for offshore wind power, it is of significance to perform a complete technical and economic comparison among HVAC, HVDC, and LFAC, e.g., transmission efficiency, transient stability, and investment evaluation. The above are subjects of ongoing work.

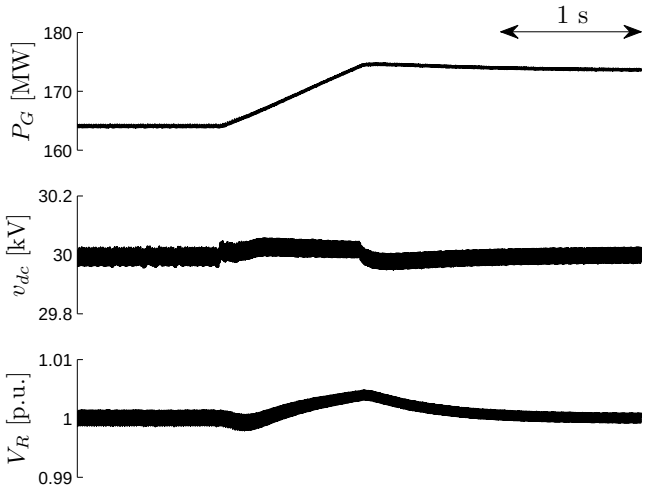

Figure 5.14 Transient waveforms.

Table 5.1 LFAC System Simulation Parameters

Sending End

DC Bus Capacitor		$C = 1000$ μF	
Smoothing Inductor		$L = 0.1$ H, $R = 1$ mΩ	
20-Hz Phase-shift Transformer			
Rated Power	214 MVA	Voltage	132/13.2 kV
Winding Resistance	0.001 p.u.	Leakage Reactance	0.05 p.u.
Magnetizing Resistance	1000 p.u.	Magnetizing Reactance	200 p.u.
AC Filters (115 MVAr, 132 kV, 20 Hz)			
	R (Ω)	L (mH)	C (μF)
11 th	0.41	29.7	17.6
13 th	0.35	21.3	17.6
$>$ 23 rd	19.7	6.8	17.6

Transmission Power Cable (132 kV)

Resistance	17.6 mΩ/km	Inductance	0.35 mH/km
Capacitance	0.25 μF/km	Rated Current	825 A

Receiving End

LC Filter		$L_f = 63$ mH, $C_f = 8.7$ μF	
Transformers			
Rated Power	100 MVA	Voltage	132/88 kV
Winding Resistance	0.001 p.u.	Leakage Reactance	0.05 p.u.
Magnetizing Resistance	1000 p.u.	Magnetizing Reactance	200 p.u.
AC Filters (200 MVAr, 132 kV, 60 Hz)			
	R (Ω)	L (mH)	C (μF)
3 rd	1.16	102.7	7.6
5 th	0.70	37.0	7.6
7 th	0.50	18.9	7.6
$>$ 9 th	38.7	11.4	7.6

Table 5.2 Parameters of PI Controllers with Transfer Function $K(1+\frac{1}{\tau s})$

	Sending end	Receiving end
K	1	0.125
τ	0.4	0.05

CHAPTER 6. DYNAMIC SIMULATION OF DFIG WIND TURBINES ON FPGA BOARDS

A paper published in the *Proceedings of the Power and Energy Conference at Illinois*, 2010

Hao Chen[1], Song Sun, Dionysios C. Aliprantis, and Joseph Zambreno

6.1 Abstract

This paper presents the implementation of a dynamic simulation of a doubly fed induction generator (DFIG)-based wind turbine on a field-programmable gate array (FPGA) board. The explicit fourth-order Runge–Kutta numerical integration algorithm is used to obtain the system dynamic response. The FPGA simulation results and speed improvement are validated versus a Matlab/Simulink simulation. Using FPGAs as computational engines can lead to significant simulation speed gains when compared to a typical PC computer, especially when operations can be efficiently parallelized on the board.

6.2 Introduction

A field-programmable gate array (FPGA) is a reconfigurable digital logic platform, which allows for the parallel execution of millions of bit-level operations in a spatially programmed environment. Research has been under way on the modeling and real-time simulation of various electrical power components using FPGAs as computational [41–44] and non-computational [46, 47] devices. Herein, the goal is to implement an entire dynamic simulation of a doubly fed induction generator (DFIG) wind turbine system on a single FPGA board as fast as possible (i.e., without being constrained by the requirement of real-time simulation).

[1]Primary researcher and author

The individual mathematical operations required by numerical integration algorithms are generally simple in terms of required logic (additions and multiplications). Hence, hardware implementations can be used to increase efficiency by reducing the overhead introduced by software, thus leading to simulation speed gains of two orders of magnitude when compared to PCs. Moreover, complex systems requiring the simultaneous solution of numerous differential equations for simulation are inherently conducive to a parallel mapping to physical computational resources. Therefore, an FPGA becomes an attractive choice for simulating complex electrical power and energy systems. Herein, a DFIG wind turbine system model is designed using very high speed integrated circuit hardware description language (VHDL), synthesized and verified using Xilinx integrated software environment (ISE). The basic steps of designing an explicit fourth-order Runge–Kutta (RK4) numerical ordinary differential equation (ODE) solver on the FPGA platform are outlined.

6.3 Modeling and Control

6.3.1 Induction Machine and Wind Turbine Model

The fifth-order induction machine model in the stationary reference frame is given by [53]:

$$v_{qs}^{s} = R_s i_{qs}^{s} + p(L_s i_{qs}^{s} + L_m i_{qr}^{\prime s}) \tag{6.1}$$

$$v_{ds}^{s} = R_s i_{ds}^{s} + p(L_s i_{ds}^{s} + L_m i_{dr}^{\prime s}) \tag{6.2}$$

$$v_{qr}^{\prime s} = R_r^{\prime} i_{qr}^{\prime s} - \omega_r(L_r^{\prime} i_{dr}^{\prime s} + L_m i_{ds}^{s}) + p(L_r^{\prime} i_{qr}^{\prime s} + L_m i_{qs}^{s}) \tag{6.3}$$

$$v_{dr}^{\prime s} = R_r^{\prime} i_{dr}^{\prime s} + \omega_r(L_r^{\prime} i_{qr}^{\prime s} + L_m i_{qs}^{s}) + p(L_r^{\prime} i_{dr}^{\prime s} + L_m i_{ds}^{s}) \tag{6.4}$$

$$p\omega_r = \tfrac{P}{2J}(T_e - T_m - B\tfrac{2}{P}\omega_r) \tag{6.5}$$

$$T_e = 0.75PL_m(i_{qs}^{s} i_{dr}^{\prime s} - i_{ds}^{s} i_{qr}^{\prime s}) \tag{6.6}$$

where $p = \frac{d}{dt}$ is the differentiation operator; R_s and $R_r^{\prime}$ are the stator and rotor resistances; L_s and $L_r^{\prime}$ are the stator and rotor inductances; L_m is the magnetizing inductance; v_{qs}^{s}, v_{ds}^{s}, i_{qs}^{s}, and i_{ds}^{s} are the qd-axes stator voltages and currents; $v_{qr}^{\prime s}$, $v_{dr}^{\prime s}$, $i_{qr}^{\prime s}$, and $i_{dr}^{\prime s}$ are the qd-axes rotor voltages and currents; ω_r is the rotor angular electrical speed; T_m and T_e are mechanical

and electromagnetic torque; P is the number of poles; J is the total rotor inertia; and B is a friction coefficient.

The wind turbine model is based on the relation between the upstream wind speed v_w and the mechanical power P_m extracted from the wind [48]. The pertinent equations are

$$P_m = \tfrac{1}{2}\rho\pi R_w^2 c_p\left(\lambda,\beta\right) v_w^3 \tag{6.7}$$

$$c_p\left(\lambda,\beta\right) = 0.5176\left(\tfrac{116}{\lambda_i} - 0.4\beta - 5\right) e^{\frac{-21}{\lambda_i}} + 0.0068\lambda \tag{6.8}$$

$$\frac{1}{\lambda_i} = \frac{1}{\lambda + 0.08\beta} - \frac{0.035}{\beta^3 + 1} \tag{6.9}$$

where ρ is the air density; R_w is the wind turbine radius; $c_p\left(\lambda,\beta\right)$ is the performance coefficient; β is the pitch angle in degrees; and λ is the tip-speed ratio given by $\lambda = \omega_w R_w / v_w$, where ω_w is the wind turbine rotor speed. Note that the relation between ω_w and ω_r is determined by the gearbox ratio. For $\beta = 0$, the performance coefficient attains its maximum value $c_p^{\max} = 0.48$ for an optimal $\lambda_{op} = 8.10$. The mechanical torque applied to the generator shaft is $T_m = \frac{P}{2}\frac{P_m}{\omega_r}$.

6.3.2 DFIG Control

An essential characteristic of DFIG control strategy is that the generated active and reactive powers can be controlled independently. It is common to use the air-gap flux oriented vector control [111] or the stator flux oriented vector control [5,112,113], under the assumption of negligible stator resistances. In particular, it has been shown that stator flux orientation can cause instability under certain operating conditions [114]. Herein, a stator voltage oriented vector control without the assumption of negligible stator resistances is presented. The overall control structure of back-to-back pulse-width modulated (PWM) converters is shown in Fig. 6.1. The reference frame transformation matrices $\mathbf{K}_s^s$, $\mathbf{K}_r^s$, $\mathbf{K}_s^e$, ${}^s\mathbf{K}^e$, ${}^e\mathbf{K}^s$, and ${}^e\mathbf{K}^r$ are defined in [53].

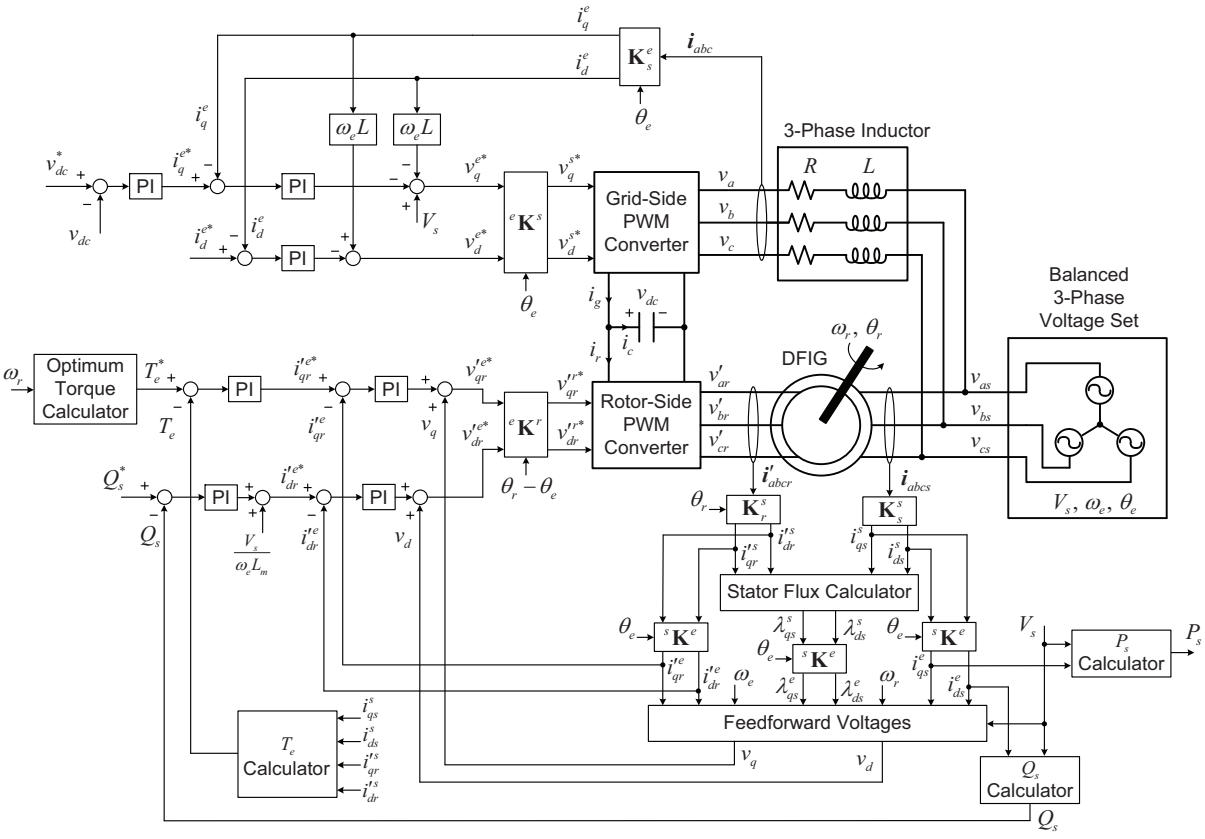

Figure 6.1 Control block diagram for DFIG

6.3.2.1 Rotor current control

Aligning the stator voltage vector with the q-axis, the induction machine voltage equations in the synchronous reference frame can be written as

$$V_s = R_s i^e_{qs} + \omega_e \lambda^e_{ds} + p\lambda^e_{qs} \tag{6.10}$$

$$0 = R_s i^e_{ds} - \omega_e \lambda^e_{qs} + p\lambda^e_{ds} \tag{6.11}$$

$$v'^e_{qr} = R'_r i'^e_{qr} + (\omega_e - \omega_r)\lambda'^e_{dr} + p\lambda'^e_{qr} \tag{6.12}$$

$$v'^e_{dr} = R'_r i'^e_{dr} - (\omega_e - \omega_r)\lambda'^e_{qr} + p\lambda'^e_{dr} \tag{6.13}$$

where V_s is the stator voltage amplitude, and ω_e is the stator voltage angular frequency. The rotor flux linkage equations are

$$\lambda'^e_{qr} = L'_r i'^e_{qr} + L_m i^e_{qs} = (L_m/L_s)\lambda^e_{qs} + \sigma L'_r i'^e_{qr} \tag{6.14}$$

$$\lambda'^e_{dr} = L'_r i'^e_{dr} + L_m i^e_{ds} = (L_m/L_s)\lambda^e_{ds} + \sigma L'_r i'^e_{dr} \tag{6.15}$$

where $\sigma = 1 - L_m^2/L_s L'_r$. Substituting (6.14) and (6.15) into (6.12) and (6.13) yields

$$\begin{aligned} v'^{e*}_{qr} = v'^e_{qr} &= R'_r i'^e_{qr} + \sigma L'_r p i'^e_{qr} + v_q \\ &= K_q \left(1 + \frac{1}{\tau_q s}\right)(i'^{e*}_{qr} - i'^e_{qr}) + v_q \end{aligned} \tag{6.16}$$

$$\begin{aligned} v'^{e*}_{dr} = v'^e_{dr} &= R'_r i'^e_{dr} + \sigma L'_r p i'^e_{dr} + v_d \\ &= K_d \left(1 + \frac{1}{\tau_d s}\right)(i'^{e*}_{dr} - i'^e_{dr}) + v_d \end{aligned} \tag{6.17}$$

where v_q and v_d are compensating feedforward voltages given by

$$v_q = \tfrac{L_m}{L_s} p\lambda^e_{qs} + (\omega_e - \omega_r)[\sigma L'_r i'^e_{dr} + \tfrac{L_m}{L_s}\lambda^e_{ds}] \tag{6.18}$$

$$v_d = \tfrac{L_m}{L_s} p\lambda^e_{ds} - (\omega_e - \omega_r)[\sigma L'_r i'^e_{qr} + \tfrac{L_m}{L_s}\lambda^e_{qs}] \tag{6.19}$$

and K_q, τ_q, K_d, and τ_d are parameters of two PI current controllers. The stator flux linkages (λ^e_{qs}, λ^e_{ds}) are computed from the stator and rotor current measurements. The derivatives $p\lambda^e_{qs}$ and $p\lambda^e_{ds}$ are obtained from (6.10) and (6.11).

6.3.2.2 Torque and power control

The optimal electromagnetic torque reference T_e^* shown in Fig. 6.1, after compensating for the friction losses, is given by [5, 112]

$$T_e^* = \frac{P}{2}\frac{K_1^3 K_2\, c_p^{\max}\omega_r^2}{\lambda_{op}^3} - B\frac{2}{P}\omega_r \tag{6.20}$$

where $K_1 = 2R_w/GP$, $K_2 = \frac{1}{2}\rho\pi R_w^2$, and G is the gearbox ratio.

6.3.2.3 Grid-side converter control

The purpose of the grid-side converter is to regulate the DC-link voltage [112]. The vector control approach shown in Fig. 6.1 is used. Aligning the stator voltage vector with the q-axis, the voltage equations in the synchronous reference frame can be written as

$$v_{qs}^e = V_s = Ri_q^e + Lpi_q^e + \omega_e L i_d^e + v_q^e \tag{6.21}$$

$$v_{ds}^e = 0 = Ri_d^e + Lpi_d^e - \omega_e L i_q^e + v_d^e \tag{6.22}$$

where R and L are the resistance and inductance of the current's filter inductors, and v_q^e, v_d^e, i_q^e, and i_d^e are the qd-axis converter input voltages and currents. From (6.21) and (6.22), the converter voltage references v_q^{e*} and v_d^{e*} are

$$\begin{aligned} v_q^{e*} = v_q^e &= -\left(Ri_q^e + Lpi_q^e\right) + V_s - \omega_e L i_d^e \\ &= -K_{qg}\left(1 + \frac{1}{\tau_{qg}s}\right)(i_q^{e*} - i_q^e) + V_s - \omega_e L i_d^e \end{aligned} \tag{6.23}$$

$$\begin{aligned} v_d^{e*} = v_d^e &= -\left(Ri_d^e + Lpi_d^e\right) + \omega_e L i_q^e \\ &= -K_{dg}\left(1 + \frac{1}{\tau_{dg}s}\right)(i_d^{e*} - i_d^e) + \omega_e L i_d^e \end{aligned} \tag{6.24}$$

where K_{qg}, τ_{qg}, K_{dg}, and τ_{dg} are parameters of two PI current controllers. Herein, i_d^{e*} is arbitrarily set to zero in order to set the stator-side reactive power to zero, but this is not always necessary in practice.

6.4 FPGA Implementation

6.4.1 Simulation Architecture

The transient response of the system is obtained by the RK4 numerical integration algorithm [115]. This is a fixed-step explicit integration algorithm, which is based on simple numerical calculations (additions and multiplications), and is thus straightforward to implement on the FPGA. The RK4 method for the initial value problem ($p\mathbf{x} = \mathbf{f}(t, \mathbf{x}), \mathbf{x}(t_0) = \mathbf{x}_0$) is described by:

$$\mathbf{x}_n = \mathbf{x}_{n-1} + \frac{h}{6}\left(\mathbf{k}_1 + 2\mathbf{k}_2 + 2\mathbf{k}_3 + \mathbf{k}_4\right) \tag{6.25}$$

$$t_n = t_{n-1} + h \tag{6.26}$$

where $\mathbf{x}_n$ is the RK4 approximation of $\mathbf{x}(t_n)$ (i.e., the exact solution), h is the time step, and

$$\mathbf{k}_1 = \mathbf{f}\left(t_{n-1}, \mathbf{x}_{n-1}\right) \tag{6.27}$$

$$\mathbf{k}_2 = \mathbf{f}\left(t_{n-1} + 0.5h, \mathbf{x}_{n-1} + 0.5h\mathbf{k}_1\right) \tag{6.28}$$

$$\mathbf{k}_3 = \mathbf{f}\left(t_{n-1} + 0.5h, \mathbf{x}_{n-1} + 0.5h\mathbf{k}_2\right) \tag{6.29}$$

$$\mathbf{k}_4 = \mathbf{f}\left(t_{n-1} + h, \mathbf{x}_{n-1} + h\mathbf{k}_3\right) . \tag{6.30}$$

The ODEs representing the entire DFIG system, expressed in the form $p\mathbf{x} = \mathbf{f}(t, \mathbf{x})$, are derived by combining the induction machine model, wind turbine model and DFIG control strategy. The state variables are i^s_{qs}, i^s_{ds}, i'^s_{qr}, i'^s_{dr}, ω_r, the integrators of four PI controllers for the rotor-side converter (x_6, x_7, x_8, and x_9), the three-phase RL circuit qd currents in the stationary reference frame (i^s_q and i^s_d), the DC-link voltage v_{dc}, and the integrators of three PI controllers for the grid-side converter (x_{13}, x_{14}, and x_{15}). The input variables are v^s_{qs}, v^s_{ds}, the wind speed v_w, the pitch angle β, the reactive power reference Q^*_s, the DC-link voltage reference v^*_{dc}, and the three-phase RL circuit d-axis current reference in the synchronous reference frame i^{e*}_d. The output variables are the stator-side active and reactive power.

As shown in Fig. 6.2, four functional modules are used to establish the entire system. The "Stator Voltage Input" module is responsible for the generation of v^s_{qs} and v^s_{ds}. The "ODE Function" and "Vector Update" modules constitute the RK4 solver. The "Output" module

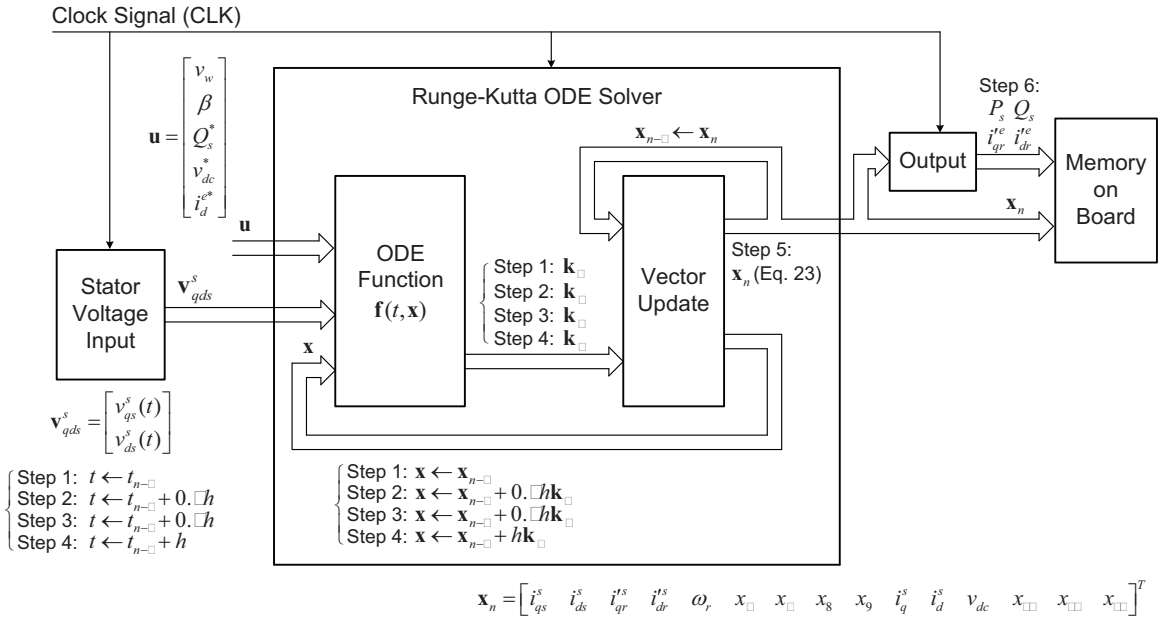

Figure 6.2 FPGA implementation of DFIG wind turbine system

implements the calculation of the stator-side active and reactive power (P_s and Q_s) and the machine rotor qd-axes currents in the synchronous reference frame (i'^e_{qr} and i'^e_{dr}). These modules have been developed using VHDL in ModelSim, which is a verification and simulation tool for VHDL designs. All variables and parameters are represented as signed fixed-point numbers with 13 bits representing the integral part, and 32 bits representing the fractional part. This provides a numerical range that can accommodate every variable involved in the simulation, with a resolution of 2^{-32}. For economizing FPGA resources, the per unit system is used in order to decrease the necessary number of bits (because variables are expected to be close to 1.0).

Every RK4 iteration shown in Fig. 6.3 consists of six steps. The "ODE Function" module executes the evaluation of $\mathbf{f}(t, \mathbf{x})$. The "Vector Update" module is responsible for the alteration of $\mathbf{x}$ in $\mathbf{f}(t, \mathbf{x})$ during steps 2, 3, and 4, as well as the calculation of (6.25) in step 5. Since v^s_{qs} and v^s_{ds} are dependent on the time t, the "Stator Voltage Input" module should generate the appropriate v^s_{qs} and v^s_{ds} for the "ODE Function" module. Specifically, $v^s_{qs}(t_{n-1} + 0.5h)$ and $v^s_{ds}(t_{n-1} + 0.5h)$ are generated during step 1 and stored for the usage of the "ODE Function" module in step 2 and step 3, while $v^s_{qs}(t_{n-1} + h)$ and $v^s_{ds}(t_{n-1} + h)$ are generated during step 3

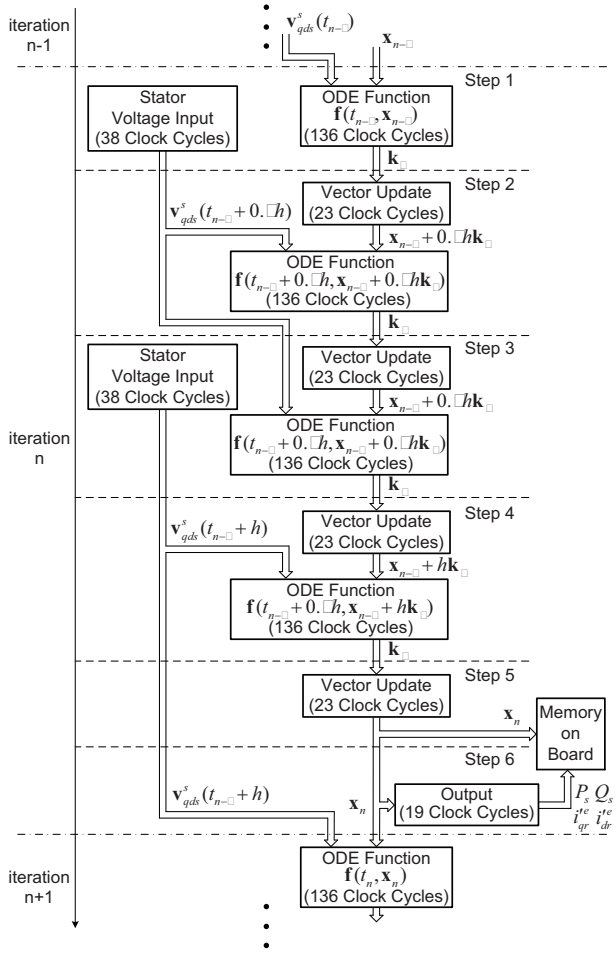

Figure 6.3 RK4 iteration process

and stored for the usage of the "ODE Function" module in step 4 and step 1 of the next iteration. Note that the "Stator Voltage Input" module and the "ODE Function" module are executed in parallel in step 1. A similar parallel execution is also performed in step 3. On the other hand, the "ODE Function" module and the "Vector Update" module have to be executed in serial pattern because the inputs of one strictly depend on the outputs of the other.

To design a sinusoidal function involved in the 'Stator Voltage Input' module, a look-up table approach is followed [68]. The evaluation of the exponential function involved in (C.1) is based on the following identities [116]:

$$\begin{aligned} e^{x} &= 2^{x \log_2 e} \\ &= 2^{x_i} 2^{x_f} = 2^{x_i} e^{x_f \ln 2}, \quad x > 0 \end{aligned} \tag{6.31}$$

$$e^x = 2^{x \log_2 e}$$
$$= 2^{x_i - 1} 2^{x_f + 1} = 2^{x_i - 1} e^{(x_f + 1) \ln 2}, \quad x < 0 \tag{6.32}$$

where x_i and x_f are the integer and fractional part of $x \log_2 e$, respectively.[2] Since $0 < x_f \ln 2 < 1$ in (6.31) and $0 < (x_f + 1) \ln 2 < 1$ in (6.32), the 32 bits representing these decimal fractions can be divided into 3 sections: bits 2^{-1} to 2^{-8} (x_H), bits 2^{-9} to 2^{-16} (x_L) and bits 2^{-17} to 2^{-32} (x_T). e^{x_H} and e^{x_L} are obtained using two exponential look-up tables (named as 'high 8 table' and 'low 8 table'). Each of them contains 256 elements. e^{x_T} is calculated by Taylor series expansion ($e^{x_T} \approx 1 + x_T$). Thus,

$$e^x = 2^{x_i} e^{x_H} e^{x_L} (1 + x_T), \quad x > 0 \quad \text{or}$$
$$e^x = 2^{x_i - 1} e^{x_H} e^{x_L} (1 + x_T), \quad x < 0 \,.$$

The multiplication by 2^{x_i} or $2^{x_i - 1}$ is executed by a bit-shifting operation.

6.4.2 Synthesis and Implementation

After the functionality and results of all modules designed using VHDL were validated in the ModelSim environment, the Xilinx ISE was used to develop, synthesize, and verify the substantial top-level wrapper module together with the DFIG wind turbine system model. The target FPGA device was Xilinx Virtex-5 XC5VLX330. The post-place and route report presented the FPGA hardware resources usage as shown in Table 6.1, and the maximum frequency of the clock signal that can be applied is 221.533 MHz. Generally, the consumption of FPGA hardware resources increases with the model complexity. Note that the entire design for the DFIG wind turbine system must fit within the resource limitation of the target FPGA device. Otherwise, an FPGA device with more hardware resources should be chosen or the model should be redesigned in order to meet the requirement of the FPGA device. The final system will be integrated on a development board that features the XC5VLX330 device—for example, Xilinx Virtex-5 and DDR2 SDRAM multi-application platform board. The simulation output data will be stored in the memory embedded on the development board.

[2] For example, if $x \log_2 e = 2.3$, then $x_i = 2$ and $x_f = 0.3$; if $x \log_2 e = -2.3$, then $x_i = -2$ and $x_f = -0.3$.

Table 6.1 Xilinx Virtex–5 XC5VLX330 resources usage summary

Logic Utilization	Used	Available	Utilization
Number of Slice Registers	86288	207360	41%
Number of Slice LUTs (Look Up Tables)	80997	207360	39%
Number of LUT-FF (Flip Flop) pairs	91913	207360	44%

6.5 Simulation Results

The simulation parameters are shown in Table 6.2. The moment of inertia J was set to 2 kg·m^2 (an unrealistically low value) in order to reduce the simulation time required to reach a steady-state operating condition. An average-value model is used to represent the rotor-side and grid-side converters shown in Fig. 6.1. The ModelSim clock frequency was (arbitrarily) set to 200 MHz, a value less than the maximum clock frequency (221.533 MHz) in the post-place and route report of the Xilinx ISE. The simulation time-step h was 10^{-4} s.

The exact same DFIG wind turbine system was also implemented in Matlab/Simulink. The verification of the results coming from ModelSim was performed versus a Simulink simulation using the ODE23tb solver with a maximum time step of 10^{-5} s. Fig. 6.4 shows the machine stator and rotor qd-axes currents in the synchronous reference frame (i^e_{qs}, i^e_{ds}, i'^e_{qr}, and i'^e_{dr}), the stator-side active and reactive power (P_s and Q_s), the rotor angular electrical speed ω_r, and the DC-link voltage v_{dc}. The wind speed v_w was stepped down from 7 m/s to 5 m/s at $t = 1$ s, and the reactive power reference Q^*_s was stepped up from 10 kVAR to 50 kVAR at $t = 3$ s. Note that in the per unit system, the value of i^e_{qs} is equal to that of P_s and the value of i^e_{ds} is equal to that of Q_s. The ModelSim waveforms are superimposed on the Simulink waveforms, but they are so close that differences cannot be distinguished.

To compare simulation speed, we ran the simulation using the ODE45 and ODE23 integration algorithms of Simulink with maximum step size of 10^{-4} s (typically the two "simplest" available solvers), because they are implementations of the explicit Runge–Kutta algorithm, albeit of a variable-step nature. The simulation speed was further increased by using the "Ac-

Table 6.2 Simulation parameters

R_s	1.4×10^{-3} Ω	P	4	β	0°	τ_{T_e}	0.0158
R'_r	9.92×10^{-4} Ω	ω_e	$2\pi 60$ rad/s	C	4000 μF	K_{Q_s}	0.0024
L_s	1.616 mH	J	2 kg·m^2	R	0.1 Ω	τ_{Q_s}	0.0158
L'_r	1.608 mH	P_{rated}	2 MW	L	1.75 mH	K_q, K_d	0.0474
L_m	1.526 mH	R_w	35 m	v^*_{dc}	700 V	τ_q, τ_d	0.0135
V_s	$690\sqrt{2/3}$ V	G	120	i^{e*}_d	0 A	K_{qg}, K_{dg}	1.3
B	0.01 N·m·s	ρ	1.25 kg/m^3	K_{T_e}	0.4488	τ_{qg}, τ_{dg}	0.0023
$K_{V_{dc}}$	0.5773	$\tau_{V_{dc}}$	0.02				

celerator" mode of Simulink, which replaces normal interpreted code with compiled code. The simulation times on an Intel Core2 Duo 2.2 GHz computer were 6.7 s for ODE45 and 4.7 s for ODE23. The FPGA simulation time predicted by ModelSim was 0.166 s, which represents a 40x speed gain. The simulation time will be further decreased if the clock frequency can be set to a higher value, if the simulation time step h is increased, or if a lower-order integration algorithm (e.g., the trapezoidal algorithm) is used.

6.6 Conclusion

This paper presented the FPGA implementation of a DFIG wind turbine system dynamic simulation, using the RK4 numerical integration algorithm. The entire system has been developed using VHDL, synthesized using the Xilinx ISE, and will be implemented on an FPGA board. An optimal VHDL design should be sought for the purpose of economizing FPGA hardware resources, especially when the model has high complexity. A comparison between the simulation results from FPGA and Simulink demonstrates the validity of this implementation. The 40x simulation speed gain demonstrates the performance advantage of FPGAs compared to PC-based simulations.

FPGAs represent an interesting possibility for simulating more complex electrical power and power electronics-based systems because of their flexibility, high processing rates and possibility to parallelize numerical integration computations. In principle, FGPAs could be coupled with other simulation platforms to perform multi-rate co-simulation of complex sys-

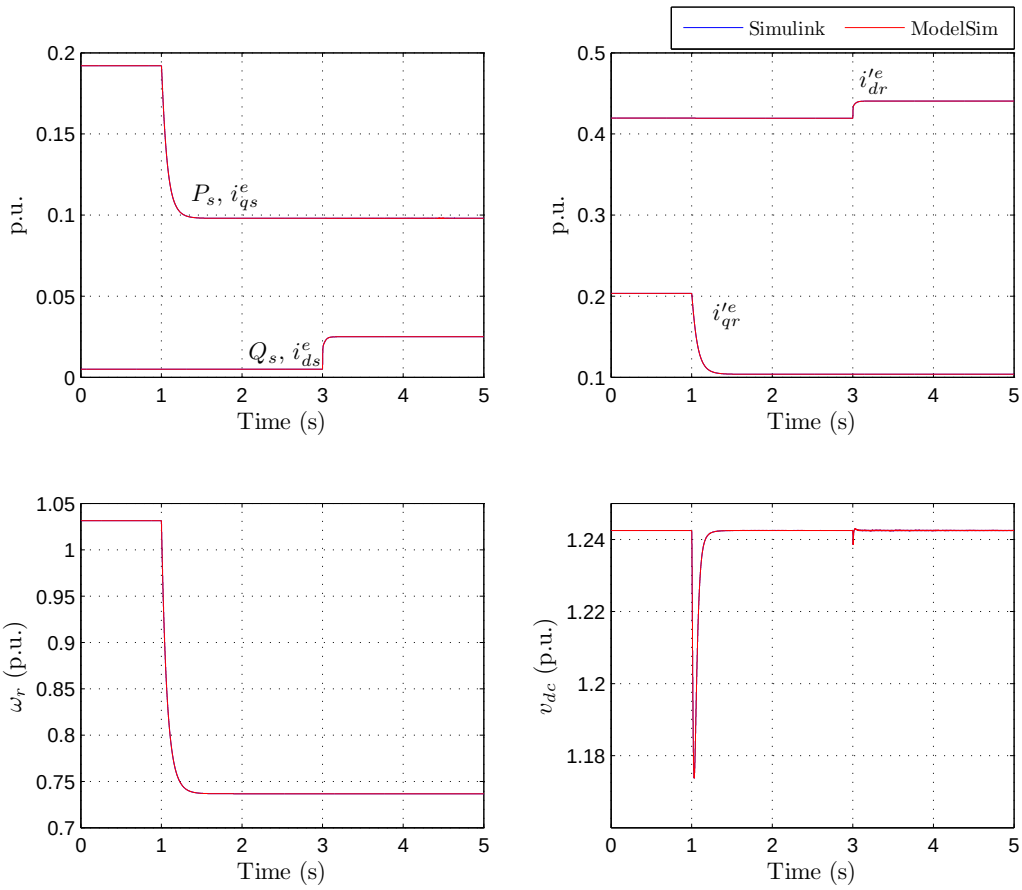

Figure 6.4 Simulation results

tems. To accelerate the dynamic simulations, FPGAs would simulate faster subsystems that require smaller integration time steps. However, it has been observed that the data exchange rate with an FPGA can be a critical bottleneck for developing such co-simulation applications, especially when it is required to achieve real-time simulation speeds. On the other hand, a pipeline VHDL design [117, 118] of a DFIG wind energy conversion system can potentially enable the dynamic simulation of entire wind farms (containing hundreds of turbines) on a single FPGA board.

CHAPTER 7. CONCLUSION

7.1 Contributions

This dissertation has presented novel technological solutions for more efficient and reliable wind energy conversion systems, wind power transmission systems, and electric system simulation platforms. The most significant contributions and conclusions of this work can be summarized as follows.

1. Two novel variable-speed wind energy conversion systems consisting of either a squirrel-cage induction generator (SCIG) or a permanent-magnet synchronous generator (PMSG) and a Vienna rectifier, have been proposed and analyzed.

   For the SCIG/Vienna rectifier configuration, an LC filter based on a switched capacitor bank is utilized to obtain a wide speed operational range. The switching and conduction losses of the power semiconductors in the Vienna rectifier were obtained by simulations, and compared to the losses incurred by a similar six-switch converter. The results show that the proposed system has potential to be more efficient and reliable.

   For the PMSG/Vienna rectifier configuration, we have identified restrictions on the system's operational range imposed by the current, voltage, and power factor limitations of the Vienna rectifier. Even with these in place, the system can function throughout the entire wind speed range. Detailed power loss calculations in the power electronics converter and the generator itself are used to design a control strategy that leads to maximum energy efficiency. Simulation results reveal that this configuration is advantageous with respect to energy efficiency compared to a traditional six-switch two-level converter.

   Two laboratory prototypes have been implemented to validate the analysis and feasibility

of the proposed systems.

2. A novel low-frequency ac transmission system has been proposed to connect dc collection based offshore wind power plants with the main onshore power grid.

   Control strategies for the 12-pulse thyristor-based converter at the sending end and the thyristor-based cycloconverter at the receiving end have been devised.

   Steady-state and harmonic analyses have been performed to illustrate the process for determining the major system component parameters.

   A design case study has demonstrated the advantage of the proposed LFAC system over the conventional HVAC system. Time-domain simulation studies are used to illustrate variables of interest.

3. The FPGA implementation of a DFIG wind turbine system dynamic simulation, using the RK4 numerical integration algorithm has been presented.

   The entire system has been developed using VHDL, synthesized and verified using the Xilinx ISE. An optimal VHDL design should be sought for the purpose of economizing FPGA hardware resources, especially when the model has high complexity. A comparison between the simulation results from FPGA and Simulink demonstrates the validity of this implementation. The obtained 40x simulation speed gain demonstrates the performance advantage of FPGAs compared to PC-based simulations.

7.2 Future Work

Based on what has been accomplished so far in this dissertation, several suggestions for further research work are provided below:

1. The proposed SCIG/Vienna rectifier and PMSG/Vienna rectifier configurations constitute new promising design options that should be investigated in more depth. Important issues are related to the economic considerations of these topologies versus classical counterparts; the effect of the Vienna rectifier on the generator performance, including

an accurate determination of harmonics-related losses on generator; a detailed system-level energy loss comparison that includes different types of grid-side converters; the quantification of the possible reliability enhancement due to the reduced voltage stress on power electronics switches; alternate control strategies (for example, controller design using the linear quadratic regulator method) and optimal modulation schemes to improve system dynamics; and the feasibility of using the proposed configurations to establish dc collection grids within wind power plants.

2. For wind power transmission systems, the proposed low-frequency ac transmission system has been demonstrated to be a feasible option for delivering large amount of power over long distances. A comprehensive and accurate transmission energy loss, taking into account the loss of the transformers, converters, and AC filters, is a worthwhile topic for further analysis. In addition, it is of significance to perform a complete technical and economic comparison among HVAC, HVDC, and LFAC, in order to help the industry to make better-informed decisions.

3. FPGA represents an interesting possibility for simulating complex electrical power and power electronics-based systems because of its flexibility, high processing rates and capability to parallelize numerical integration computations. In principle, FGPA boards could be coupled with other simulation platforms, for example, RTDS or other PC-based simulation platforms, to perform multi-rate co-simulation of complex systems. To accelerate the dynamic simulations, FPGA would simulate faster subsystems that require smaller integration time steps. Moreover, it might be of interest to develop a pipeline VHDL design of a DFIG wind energy conversion system. With the pipeline design, the dynamic simulation of an entire wind power plant (containing hundreds of turbines) on a single FPGA board could be possible.

APPENDIX A. PARAMETERS OF INDUCTION MACHINE AND WIND TURBINE

The 4-pole, 60-Hz induction machine parameters are as follows [53]: rated power = 50 hp; rated voltage (line-to-line rms value) = 460 V; $R_s = 0.087\ \Omega$; $R'_r = 0.228\ \Omega$; $X_{ls} = X'_{lr} = 0.302\ \Omega$; $X_m = 13.08\ \Omega$. The reactances are expressed in Ω at $\omega_b = 2\pi 60$ rad/s. The LC filter parameters are: $C_1 = 638\ \mu$F, $L_1 = 1.8$ mH, $C_2 = 370\ \mu$F, and $L_2 = 3.0$ mH. The AC voltage rating of C_1 and C_2 is chosen as 400 Vrms according to $|\tilde{V}_m|_{\max}$ in Figs. 2.6 and 2.8.

The wind turbine parameters listed below are chosen such that the rated power and speed of the machine are reached at the rated wind speed: $R_w = 4.8$ m; $G = 9.3$; rated wind speed = 12 m/s. The performance coefficient is [48]

$$c_p(\lambda, \gamma) = 0.5176 \left(\frac{116}{\lambda_i} - 0.4\gamma - 5 \right) e^{\frac{-21}{\lambda_i}} + 0.0068\lambda\,, \tag{A.1}$$

with $\frac{1}{\lambda_i} = \frac{1}{\lambda + 0.08\gamma} - \frac{0.035}{\gamma^3 + 1}$.

APPENDIX B. WIND TURBINE AND INDUCTION GENERATOR PARAMETERS FOR SIMULATION AND EXPERIMENTS

B.1 Wind Turbine and Induction Generator Simulation Parameters

For simulation purposes, a 300-kW, 4-pole, 50-Hz induction generator is used, with parameters obtained from [119]: rated voltage (line-to-line rms) = 415 V; base voltage = $415/\sqrt{3}$ V; base current = $300,000/\sqrt{3}/415 = 417$ A; $R_s = 0.004\ \Omega$; $R'_r = 0.0032\ \Omega$; $X_{ls} = 0.0383\ \Omega$, $X'_{lr} = 0.0772\ \Omega$; $X_m = 1.56\ \Omega$; $\Lambda'_r = 1.08$ Vs. The arctangent function representing the main flux path magnetization is given by [71]

$$\Lambda_m(I_m) = \frac{2M_d}{\pi}\left[(I_m - I_{mT})\arctan\left(\tau_T(I_m - I_{mT})\right) - I_{mT}\arctan\left(\tau_T I_{mT}\right)\right] + \frac{M_d}{\pi\tau_T}\left[\ln\left(1+\tau_T^2 I_{mT}^2\right) - \ln\left(1+\tau_T^2(I_m - I_{mT})^2\right)\right] + M_a I_m\,, \quad \text{(B.1)}$$

where $I_{mT} = 156$ A, $\tau_T = 0.05\ \text{A}^{-1}$, $M_a = \frac{M_f+M_i}{2}$, $M_d = \frac{M_f-M_i}{2}$, $M_i = 7.0$ mH and $M_f = 0.06M_i$.

The wind turbine parameters listed below are chosen such that the rated power and speed of the machine are reached at the rated wind speed: $R_w = 17.5$ m; $G = 32$; cut-in wind speed = 3 m/s; rated wind speed = 10.5 m/s. The performance coefficient is modeled by [48]

$$c_p(\lambda,\gamma) = 0.5\left(\frac{116}{\lambda_i} - 0.4\gamma - 5\right)e^{\frac{-21}{\lambda_i}}\,, \quad \text{(B.2)}$$

with $\frac{1}{\lambda_i} = \frac{1}{\lambda+0.08\gamma} - \frac{0.035}{\gamma^3+1}$, where $c_p(\lambda,0)$ attains its maximum value $c_p^{\max} = 0.41$ for an optimal $\lambda_o = 7.95$.

B.2 Laboratory Prototype Parameters

The experiments were conducted using a 1/4-HP, 4-pole, 60-Hz induction machine with the following parameters: rated voltage (line-to-line rms) = 208 V; $R_s = R'_r = 12.3\ \Omega$; $L_{ls} = L'_{lr} = 68.6$ mH; $L_{m0} = 0.44$ H (unsaturated magnetizing inductance); $\Lambda'_r = 0.40$ Vs. The saturation characteristic parameters in (B.1) are: $I_{mT} = 1.22$ A, $\tau_T = 3\ \text{A}^{-1}$, $M_i = L_{m0}$, and $M_f = 0.0167$ H.

The prime mover was a separately-excited 1/4-HP dc machine, with parameters: $R_a = 6.7\ \Omega$ (armature winding resistance); $R_f = 263.6\ \Omega$ (field winding resistance); $R_{fx} = 412\ \Omega$ (external resistance connected in series with the field winding); $L_a = 0.073$ H (self-inductance of the armature winding); $L_f = 11.34$ H (self-inductance of the field winding); $L_{af} = 2.62$ H (mutual-inductance between the armature and field winding). The friction coefficient of the system is $F = 0.002\ \text{N} \cdot \text{m} \cdot \text{s/rad}$.

The LC filter parameters are: $C = 8.1\ \mu$F, $L = 0.2$ H, and $R_L = 4\ \Omega$ (inductor's resistance).

APPENDIX C. WIND TURBINE AND PERMANENT-MAGNET SYNCHRONOUS GENERATOR PARAMETERS FOR SIMULATION AND EXPERIMENTS

C.1 Wind Turbine Parameters for Analysis and Simulation

The generator is a 16-pole, 60-Hz, 1.5-MW, 1.5-kV PMSG, assumed to be Y-connected, with the following parameters: $R_s = 0.022\ \Omega$; $X_q = 1.266\ \Omega$; $X_d = 0.662\ \Omega$; $\lambda_m = 2.984$ Vs. The dc-link voltage V_o is set to 2800 V. The per unit system bases are defined as: base power = 1.5 MVA; base voltage (peak of line-neutral voltage) $= 1.5\sqrt{2/3}$ kV; base current (peak of line current) = 816.5 A; base speed = 377 rad/s. The maximum stator current $I_{s\,\max} = 1.1$ p.u.

The wind turbine parameters are as follows: $A = 6362\ \text{m}^2$; gearbox ratio = 27; cut-in wind speed $v_w^{\text{in}} = 4$ m/s; rated wind speed $v_w^{\text{rated}} = 9.8$ m/s; cut-out wind speed $v_w^{\text{out}} = 25$ m/s. The performance coefficient is modeled by [48]

$$c_p\left(\lambda,\gamma\right) = 0.5\left(\frac{116}{\lambda_i} - 0.4\gamma - 5\right)e^{\frac{-21}{\lambda_i}},$$

with $\frac{1}{\lambda_i} = \frac{1}{\lambda+0.08\gamma} - \frac{0.035}{\gamma^3+1}$. When $\gamma = 0$, the performance coefficient reaches its maximum value $c_p^{\max} = 0.411$ for an optimal tip-speed ratio $\lambda_o = 7.955$.

The parameters of the PI controllers in Fig. 6.1 are listed in Table C.1. The time constant of the first-order LPFs is 0.6 ms. The dc-link capacitors are $C_o = 2000\ \mu$F.

C.2 Laboratory Prototype Parameters

The laboratory prototype for a PMSG/Vienna rectifier system is shown in Fig. C.1. The experiments were conducted using a machine manufactured by ESTUN Automation (model: EMJ-04APB22). The machine parameters are as follows: $R_s = 2.358\ \Omega$; $L_q = 8.495$ mH;

Table C.1 Parameters of PI Controllers with Transfer Function $K(1+\frac{1}{\tau s})$

	q-axis current	d-axis current	neutral voltage
K	1.99	1.03	0.008
τ	0.0033	0.0033	0.01

$L_d = 7.485$ mH; $\lambda_m = 0.0607$ Vs; $p = 4$; the maximum stator current $I_{s\,\max} = 3.8$ A, peak; the rated electrical frequency and rated power were defined as 100 Hz and 200 W, respectively. The dc-link voltage was set to $V_o = 50$ V. The dc-link capacitors are $C_o = 400$ μF.

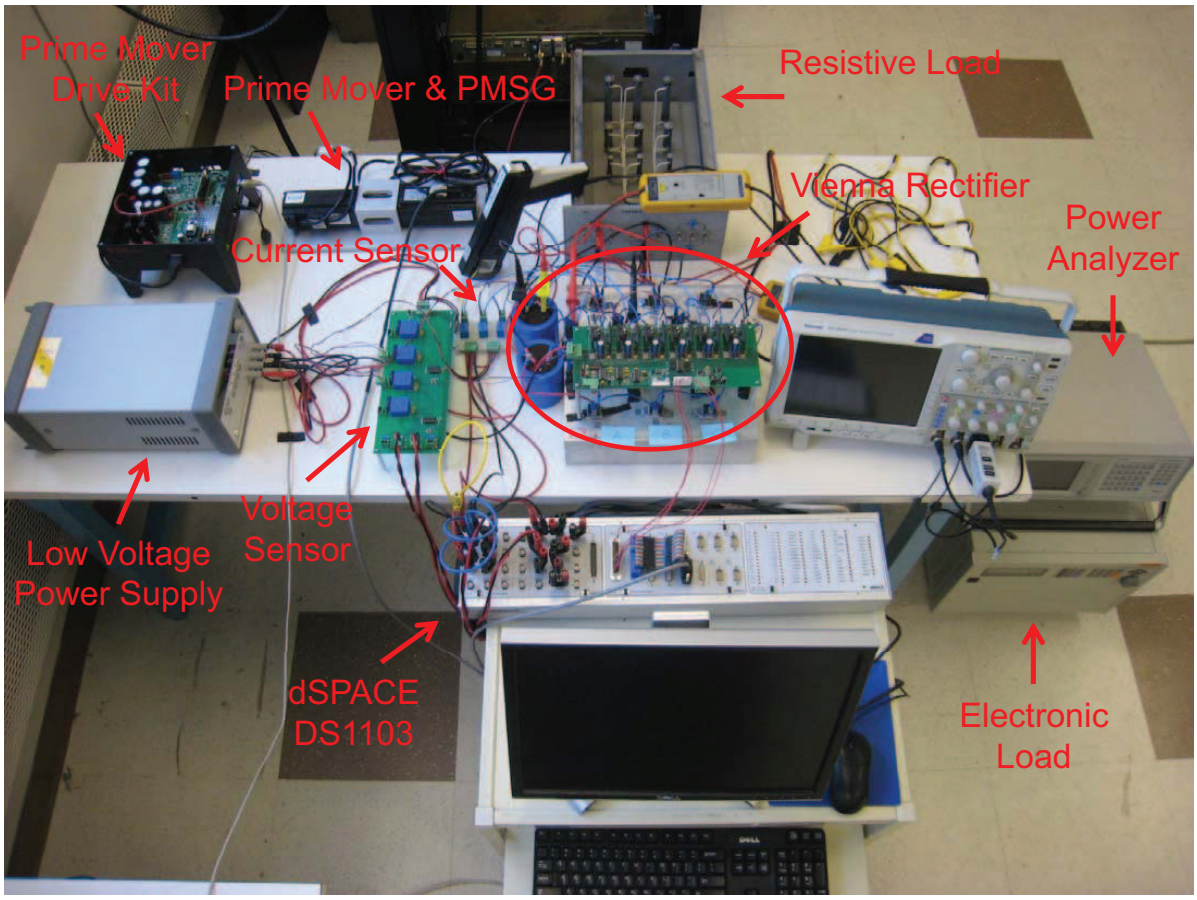

Figure C.1 Laboratory prototype.

Bibliography

[1] "20% Wind Energy by 2030," U.S. Dept. of Energy, Tech. Rep., Jul. 2008. [Online]. Available: www1.eere.energy.gov/windandhydro/pdfs/41869.pdf

[2] T. Mai, R. Wiser, D. Sandor, G. Brinkman, G. Heath, P. Denholm, D. J. Hostick, N. Darghouth, A. Schlosser, and K. Strzepek, "Exploration of High-Penetration Renewable Electricity Futures. Vol. 1 of Renewable Electricity Futures Study," U.S. Dept. of Energy National Renewable Energy Laboratory., Tech. Rep., Jun. 2012. [Online]. Available: http://www.nrel.gov/docs/fy12osti/52409-1.pdf

[3] F. Blaabjerg and Z. Chen, *Power Electronics for Modern Wind Turbines*. Morgan & Claypool, 2006.

[4] V. Akhmatov, A. H. Nielsen, J. K. Pedersen, and O. Nymann, "Variable-speed wind turbines with multi-pole synchronous permanent magnet generators. Part I: Modelling in dynamic simualtion tools," *Wind Engineering*, vol. 27, no. 6, pp. 531–548, Dec. 2003.

[5] A. D. Hansen, P. Sørensen, F. Iov, and F. Blaabjerg, "Control of variable speed wind turbines with doubly-fed induction generators," *Wind Energy*, vol. 28, no. 4, pp. 411–434, Jun. 2004.

[6] M. Liserre, R. Cárdenas, M. Molinas, and J. Rodríguez, "Overview of multi-MW wind turbines and wind parks," *IEEE Trans. Ind. Electron.*, vol. 58, no. 4, pp. 1081–1095, Apr. 2011.

[7] R. C. Portillo, M. M. Prats, J. I. León, J. A. Sánchez, J. M. Carrasco, E. Galván, and L. G. Franquelo, "Modeling strategy for back-to-back three-level converters applied to

high-power wind turbines," *IEEE Trans. Ind. Electron.*, vol. 53, no. 5, pp. 1483–1491, Oct. 2006.

[8] E. J. Bueno, S. Cóbreces, F. J. Rodríguez, A. Hernández, and F. Espinosa, "Design of a back-to-back NPC converter interface for wind turbines with squirrel-cage induction generator," *IEEE Trans. Energy Convers.*, vol. 23, no. 3, pp. 932–945, Sep. 2008.

[9] N. Celanovic and D. Boroyevich, "A comprehensive study of neutral-point voltage balancing problem in three-level neutral-point-clamped voltage source PWM inverters," *IEEE Trans. Power Electron.*, vol. 15, no. 2, pp. 242–249, Mar. 2000.

[10] J. W. Kolar and F. C. Zach, "A novel three-phase utility interface minimizing line current harmonics of high-power telecommunications rectifier modules," *IEEE Trans. Ind. Electron.*, vol. 44, no. 4, pp. 456–467, Aug. 1997.

[11] R. Lai, F. Wang, R. Burgos, Y. Pei, D. Boroyevich, B. Wang, T. A. Lipo, V. D. Immanuel, and K. J. Karimi, "A systematic topology evaluation methodology for high-density three-phase PWM AC-AC converters," *IEEE Trans. Power Electron.*, vol. 23, no. 6, pp. 2665–2680, Nov. 2008.

[12] S. V. Bozhko, R. Blasco-Giménez, R. Li, J. C. Clare, and G. M. Asher, "Control of offshore DFIG-based wind farm grid with line-commutated HVDC connection," *IEEE Trans. Energy Convers.*, vol. 22, no. 1, pp. 71–78, Mar. 2007.

[13] P. Bresesti, W. L. Kling, R. L. Hendriks, and R. Vailati, "HVDC connection of offshore wind farms to the transmission system," *IEEE Trans. Energy Convers.*, vol. 22, no. 1, pp. 37–43, Mar. 2007.

[14] N. Flourentzou, V. G. Agelidis, and G. D. Demetriades, "VSC-based HVDC power transmission systems: An overview," *IEEE Trans. Power Electron.*, vol. 24, no. 3, pp. 592–602, Mar. 2009.

[15] O. Gomis-Bellmunt, J. Liang, J. Ekanayake, R. King, and N. Jenkins, "Topologies of multiterminal HVDC-VSC transmission for large offshore wind farms," *Electr. Power Syst. Res.*, vol. 81, no. 2, pp. 271–281, Feb. 2011.

[16] "2011 offshore development information statement," National Grid, Tech. Rep., Sep. 2011. [Online]. Available: http://www.nationalgrid.com/uk/Electricity/OffshoreTransmission/ODIS/CurrentStatement/

[17] M. Schwartz, D. Heimiller, S. Haymes, and W. Musial, "Assessment of Offshore Wind Energy Resources for the United States," U.S. Dept. of Energy, Tech. Rep., Jun. 2010. [Online]. Available: http://www.nrel.gov/docs/fy10osti/45889.pdf

[18] N. M. Kirby, L. Xu, M. Luckett, and W. Siepman, "HVDC transmission for large offshore windfarms," *IEE Power Eng. Jou.*, vol. 16, no. 3, pp. 135–141, Jun. 2002.

[19] W. Musial and B. Ram, "Large-Scale Offshore Wind Power in United States. Assessment of Opportunities and Barriers," U.S. Dept. of Energy, Tech. Rep., Sep. 2010. [Online]. Available: http://www.nrel.gov/wind/pdfs/40745.pdf

[20] C. Meyer, M. Höing, A. Peterson, and R. W. De Doncker, "Control and design of DC grids for offshore wind farms," *IEEE Trans. Ind. Appl.*, vol. 43, no. 6, pp. 1475–1482, Nov./Dec. 2007.

[21] J. Arrillaga, *High Voltage Direct Current Transmission*, 2nd ed. London, UK: Institution of Electrical Engineers, 1998.

[22] T. Funaki and K. Matsuura, "Feasibility of the lower frequency AC transmission," in *IEEE Power Engineering Society Winter Meeting*, vol. 4, 2000, pp. 2693–2698.

[23] R. Nakagawa, T. Funaki, and K. Matsuura, "Installation and control of cycloconverter to low frequency AC power cable transmission," in *Proc. of the Power Conversion Conf.*, vol. 3, Osaka, Japan, 02-05 Apr. 2002, pp. 1417–1422.

[24] X. Wang, C. Cao, and Z. Zhou, "Experiment on fractional frequency transmission system," *IEEE Trans. Power Syst.*, vol. 21, no. 1, pp. 372–377, Feb. 2006.

[25] N. Qin, S. You, Z. Xu, and V. Akhmatov, "Offshore wind farm connection with low frequency ac transmission technology," in *Proc. IEEE PES General Meeting*, Calgary, Alberta, Canada, 2009.

[26] B. K. Bose, *Modern Power Electronics and AC Drives*. New Jersey: Prentice Hall, 2002.

[27] T. Petru and T. Thiringer, "Modeling of wind turbines for power system studies," *IEEE Trans. Power Syst.*, vol. 17, no. 4, pp. 1132–1139, Nov. 2002.

[28] H. M. EL-Helw and S. B. Tennakoon, "Evaluation of the suitability of a fixed speed wind turbine for large scale wind farms considering the new UK grid code," *Renewable Energy*, vol. 33, no. 1, pp. 1–12, Jan. 2008.

[29] S. Bozhko, G. Asher, R. Li, J. Clare, and L. Yao, "Large offshore DFIG-based wind farm with line-commutated HVDC connection to the main grid: Engineering studies," *IEEE Trans. Energy Convers.*, vol. 23, no. 1, pp. 119–127, Mar. 2008.

[30] Y. Zhou, P. Bauer, J. A. Ferreira, and J. Pierik, "Operation of grid-connected DFIG under unbalanced grid voltage condition," *IEEE Trans. Energy Convers.*, vol. 24, no. 1, pp. 240–246, Mar. 2009.

[31] C. Feltes, H. Wrede, F. W. Koch, and I. Erlich, "Enhanced fault ride-through method for wind farms connected to the grid through VSC-based HVDC transmission," *IEEE Trans. Power Syst.*, vol. 24, no. 3, pp. 1537–1546, Aug. 2009.

[32] H. Kim, S. Kim, and H. Ko, "Modeling and control of PMSG-based variable-speed wind turbine," *Electric Power Systems Research*, vol. 80, pp. 46–52, 2010.

[33] A. Luna, F. K. A. Lima, D. Santos, P. Rodríguez, E. H. Watanabe, and S. Arnaltes, "Simplified modeling of a DFIG for transient studies in wind power applications," *IEEE Trans. Ind. Electron.*, vol. 58, no. 1, pp. 9–20, Jan. 2011.

[34] V. Akhmatov and H. Knudsen, "An aggregate model of a grid-connected large-scale offshore wind farm for power stability investigations–importance of windmill mechanical system," *Electric Power and Energy Systems*, vol. 24, no. 9, pp. 709–717, Nov. 2002.

[35] V. Akhmatov, H. Knudsen, A. H. Nielsen, J. K. Pedersen, and N. K. Poulsen, "Modelling and transient stability of large wind farms," *Electric Power and Energy Systems*, vol. 25, no. 2, pp. 123–144, Feb. 2003.

[36] D. J. Trudnowski, A. Gentile, J. M. Khan, and E. M. Petritz, "Fixed-speed wind-generator and wind-park modeling for transient stability studies," *IEEE Trans. Power Syst.*, vol. 19, no. 4, pp. 1911–1917, Nov. 2004.

[37] S. Abourida and J. Belanger, "Rela-time platform for the control prototyping and simulation of power electronics and motor drives," in *Proc. Int. Conf. Modeling, Simulation and Applied Optimization*, Sharjah, U.A.E., Jan. 2009.

[38] W. Qiao, G. K. Venayagamoorthy, and R. G. Harley, "Real-time implementation of a STATCOM on a wind farm equipped with doubly fed induction generators," *IEEE Trans. Ind. Appl.*, vol. 45, no. 1, pp. 98–107, Jan./Feb. 2009.

[39] G. Kim, M. Park, I. Yu, and B. Song, "RTDS-based real time simulations of grid-connected wind turbine generator systems," in *Proc. IEEE Applied Power Electronics Conference and Exposition*, Palm Springs, CA, Feb. 2010.

[40] W. Li, G. Joós, and J. Bélanger, "Real-time simulation of a wind turbine generator coupled with a battery supercapacitor energy storage system," *IEEE Trans. Ind. Electron.*, vol. 57, no. 4, pp. 1137–1145, Apr. 2010.

[41] P. Le-Huy, S. Guérette, L. A. Dessaint, and H. Le-Huy, "Dual-step real-time simulation of power electronic converters using an FPGA," in *IEEE Int. Symp. Ind. Electron.*, Montreal, Canada, Jul. 2006, pp. 1548–1553.

[42] J. C. G. Pimentel, "Implementation of simulation algorithms in FPGA for real time simulation of electrical networks with power electronics devices," in *IEEE Int. Conf. Reconfig. Comp. & FPGA's*, Sep. 2006, pp. 1–8.

[43] G. G. Parma and V. Dinavahi, "Real-time digital hardware simulation of power electronics and drives," *IEEE Trans. Power Del.*, vol. 22, no. 2, pp. 1235–1246, Apr. 2007.

[44] A. Myaing and V. Dinavahi, "FPGA-based real-time emulation of power electronic systems with detailed representation of device characteristics," *IEEE Trans. Ind. Electron.*, vol. 58, no. 1, pp. 358–368, Jan. 2011.

[45] Y. Chen and V. Dinavahi, "Digital hardware emulation of universal machine and universal line models for real-time electromagnetic transient simulation," *IEEE Trans. Ind. Electron.*, vol. 59, no. 2, pp. 1300–1309, Feb. 2012.

[46] T. Maguire and J. Giesbrecht, "Small time-step ($< 2\mu$Sec) VSC model for the real time digital simulator," in *Int. Conf. Power Syst. Transients*, Montreal, Canada, Jun. 2005.

[47] C. Dufour, J. Bélanger, S. Abourida, and V. Lapointe, "FPGA-based real-time simulation of finite-element analysis permanent magnet synchronous machine drives," in *IEEE Power Electron. Spec. Conf.*, Jun. 2007, pp. 909–915.

[48] S. Heier, *Grid Integration of Wind Energy Conversion Systems*, 2nd ed. Chichester, England; Hoboken, NJ: Wiley, 2006.

[49] M. G. Simões, B. K. Bose, and R. J. Spiegel, "Design and performance evaluation of a fuzzy-logic-based variable-speed wind generation system," *IEEE Trans. Ind. Appl.*, vol. 33, no. 4, pp. 956–965, Jul./Aug. 1997.

[50] T. Ahmed, K. Nishida, and M. Nakaoka, "Advanced control of PWM converter with variable-speed induction generator," *IEEE Trans. Ind. Appl.*, vol. 42, no. 4, pp. 934–945, Jul./Aug. 2006.

[51] W. Lu and B. T. Ooi, "Optimal acquisition and aggregation of offshore wind power by multiterminal voltage-source HVDC," *IEEE Trans. Power Del.*, vol. 18, no. 1, pp. 201–206, Jan. 2003.

[52] S. Lundberg, "Evaluation of wind farm layouts," in *Nordic Workshop on Power and Ind. Electron.*, Trondheim, Norway, Jun. 2004.

[53] P. C. Krause, O. Wasynczuk, and S. D. Sudhoff, *Analysis of Electric Machinery and Drive Systems*, 2nd ed. IEEE Press, 2002.

[54] L. Dalessandro, S. D. Round, and J. W. Kolar, "Center-point voltage balancing of hysteresis current controlled three-level PWM rectifiers," *IEEE Trans. Power Electron.*, vol. 23, no. 5, pp. 2477–2488, Sep. 2008.

[55] P. Vas, *Electrical Machines and Drives: A Space-vector Theory Approach.* Oxford University Press, 1992.

[56] O. Ojo, "The generalized discontinuous PWM scheme for three-phase voltage source inverters," *IEEE Trans. Ind. Electron.*, vol. 51, no. 6, pp. 1280–1289, Dec. 2004.

[57] T. Brückner and D. G. Holmes, "Optimal pulse-width modulation for three-level inverters," *IEEE Trans. Power Electron.*, vol. 20, no. 1, pp. 82–89, Jan. 2005.

[58] L. Dalessandro, S. D. Round, U. Drofenik, and J. W. Kolar, "Discontinuous space-vector modulation for three-level PWM rectifiers," *IEEE Trans. Power Electron.*, vol. 23, no. 2, pp. 530–542, Mar. 2008.

[59] PLECS User Manual. [Online]. Available: http://www.plexim.com/downloads/

[60] CM800HA-34H Data Sheet. [Online]. Available: http://www.pwrx.com/pwrx/docs/cm800ha-34h.pdf

[61] QRS1240T30 Data Sheet. [Online]. Available: http://www.pwrx.com/pwrx/docs/qrs1240t30.pdf

[62] CM400HA-24A Data Sheet. [Online]. Available: http://www.pwrx.com/pwrx/docs/cm400ha_24a.pdf

[63] Mitsubishi Electric Power Module Loss Simulator. [Online]. Available: http://www.mitsubishichips.com/Global/products/powermod/index.html

[64] H. D. Lambilly and H. O. Keser, "Failure analysis of power modules: a look at the packaging and reliability of large IGBT's," *IEEE Trans. Compon., Hybrids, Manuf. Technol.*, vol. 16, no. 4, pp. 412–417, Jun. 1993.

[65] W. Wu, G. Gao, L. Dong, and Z. Wang, "Thermal reliability of power insulated gate bipolar transistor (IGBT) modules," in *IEEE Semicond. Thermal Meas. and Mgmt. Symp.*, Austin, TX, USA, 1996, pp. 136–141.

[66] B. C. Rabelo, Jr., W. Hofmann, J. L. da Silva, R. G. de Oliveira, and S. R. Silva, "Reactive power control design in doubly fed induction generators for wind turbines," *IEEE Trans. Ind. Electron.*, vol. 56, no. 10, pp. 4154–4162, Oct. 2009.

[67] P. K. Goel, B. Singh, S. S. Murthy, and N. Kishore, "Isolated wind-hydro hybrid system using cage generators and battery storage," *IEEE Trans. Ind. Electron.*, vol. 58, no. 4, pp. 1141–1153, Apr. 2011.

[68] H. Chen, S. Sun, D. C. Aliprantis, and J. Zambreno, "Dynamic simualtion of electric machines on FPGA boards," in *IEEE Int. Electr. Mach. and Drives Conf.*, May 2009, pp. 1842–1847.

[69] A. Rajaei, M. Mohamadian, S. M. Dehghan, and A. Yazdian, "PMSG-based variable speed wind energy conversion system using Vienna rectifier," *Euro. Trans. Electr. Power*, vol. 21, no. 1, pp. 954–972, Jan. 2011.

[70] L. Wang and C.-H. Lee, "Dynamic analysis of parallel operated self-excited induction generators feeding an induction motor load," *IEEE Trans. Energy Convers.*, vol. 14, no. 3, pp. 479–485, Sep. 1999.

[71] K. A. Corzine, B. T. Kuhn, S. D. Sudhoff, and H. J. Hegner, "An improved method for incorporating magnetic saturation in the q-d synchronous machine model," *IEEE Trans. Energy Convers.*, vol. 13, no. 3, pp. 270–275, Sep. 1998.

[72] 5MPA Series Metallized Polypropylene. [Online]. Available: http://www.ecicaps.com/capacitors.php

[73] QRS0680T30 Data Sheet. [Online]. Available: http://www.pwrx.com/pwrx/docs/QRS0680T30.pdf

[74] PS410625 Data Sheet. [Online]. Available: http://www.pwrx.com/pwrx/docs/ps41__25.pdf

[75] B. T. Cassimere, S. D. Sudhoff, B. N. Cassimere, D. C. Aliprantis, and M. D. Swinney, "IGBT and PN junction diode loss modeling for system simulations," in *Proc. IEEE Int. Elec. Mach. Drives Conf. (IEMDC)*, San Antonio, TX, May 2005, pp. 941–949.

[76] E. C. Morgan, M. Lackner, R. M. Vogel, and L. G. Baise, "Probability distributions for offshore wind speeds," *Energy Conversion and Management*, vol. 52, pp. 15–26, Jan. 2011.

[77] M. Chinchilla, S. Arnaltes, and J. C. Burgos, "Control of permanent-magnet generators applied to variable-speed wind-energy systems connected to the grid," *IEEE Trans. Energy Convers.*, vol. 21, no. 1, pp. 130–135, Mar. 2006.

[78] E. Tremblay, S. Atayde, and A. Chandra, "Comparative study of control strategies for the doubly fed induction generator in wind energy conversion systems: a DSP-based implementation approach," *IEEE Trans. Sustainable Energy*, vol. 2, no. 3, pp. 288–299, Jul. 2011.

[79] H. Nian, Y. Song, P. Zhou, and Y. He, "Improved direct power control of a wind turbine driven doubly fed induction generator during transient grid voltage unbalance," *IEEE Trans. Energy Convers.*, vol. 26, no. 3, pp. 976–986, Sep. 2011.

[80] H. Polinder, F. F. A. van der Pijl, G.-J. de Vilder, and P. J. Tavner, "Comparison of direct-drive and geared generator concepts for wind turbines," *IEEE Trans. Energy Convers.*, vol. 21, no. 3, pp. 725–733, Sep. 2006.

[81] A. D. Hansen and G. Michalke, "Multi-pole permanent magnet synchronous generator wind turbines' grid support capability in uninterrupted operation during grid faults," *IET Renewable Power Generation*, vol. 3, no. 3, pp. 333–348, Sep. 2009.

[82] H. Geng, G. Yang, D. Xu, and B. Wu, "Unified power control for PMSG-based WECS operating under different grid conditions," *IEEE Trans. Energy Convers.*, vol. 26, no. 3, pp. 822–830, Sep. 2011.

[83] D. C. Aliprantis, S. A. Papathanassiou, M. P. Papadopoulos, and A. G. Kladas, "Modeling and control of a variable-speed wind turbine equipped with permanent magnet synchronous generator," in *IEEE Int. Conf. Electrical Machines*, Espoo, Finland, Aug. 2000.

[84] H. Chen and D. C. Aliprantis, "Induction generator with Vienna rectifier: feasibility study for wind power generation," in *Proc. IEEE Int. Conf. Electrical Machines*, Rome, Italy, Sep. 2010.

[85] ——, "Analysis of squirrel-cage induction generator with Vienna rectifier for wind energy conversion system," *IEEE Trans. Energy Convers.*, vol. 26, no. 3, pp. 967–975, Sep. 2011.

[86] P. Ide, N. Froehleke, and H. Grotstollen, "Comparison of selected 3-phase switched mode rectifiers," in *19th International Telecommunications Energy Conference*, Melbourne, Australia, Oct. 1997, pp. 630–636.

[87] T. Viitanen and H. Tuusa, "A steady-state power loss consideration of the 50kw VIENNA I and PWM full-bridge three-phase rectifiers," in *IEEE Annual Power Electronics Specialists Conference*, Cairns, Australia, Jun. 2002, pp. 915–920.

[88] R. Teichmann, M. Malinowski, and S. Bernet, "Evaluation of three-level rectifiers for low-voltage utility applications," *IEEE Trans. Ind. Electron.*, vol. 52, no. 2, pp. 471–481, Apr. 2005.

[89] L. Y. Pao and K. E. Johnson, "A tutorial on the dynamics and control of wind turbines and wind farms," in *American Control Conference (ACC)*, St. Louis, MO, Jun. 2009.

[90] 5SNA 1200G450300 Data Sheet. [Online]. Available: http://www.abb.com/ProductGuide/

[91] 5SDF 10H4502 Data Sheet. [Online]. Available: http://www.abb.com/ProductGuide/

[92] 5SDD 11D2800 Data Sheet. [Online]. Available: http://www.abb.com/ProductGuide/

[93] R. Schnell and U. Schlapbach, "Realistic benchmarking of IGBT-modules with the help of a fast and easy to use simulation-tool," in *Proc. PCIM'04 Power Electronics Conference*, Nuremberg, Germany, 2004.

[94] D. W. Chung, J. S. Kim, and S. K. Sul, "Unified voltage modulation technique for real-time three-phase power conversion," *IEEE Trans. Ind. Appl.*, vol. 34, no. 2, pp. 374–380, Mar./Apr. 1998.

[95] J. H. Seo, C. H. Choi, and D. S. Hyun, "A new simplified space-vector PWM method for three-level inverters," *IEEE Trans. Power Electron.*, vol. 16, no. 4, pp. 545–550, Jul. 2001.

[96] R. Burgos, R. Lai, Y. Pei, F. Wang, D. Boroyevich, and J. Pou, "Space vector modulation for Vienna-type rectifiers based on the equivalence between two- and three-level converters: a carrier-based implementation," *IEEE Trans. Power Electron.*, vol. 23, no. 4, pp. 1888–1898, Jul. 2008.

[97] B. Wu, *High-Power Converters and AC Drives*. Hoboken, NJ: Wiley, 2006.

[98] N. B. Negra, J. Todorovic, and T. Ackermann, "Loss evaluation of HVAC and HVDC transmission solutions for large offshore wind farms," *Electr. Power Syst. Res.*, vol. 76, no. 11, pp. 916–927, Jul. 2006.

[99] J. Robinson, D. Jovcic, and G. Joós, "Analysis and design of an offshore wind farm using a MV DC grid," *IEEE Trans. Power Del.*, vol. 25, no. 4, pp. 2164–2173, Oct. 2010.

[100] M. Popat, B. Wu, F. Liu, and N. Zargari, "Coordinated control of cascaded current-source converter based offshore wind farm," *IEEE Trans. Sustainable Energy*, vol. 3, no. 3, pp. 557–565, Jul. 2012.

[101] E. Prieto-Araujo, F. D. Bianchi, A. Junyent-Ferré, and O. Gomis-Bellmunt, "Methodology for droop control dynamic analysis of multiterminal VSC-HVDC grids for ooffshore wind farms," *IEEE Trans. Power Del.*, vol. 26, no. 4, pp. 2476–2485, Oct. 2011.

[102] E. Veilleux and B. Ooi, "Multiterminal HVDC with thyristor power-flow controller," *IEEE Trans. Power Del.*, vol. 27, no. 3, pp. 1205–1212, Jul. 2012.

[103] J. Arrillaga, Y. H. Liu, and N. R. Watson, *Flexible Power Transmission: The HVDC Options*. Hoboken, NJ: Wiley, 2007.

[104] B. R. Pelly, *Thyristor Phase-Controlled Converters and Cycloconverters*. New York: Wiley, 1971.

[105] A. R. Bergen and V. Vittal, *Power System Analysis*, 2nd ed. New Jersey: Prentice Hall, 2000.

[106] J. Arrillaga and N. R. Watson, *Power System Harmonics*, 2nd ed. Hoboken, NJ: Wiley, 2003.

[107] XLPE Land Cable Systems User's Guide. [Online]. Available: http://www.abb.com

[108] XLPE Submarine Cable Systems. [Online]. Available: http://www.abb.com

[109] "2010 offshore development information statement," National Grid, Tech. Rep., Sep. 2010. [Online]. Available: http://www.nationalgrid.com/uk/Electricity/ODIS/Archive/

[110] L. Freris and D. Infield, *Renewable Energy in Power Systems.* Wiley, 2008.

[111] M. Yamamoto and O. Motoyoshi, "Active and reactive power control for doubly-fed wound rotor induction generator," *IEEE Trans. Power Electron.*, vol. 6, no. 4, pp. 624–629, Oct. 1991.

[112] R. Pena, J. C. Clare, and G. M. Asher, "Doubly fed induction generator using back-to-back PWM converters and its application to variable-speed wind-energy generation," *IEE Proceedings Electric Power Applications*, vol. 143, no. 3, pp. 231–241, May 1996.

[113] R. Fadaeinedjad, M. Moallem, and G. Moschopoulos, "Simulation of a wind turbine with doubly fed induction generator by FAST and Simulink," *IEEE Trans. Energy Convers.*, vol. 23, no. 2, pp. 690–700, Jun. 2008.

[114] A. Petersson, L. Harnefors, and T. Thiringer, "Comparison between stator-flux and grid-flux-oriented rotor current control of doubly-fed induction generators," in *2004 IEEE 35th Annual Power Electronics Specialists Conference*, vol. 1, 20-25 Jun. 2004, pp. 482–486.

[115] W. Gautschi, *Numerical Analysis: An Introduction.* Boston: Birkhäuser, 1997.

[116] E. Jamro and K. Wiatr, "FPGA implementation of 64-bit exponential function for HPC," in *IEEE Int. Conf. Field Programmable Logic and Applications*, Aug. 2007, pp. 718–721.

[117] P. P. Chu, *RTL Hardware Design Using VHDL: Coding for Efficiency, Portability, and Scalability.* Hoboken, New Jersey: Wiley-Interscience, 2006.

[118] J. Cavanagh, *Verilog HDL: Digital Design and Modeling.* Boca Raton, Florida: CRC Press, 2007.

[119] O. Anaya-Lara, N. Jenkins, J. Ekanayake, P. Cartwright, and M. Hughes, *Wind Energy Generation: Modelling and Control.* Wiley, 2009.